Spring 1-1-2013

# New Methods in Optical Track Association and Uncertainty Mapping of Earth-Orbiting Objects

Kohei Fujimoto
*University of Colorado at Boulder*, kfujimot@gmail.com

**New Methods in Optical Track Association and Uncertainty Mapping of Earth-Orbiting Objects**

by

**Kohei Fujimoto**

M.S., The University of Colorado - Boulder, 2011

B.S.E., The University of Michigan, 2009

A thesis submitted to the

Faculty of the Graduate School of the

University of Colorado in partial fulfillment

of the requirements for the degree of

Doctor of Philosophy

Department of Aerospace Engineering Science

2013

This thesis entitled:
New Methods in Optical Track Association and Uncertainty Mapping of Earth-Orbiting Objects
written by Kohei Fujimoto
has been approved for the Department of Aerospace Engineering Science

_____

Prof. Daniel J. Scheeres

_____

Prof. George H. Born

Date _____

The final copy of this thesis has been examined by the signatories, and we find that both the content and the form meet acceptable presentation standards of scholarly work in the above mentioned discipline.

Fujimoto, Kohei (Ph.D., Aerospace Engineering Science)

New Methods in Optical Track Association and Uncertainty Mapping of Earth-Orbiting Objects

Thesis directed by Prof. Daniel J. Scheeres

As more and more sensing capabilities for space surveillance are introduced, we expect that both correlated and uncorrelated tracks of resident space objects will drastically increase. Existing observation association techniques rely on simplified dynamics, *ad hoc* association criteria, and linear propagation of Gaussian uncertainty. To maintain an accurate catalog of resident space objects now and into the future, however, a more consistent description of the uncertainty associated with said objects is desired. Two characteristics of the space situational awareness problem are applicable to this goal: that the type of observation significantly influences the geometry of the observational uncertainty, and that the dynamical system is amenable to analytic or semi-analytic solution techniques. In this dissertation, each of these characteristics are examined and ultimately applied to the problem of optical track association, often referred to as the too-short arc problem.

First, an analytical method of non-linear uncertainty propagation is discussed. A special solution to the Fokker-Planck equations for deterministic systems and the state transition tensor concept are combined so that, given an analytical expression of both the initial probability distribution and the dynamics, the probability distribution may be expressed analytically for all time. Next, an observation association technique is proposed which involves admissible regions: probability density functions representing not only the measurement errors but also the limited knowledge in the unobserved variables. Bayes' rule is directly applied to associate multiple observations and subsequently obtain an orbit estimate. A quantitative argument on the effects of measurement errors on the admissible region, and consequently direct Bayesian track association, are also given. Finally, the proposed approach to short-arc association and initial orbit determination are applied to optical observations taken at the Astronomical Institute of the University of Bern. In addition to matching over half of the objects detected by conventional techniques, the proposed method finds two additional objects at or near geostationary altitude, all without *a priori* information.

**Dedication**

For my future wife.

*Dicebat Bernardus Carnotensis nos esse quasi* ***nanos gigantium humeris insidentes****, ut possimus plura eis et remotiora videre, non utique proprii visus acumine, aut eminentia corporis, sed quia in altum subvenimur et extollimur magnitudine gigantea.*

— John of Salisbury

## Acknowledgements

I appreciate the many giants who allowed me to stand on their shoulders and shared their grand view of the world; without them, this thesis would not exist. Here is an attempt to acknowledge some of them.

I would first like to thank my adviser, Dr. Daniel Scheeres, for his mentorship over the past five and a half years. It is impossible to overstate the positive influence Dan has had on me as an aspiring academic, young professional, and educator-in-training. I'd also like to acknowledge other members of my thesis committee: Dr. Penina Axelrad, Dr. George Born, Dr. Elizabeth Bradley, and Mr. David Vallado. I'm especially indebted to George for introducing me to statistical orbit determination both in class and as part of the LiAISON research group. Outside of the committee, Dr. Terry Alfriend has provided much input to this thesis; his comments were always welcome.

A very special thanks is stated to my mentors at internship positions held while writing this thesis. Thomas Schildknecht and Johannes Herzog at the University of Bern not only provided observational data for this thesis but also expertise and insight on tracking resident space objects. In addition, IHI Corporation gave me the opportunity to experience almost all aspects of the too short arc problem, from the planning of observations all the way to initial orbit determination.

I have been fortunate enough to be surrounded by witty friends and colleagues both in and out of school. You know who you are. Don't forget to be awesome.

Last but not least, "*Domo arigato*, Mr. and Mrs. Fujimoto" for believing in their son, who got a C in math in high school, when he started yammering about becoming a theoretical researcher in astrodynamics. And of course, this thesis would be filled with so much more glum and blah had it not been for my wonderful girlfriend, Hikaru Furukawa, who has cheered me on throughout my years in graduate school.

## Contents

**Chapter**


**1** Introduction 1

1.1 Current Challenges in Space Situational Awareness . . . . . 1

1.1.1 Optical Track Association via Probability Distributions . . . . . 2

1.1.2 Analytical Non-Linear Propagation of Uncertainty . . . . . 5

1.2 Organization and Contributions . . . . . 6

**2** Analytical Non-Linear Propagation of Uncertainty 12

2.1 Solution of the Fokker-Planck Equation For a Deterministic Dynamical System . . . . . 13

2.1.1 Prediction Error as an Uncertainty Consistency Metric . . . . . 14

2.1.2 Example: Damped Harmonic Oscillator . . . . . 15

2.2 Non-Linear Mapping of System Dynamics Using State Transition Tensors . . . . . 16

2.2.1 Non-Linear Mapping of Probability Cumulants Using State Transition Tensors . . . 19

2.3 State Transition Tensors of Earth-Orbiters . . . . . 21

2.3.1 Two-Body Dynamics . . . . . 22

2.3.2 Two-Body Dynamics + Averaged $J_2$ Perturbations . . . . . 23

2.3.3 Two-Body Dynamics + Atmospheric Drag . . . . . 25

2.4 Simulated Examples . . . . . 31

2.4.1 Propagation of the 3-$\sigma$ Ellipse . . . . . 31

2.4.2 Propagation of Probability Cumulants . . . . . 42

2.4.3 Conservation of the Prediction Error . . . . . 49
2.5 Conclusions . . . . . 50

**3** Association of Short-Arc Optical Observations via The Direct Bayesian Admissible Region Method 54
3.1 The Too-Short Arc Problem . . . . . 55
3.2 The Attributable Vector . . . . . 56
3.3 The Classical Admissible Region . . . . . 59
3.4 Transformation of Virtual Objects . . . . . 62
3.4.1 Exact Transformation . . . . . 62
3.4.2 Linear Transformation . . . . . 63
3.5 The Geometry of Classical Admissible Regions . . . . . 64
3.6 Direct Bayesian Association of Observations . . . . . 65
3.6.1 The Generalized Admissible Region . . . . . 65
3.6.2 Association of Observations . . . . . 66
3.6.3 Application to Space Situational Awareness . . . . . 69
3.7 Efficient Algorithms For Admissible Region Mapping . . . . . 70
3.7.1 Linearization Algorithm . . . . . 72
3.7.2 Determining the Intersection of Planes and Hypercubes . . . . . 75
3.7.3 Benefits of the Linear Map . . . . . 81
3.7.4 Planar Mesh Mapping of Admissible Region Subregions . . . . . 82
3.7.5 Benefits of the Planar Mesh Map . . . . . 83
3.8 Limiting Cases . . . . . 84
3.8.1 Simultaneous Observations of an Object . . . . . 86
3.8.2 Observations of Satellite Constellations . . . . . 86
3.9 Simulated Example: Ground-Based Observations . . . . . 88
3.10 Simulated Example: Space-Based Observations . . . . . 93
3.10.1 False Association via the Observing Satellite's State . . . . . 93

3.10.2 Observer at LEO . . . 94
3.10.3 Observer at GEO . . . 96
3.11 Conclusions . . . 98

**4** Addressing Errors in The Direct Bayesian Admissible Region Method 100
4.1 Effects of Measurement Errors on The Admissible Region: Ground-Based Observations . . . 101
4.2 Effects of Measurement Errors on The Admissible Region: Space-Based Observations . . . 105
4.3 Extension of The Planar Mesh Map to Higher Dimensions . . . 108
4.4 "Direct Bayesian + Least Squares" Hybrid Approach . . . 112
4.5 Conclusions . . . 114

**5** Applications to Short-Arc Data at The Astronomical Institute at The University of Bern 116
5.1 Optical Observation Capabilities And Processing . . . 117
5.2 Observation Strategy . . . 120
5.3 Results . . . 121
5.3.1 Type II Solutions . . . 124
5.3.2 Type III Solutions . . . 126
5.4 Potential Improvements of The Observation Strategy . . . 126
5.5 Conclusions . . . 132

**6** Conclusions and Future Work 133

**Bibliography** 136

**Appendix**

**A** Derivation of State Transition Matrices For Two-Body Motion With Averaged $J_2$ Effects in The Poincaré Orbital Elements 142

**B** Initial Orbital Elements For Observed and Observing Objects in The Direct Bayesian Examples 146

**C** Pseudo-Code For The Direct Bayesian Admissible Region Method 148

**D** Keplerian Orbital Elements of All Objects Detected in The ZimSMART Observations With The Hybrid Method 150

# Tables

**Table**


1.1 Contribution of existing work and thesis work on track association and initial orbit determination with admissible regions. . . . . 9

1.2 Contribution of existing work and thesis work on the non-linear propagation of uncertainty in astrodynamics. . . . . 10

2.1 The sum over state space (Sum), the maximum value (Max), and the position of the maximum propagated back to the initial time ($\mathbf{X}^{0,\mathrm{Max}} = (x, u)$) for both the pdf and the probability as a function of time. The Jacobian determinant at each time is also noted ($|\partial\mathbf{X}/\partial\mathbf{X}^0|$). . . . . 16

2.2 The mean $\delta\bar{\mathfrak{l}}$ of the deviation of Poincaré element $\mathfrak{l}$ for different numerical and analytical propagation methods under two-body dynamics. "$\Delta[\%]$" indicates relative error with respect to the Monte Carlo results in percentages. . . . . 44

2.3 Elements from the covariance matrix for different numerical and analytical propagation methods under two-body dynamics. . . . . 45

2.4 Relative error of analytically propagated cumulants compared to a numerically computed truth under two-body dynamics plus atmospheric drag. . . . . 48

2.5 Computation time required to compute the mean and covariance with the Monte Carlo (MC) and state transition tensor (STT) techniques under two-body dynamics plus atmospheric drag. The process is split up into uncertainty propagation (Prop.), and mean (Mean) and covariance computation (Cov.) The results are an average over 10 simulation runs. . . . . 48

2.6 Change in $\mathcal{PE}$ after 20 orbit periods of Object 1 under two-body dynamics. "F-P" indicates propagation via the Fokker-Planck solution, and the number after "STT" indicates the order of the expansion of the dynamics. . . . . 50

3.1 The root mean square of the residuals in right ascension ($\delta$RA) and declination ($\delta$DEC) for a simulated observation of a GEO object when fit to its truth state (Object 1) and a consistent but false state (Object 2). . . . . 56

3.2 Computation time, spatial accuracy, and density accuracy between the non-linear (full) and linear admissible region maps. †: The computation time of the non-linear map does not scale linearly with sample size, since for larger samples a less efficient sorting algorithm must be used due to memory constraints. . . . . 82

3.3 Density accuracy for linear maps of non-singular Poincaré orbit elements and the singular Keplerian orbital elements. . . . . 82

3.4 Spatial and density accuracy metrics for the linear and planar mesh maps as well as runtimes for all three methods: Exact, Linear, and Planar Mesh. $\Delta$ is the difference in metrics between the linear and planar maps; bold letters indicate improvement. . . . . 85

3.5 The estimation accuracy of each observed object when using a uniform initial pdf (left) and the JSpOC TLE catalog as the initial pdf (right). All sides of each bin are approximately 0.082 in length where the units are in the Earth radii - kg - hr system. . . . . 91

3.6 The estimation accuracy of objects observed (GEO1∼GPS1) for a space-based observer in a low Earth orbit LEO-O. For each object observed ("Object"), the number of observations processed ("Number of Obs.") as well as the number of discretization bins that the posterior pdf is non-zero ("Overlap Bins") are listed. "True Sol." and "Degenerate Sol." indicate whether the observed objects' states or the observing satellite's state, respectively, are included in the solution. All sides of each bin are approximately 0.082 in length where the units are in the Earth radii - kg - hr system. . . . . 96

3.7 The estimation accuracy of each observation pair ("Obs. Pair") for the GEO-O observer. $\Delta t$ is the time between observations in hours. All sides of each bin are approximately 0.082 in length where the units are in the Earth radii - kg - hr system. . . . . 97

3.8 The estimation accuracy of each observed object for an improved GEO (GEO-O') observer. All sides of each bin are approximately 0.082 in length where the units are in the Earth radii - kg - hr system. . . . . 98

4.1 Percentage of simulation sample points where the smaller angle between the map of the displacement in the range and either angle-rate meets the criterion indicated in the top row. Values for two propagation times ($\Delta t$) are shown. . . . . 103

4.2 Percentage of simulation sample points where the larger angle between the map of the displacement in the range and either angle-rate meets the criterion indicated in the top row. Values for two propagation times ($\Delta t$) are shown. . . . . 104

4.3 The mean and maximum state errors in each Poincaré orbital element direction, as well as the ratio of their values with respect to the nominal discretization size of 0.081586, for the LEO-O observer. . . . . 106

4.4 The mean and maximum state errors in each Poincaré orbital element direction, as well as the ratio of their values with respect to the nominal discretization size of 0.081586, for the GEO-O observer. . . . . 108

4.5 Results of the association and initial orbit determination based on admissible regions ignoring (w/o Error) and including (w/ Error) effects of observational error. . . . . 111

4.6 For two orbit estimates computed based on the hybrid approach, the semi-major axis ($a$), eccentricity ($e$) and inclination ($i$) are listed along with the RMS of the residuals for the first tracklet in RA ($\mathrm{RMS_{RA}}$) and the linear regression slope parameter ($\beta_{1,\mathrm{RA}}$) with its corresponding $p$-value. . . . . 113

5.1 Instrument specs for the ZimSMART telescope. . . . . 118

5.2 Parameters for the data set used in this example. # of objects detected is based on AIUB correlation results. . . . . 121

5.3 Summary of association results ordered by solution type. Tracklets correlated to objects in the JSpOC TLE catalog with the AIUB code are indicated by their 6 letter international designator. Tracklets associated with AIUB's least squares method are indicated by a 7 letter internal designator starting with "Z." Tracklets newly associated are indicated by a bracketed number assigned by tracklet epoch. $\delta t$ is the observation time gap. . . . . 125

5.4 Orbit solutions found by type and association method. $\Delta$ is the difference between methods. 125

5.5 For Type II solutions, listed here are the semi-major axis $a$, eccentricity $e$, inclination $i$, and ratio between the observation time gap $\delta t$ and the orbit period $T$. . . . . 126

5.6 For Type III solutions, listed here are all 6 orbital elements: semi-major axis $a$, eccentricity $e$, inclination $i$, right ascension of the ascending node $\Omega$, argument of periapsis $\omega$, and mean anomaly $M$. . . . . 126

5.7 Objects where multiple tracklets with at least a 24 hour time gap are correlated based on the AIUB algorithm. Tracklets of objects under "Agreement" are associated similarly with the hybrid approach, "multi-rev" associated with another object, and "missed" not associated at all. Number of objects in each category in parenthesis. . . . . 129

B.1 The classical orbital elements at the epoch time for all 8 observed objects and 2 observer satellites in the Examples section where $r_E$ is Earth radius. . . . . 146

B.2 The Poincaré orbital elements at the epoch time for all 8 observed objects and 2 observer satellites in the Examples section listed as ($a$ [$r_E$], $e$, $i$ [rad], $\Omega$ [rad], $\omega$ [rad], $M$ [rad]), ($\mathfrak{L}$ [$r_E{}^2$/hour], $\mathfrak{l}$ [rad], $\mathfrak{G}$ [$r_E$/hour$^{1/2}$], $\mathfrak{g}$ [$r_E$/hour$^{1/2}$], $\mathfrak{H}$ [$r_E$/hour$^{1/2}$], $\mathfrak{h}$ [$r_E$/hour$^{1/2}$]), where $r_E$ is Earth radius. . . . . 147

D.1 Keplerian orbital elements of all objects detected with the hybrid approach: semi-major axis ($a$), eccentricity ($e$), inclination ($i$), right ascension of the ascending node ($\Omega$), argument of periapsis ($\omega$), and mean anomaly ($M$). Solutions sorted by the epoch of the first tracklet. "Tr 1" and "Tr 2" indicate the objects that the associated tracklets were correlated to by the AIUB code. Objects in the NORAD TLE catalog are denoted by their 6 letter international designator, those in AIUB's internal catalog by a 7 letter designator starting with "Z," and uncorrelated tracks by a bracketed number assigned by tracklet epoch. "Type" is the solution type: I, II, or III. . . . . 151

# Figures

**Figure**


2.1 The evolution of the probability density function (left) and local probability (right) for a 1-D damped harmonic oscillator. Top figures are for $t = 0$, bottom figures are for $t = 0.909$. For each data type, the coloring is such that any value larger than maximum value at the initial time corresponds to a dark red. . . . . 17

2.2 The difference in the numerically and analytically integrated mean anomaly (i.e., "Error") for different orders of expansion of mean motion $n$. The reference orbit is a 300 km altitude circular orbit with an inclination of 15°. The errors are plotted for up to 100 orbit periods of the initial orbit. . . . . 27

2.3 For an object with a semi-major axis of 300 km, eccentricity of 0.01, and an inclination of 15°, left: the difference in the numerically and analytically integrated mean anomaly (i.e. "Error") for different orders of expansion of mean motion $n$. Right: the apoapsis ($h_a$) and periapsis ($h_p$) altitude along with semi-major axis minus Earth radii ($a - \mathrm{r_E}$). Both are plotted for up to 54 orbit periods, which is the orbital lifetime of the object. . . . . 30

2.4 Initial Gaussian distribution of the state deviation in the $\mathfrak{Q}^0$-$\mathfrak{l}^0$ plane (sampled with the yellow points) with the corresponding 3-$\sigma$ ellipse (blue curve) for cases (i) (left) and (ii) (right) in Section 2.4.1.1. . . . . 32

2.5 The Gaussian distribution of the state deviation propagated for 5 (top left), 10 (top right), and 20 (bottom) orbit periods using various propagation methods for case (i) under two-body dynamics. The $\mathfrak{Q}$-$\mathfrak{I}$ plane is rotated so that the axes of the plot corresponds to the principal axis directions of the linearly propagated ellipse. The second order and higher curves are nearly identical. Points from the Monte Carlo run (labeled "Monte Carlo") represent the "complete" non-linear dynamics. The lines (labeled "$n$ order") represent how the edges of the initial 3-$\sigma$ ellipse propagate with $n$-th order state transition tensors. . . . . 33

2.6 The Gaussian distribution of the state deviation propagated for 100 orbital periods using various propagation methods under two-body dynamics. The figures have been rotated as in Figure 2.5. The figure on the right is a zoom up near the origin. . . . . 34

2.7 The Gaussian distribution of the state deviation propagated for 5 (top left), 10 (top right), 20 (bottom left), and 100 orbit periods (bottom right) using various propagation methods for case (ii) under two-body dynamics. The second order and higher curves are nearly identical. The figure for 100 orbit periods has been rotated as in Figure 2.5. . . . . 36

2.8 Initial Gaussian distribution of the state deviation (sampled with the blue points) projected onto the $\mathfrak{Q}^0$-$\mathfrak{I}^0$ (top left), $\mathfrak{G}^0$-$\mathfrak{g}^0$ (top right), and $\mathfrak{H}^0$-$\mathfrak{h}^0$ (bottom) subspaces with the corresponding 3-$\sigma$ hyper-ellipsoid (sampled with green points) in Section 2.4.1.2. . . . . 36

2.9 The Gaussian distribution of the state deviation propagated for 20 orbital periods under $J_2$ averaged perturbations only and projected onto the $\mathfrak{Q}$-$\mathfrak{I}$ (top left), $\mathfrak{G}$-$\mathfrak{g}$ (top right), and $\mathfrak{H}$-$\mathfrak{h}$ (bottom) subspaces. Monte Carlo results are in blue points and STT propagation results in green points. . . . . 37

2.10 The Gaussian distribution of the state deviation propagated for 20 orbital periods using a second order expansion of the two-body dynamics + a first order expansion of the averaged perturbation due to $J_2$. The distribution is projected onto the $\mathfrak{Q}$-$\mathfrak{I}$ subspace, then rotated so that the axes of the plot corresponds to the principal axis directions of the propagated covariance matrix. Monte Carlo results are in blue points and state transition tensor propagation results in green points. . . . . 38

2.11 Atmospheric density at the reference state as computed by the NRLMSISE-00 model and the hourly $A_p$ index starting February 8, 2009 (left, *Calm*) and July 11, 2000 (right, *Storm*). Units of time are in orbit periods of the initial orbit ($\approx$ 90.52 minutes). . . . . 38

2.12 Initial Gaussian distribution of the state deviation in the $a$-$M$ plane (sampled with the blue points) with the corresponding 3-$\sigma$ ellipse (red curve) in Section 2.4.1.3. . . . . 39

2.13 An initial Gaussian distribution of the state deviation propagated numerically (MC) and analytically (STT; number indicates expansion order) over 6.286 days under two-body dynamics plus atmospheric drag for the *Calm* (left) and *Storm* (right) scenarios in a circular orbit. The results are projected on the semi-major axis ($a$) / mean anomaly ($M$) space in units of km-rad and subsequently rotated so that the axes of the plot corresponds to the principal axis directions of the linearly propagated ellipse. . . . . 41

2.14 An initial Gaussian distribution of the state deviation propagated numerically (blue) and analytically (red: 1st order, green: 2nd order) over 3.143 days for the *Calm* (left) and *Storm* (right) scenarios under two-body dynamics plus atmospheric drag in a slightly elliptic orbit. The results are projected on the semi-major axis ($a$) / mean anomaly ($M$) space in units of km-rad and subsequently rotated so that the axes of the plot corresponds to the principal axis directions of the linearly propagated ellipse. . . . . 43

2.15 Same distribution as Figure 2.14 but the results are projected on the semi-major axis ($a$) / eccentricity ($e$) space in units of km-[ ] and subsequently rotated so that the axes of the plot corresponds to the principal axis directions of the linearly propagated ellipse. . . . . 43

2.16 The change in $\mathcal{PE}(t)$ over time using various propagation methods under two-body dynamics. "F-P" indicates propagation via the Fokker-Planck solution, and the number after "STT" indicates the order of the expansion of the dynamics. The Linear and F-P (STT:1) curves, and the F-P (STT:2) through F-P (Complete) curves are nearly identical, respectively. . . . . 51

2.17 An initial Gaussian distribution propagated numerically (blue) and analytically (green) over 1.2572 days for the *Storm* scenario in a circular orbit with $J_2$ effects included. The result is projected on the semi-major axis ($a$) / mean anomaly ($M$) space in units of km-rad and subsequently rotated so that the axes of the plot correspond to the principal axis directions of the linearly propagated ellipse. . . . . 53

3.1 History of residuals in right ascension ($\delta$RA) and declination ($\delta$DEC) for a simulated observation of a geostationary orbit object fit to its true state (Object 1) and a consistent but false state (Object 2). . . . . 57

3.2 A classical admissible region for a simulated ground-based observation, where $\mathcal{A} = (\alpha, \delta, \dot{\alpha}, \dot{\delta})$ = (118.258 deg, -13.625 deg, 29.060 arcsec/sec, 3.747 arcsec/sec). The inertial longitude $\Theta$ and latitude $\Phi$ of the observatory are $(\Theta, \Phi)$ = (275.0 deg, 5.7 deg). The different shadings represent the different regions which satisfy each criterion in set $C$ ($C_1$: light circle, $C_2$: satisfied for the region plotted, $C_3$: dark circle, $C_4$: dark dot). The admissible region is where all types of shading overlap, or the region outlined by the black line. Unit of range are in Earth radii, range-rate in Earth radii / hour. . . . . 60

3.3 An admissible region for a simulated space-based observation, where $\mathcal{A} = (\alpha, \delta, \dot{\alpha}, \dot{\delta})$ = (53.09 deg, -18.74 deg, 12.17 arcsec/sec, 0.5872 arcsec/sec). The position $\mathbf{P}_O$ and velocity $\dot{\mathbf{P}}_O$ of the observer are (-37590.4, 17091.2, 7205.36) km and (-1.56206, -2.66918, -0.0225619) km/s, respectively. The different shadings represent the different regions which satisfy each criterion in set $C_1$ (circle), $C_3$ (cross), and $C_4$ (light dot). The admissible region is where all types of shading overlap, or the region indicated by the dark dots. . . . . 61

3.4 Map $T$ evolves admissible regions $F_{\mathfrak{Y}1}(t_1)$ (blue) and $F_{\mathfrak{Y}2}(t_2)$ [orange] from two separate observations to a common epoch $\tau$. The intersection point [green] is where the observed object most likely exists in state space. . . . . 71

3.5 Grid in $\rho$-$\dot{\rho}$ for the linear map of $\tilde{\tilde{S}}_2$. . . . . 73

3.6 Components of $\bar{\mathbf{X}}$ in 3-space along a line segment parameterized by $\kappa$. Each bold line represents a different component of $\bar{\mathbf{X}}$ as a function of $\kappa$, and the dashed line represents the corresponding bin index for each value of $\kappa$. The black dotted lines are the values of $\kappa$ for which this line segment cuts through a bin boundary; this line segment cuts through bins $\mathbf{i} = (\text{red}, \text{green}, \text{blue})^T = (7, 7, 2)^T$, $(6, 7, 2)^T$, $(6, 6, 2)^T$, and $(6, 6, 1)^T$. . . . . 76

3.7 A 3-dimensional representation of the linear mapping process. The gray dashed lines represent the boundaries of the bins. The brown surface is the admissible region map, and the blue plane is a portion of the admissible region mapped to the state space about the asterisk. The plane cuts through 4 bins; regions belonging to different bins are distinguished by the shading. . . . . 78

3.8 An *s*-*t* plane diagram for a linear map of the admissible region defined by $\bar{\mathbf{X}}_1 = (99.556, 43.021, 38.964, 25.941, 69.507, 64.876)^T$, $\bar{\mathbf{X}}_2 = (99.19, 42.991, 39.019, 26.047, 69.492, 64.873)^T$, and $\bar{\mathbf{X}}_3 = (98.626, 42.994, 38.975, 26.201, 69.498, 64.877)^T$. The red lines represent the linear map boundaries, the blue lines the bin boundaries, and the blue dots all of the intersection points. The indices of the different bins that project onto the linear map are labeled accordingly. . . . . 80

3.9 A schematic of local mapping of the admissible region using the linear (left) and planar mesh (right) techniques. The figure is an isometric view. The planar regions indicate local maps with respect to each reference point, indicated by the asterisks. Since each local map has different reference points, there will be inconsistencies (i.e. gaps) at the edges. The planar mesh map alleviates this problem because the mapping of vertices is more precise. . . 83

3.10 A histogram of the number of bins in the "truth" distribution which are not included in the linear (blue) and planar mesh (red) maps as a function of the semi-major axis of that bin. Number of bins are accumulated over one Earth radius. . . . . 85

3.11 Combined pdf $h$ of two near-parallel pdfs (CM1 observed simultaneously at ($\phi$ [deg], $\Theta$ [deg]) = $(57.296, 57.295)$ and $(114.59, 85.944)$ at time $t = 26.36$ hours; c.f. Appendix B) as the discretization is refined from $M = 1.7624 \times 10^{12}$ (top) to $1.2M$ (middle) and $1.5M$ (bottom). . . . . 87

3.12 Correlation of observations of 2 different objects separated by a mean anomaly of $2/3\pi$ rad on the same orbital plane as EM2 (c.f. Appendix B). Observations are separated by 14.85 hours (top) and 60.61 hours (bottom). All observations are made at ($\phi$ [deg], $\Theta$ [deg]) = $(229.18, 114.59)$. . . . . 89

3.13 Projections of probability distributions when correlating observations of two different objects (top; LEO2-LEO3) and the same object (bottom; LEO2-LEO2). Length units in Earth radii, time units in hours, angle units in radians. . . . . 92

3.14 Projections of admissible region maps when associating observations from LEO-O of two different objects (GEO1-GEO2). Each subplot is a 2-dimensional subspace of the Poincaré space. Regions where the associated pdf for GEO1 is non-zero are in red, GEO2 in green. The blue region is where the posterior pdf is non-zero; i.e. where the two maps intersect. The yellow asterisks indicate the true state of the observed objects, and the cyan asterisk is the state of the observing satellite. The bottom plot is a zoom in of the top plot focusing on the blue region. Units of length are in Earth radii, time in hours, and angle in radians. . . . . 95

4.1 Norm of displacement in the $\rho$ (blue), $\dot{\rho}$ (green), $\alpha$ (red), $\delta$ (cyan), $\dot{\alpha}$ (purple), and $\dot{\delta}$ (gold) directions when mapped to the Poincaré orbital element space. Time propagated for 0 (left) and 120 hours (right). . . . . 102

4.2 Left: ratio between the norm of the displacement in $\alpha$ and $\dot{\alpha}$ when mapped to the Poincaré orbital element space versus the velocity of the observed object. Right: similar plot but for $\delta$ and $\dot{\delta}$. . . . . 103

4.3 Left: ratio between the norm of the displacement in $\alpha$ when mapped to the Poincaré orbital element space versus the object's inclination. Right: similar plot but for $\delta$. . . . . 103

4.4 The smaller angle between the map of the displacement in the range and either angle-rate for all simulations. Left: propagation time is 0, right: propagation time is 120 hours. . . . . 104

4.5 The larger angle between the map of the displacement in the range and either angle-rate for all simulations. Left: propagation time is 0, right: propagation time is 120 hours. . . . . 104

4.6 Scatter plot of the smaller angle between the map of the displacement in the range and either angle-rate versus the velocity of the observed object. The propagation time is 0. . . . . 105

4.7 Errors in the Poincaré orbital elements due to uncertainty in the attributable vector as a function of time for the LEO-O observer. The black dotted line indicates the nominal discretization size. . . . . 107

4.8 Errors in the Poincaré orbital elements due to uncertainty in the attributable vector as a function of time for the GEO-O observer. The black dotted line indicates the nominal discretization size. . . . . 107

4.9 Admissible region including effects of observational errors in the Poincaré orbital element space for the first (blue) and second (red) observations. True state (white) lies on top of the posterior pdf (green). . . . . 112

5.1 Current setup of ZimSMART [26]. . . . . 117

5.2 Distribution of resident space objects in the geostationary belt with respect to right ascension and declination [25]. . . . . 120

5.3 A flowchart of the "direct Bayesian + least squares" hybrid approach. . . . . 123

5.4 The orbit (dotted red line) and position of Object 9 at the first observation epoch along with orbits and positions of catalogued objects 08065B and 10021A (solid red lines) as well as the observation direction (black). Left: view along the $-z$-direction in the J2000 coordinate frame, right: view along the $+y$-direction in the J2000 coordinate frame. Figures generated with AGI's STK. . . . . 127

5.5 Similar to Figure 5.4 but for the second observation epoch. Figures generated with AGI's STK. . . . . 127

5.6 Ground tracks of Type III solutions for a full orbit from the observation epoch: Objects 1 (light blue) and 8 (dark blue). The position of each object at the epoch of the first observation is indicated by a satellite logo. The position of the Zimmerwald observatory is also plotted with a dome logo. Figure generated with AGI's STK. . . . . 128

5.7 History of RA/DEC $O - C$ residuals using the hybrid method for two tracklets correlated to object 84028A with current AIUB code. Plot points to the left of the dotted line are for the first tracklet and to the right the second. $p$-values for the model utility test are indicated per tracklet and angle. . . . . 131

# Chapter 1

# Introduction

## 1.1 Current Challenges in Space Situational Awareness

Situational awareness of resident space objects (RSOs) such as active satellites and space debris is highly important for all current and future space-faring nations. The number of objects in orbit under 1 cm in diameter is believed to be in the hundreds of thousands, with one estimate as of May 2009 at 700,000 [88]. On the other hand, as of January 2013, approximately 16,500 objects exist in the public two-line element (TLE) catalog maintained by the United States' Joint Space Operations Center (JSpOC) [54]. Objects currently contained in the catalog are generally greater than 5 cm in diameter, but smaller objects are expected to be detected given recent optical sensor additions to the Space Surveillance Network (SSN), such as the Space Surveillance Telescope (SST) and the Space Based Space Surveillance (SBSS) satellite [64]. With ever more space surveillance sensing capabilities coming online, now and in the future, both domestically and internationally, we expect that both the number of cataloged objects and the number of observations that fail to correlate with the catalog (i.e., uncorrelated tracks, or UCTs) to drastically increase [85].

We take special note that the motion of satellites in Earth orbit are particularly amenable to having their solution described through analytic or semi-analytic techniques [3, 8, 43, 83]. Even when stronger non-gravitational perturbations such as solar radiation pressure and atmospheric drag are encountered, these perturbations generally have deterministic components that are substantially larger than their time-varying stochastic components, meaning that they can be modeled either numerically or, in some cases, analytically [9, 31, 32, 40, 49, 58, 73]. These facts open the door to the application of analytical or semi-analytical techniques to describe the motion of a satellite, even accounting for uncertainty in model parameters – so

long as they do not contain strong dynamical stochastic variations. In particular, if an approximate technique is found for describing the dynamics of a satellite over time, such a solution can be applied to a range of important questions related to the dynamical propagation of an object's probability density function (pdf).

We address these questions in this dissertation, as outlined in the Thesis Statement:

> The association of multiple optical tracks of Earth-orbiting objects may be improved by efficiently expressing the current and future state uncertainty. Sparse probability distributions in the state space obtained from both angles and angle-rate data enable rapid association and initial orbit determination. These probability distributions may be propagated analytically and non-linearly by means of the state transition tensor concept.

Let us introduce each facet of the Thesis Statement in detail.

### 1.1.1 Optical Track Association via Probability Distributions

One problem of concern in space situational awareness (SSA) is the association of optical observations of Earth-orbiting objects. Traditionally, track association is done by performing an initial orbit determination (IOD) based on the angular information of each track and comparing the tracks in either state or observation variable space. The problem with this approach is twofold. First, the association of observations must be assumed initially and then deduced from the quality of the least-squares fit; that is, the association of observations is a direct function of the quality of the orbit estimation and vice versa. Especially in a survey-type observation strategy, even with the improvement in SSA observational capabilities as described in the previous section, due to the large number of objects in orbit, only a limited number of observations are available per night per object, each over short observation arcs that span a few minutes [46]. Given such a small window of data, a large subset of the state space remains consistent with each tracklet, leading to poor convergence to the true solution if not divergence [83]. The association of observations, therefore, cannot be inferred confidently. Several workarounds have been proposed: e.g. to assume that the observed orbit is always circular, or to generate hypotheses on the state of the observed object [12, 17]. The former approach adds too many constraints to the system such that the state estimate is inaccurate, and the latter adds too few constraints such that computational cost is high. Indeed, at the Astronomical Institute at the University of Bern (AIUB) where an independent catalogue of Earth-orbiting object is maintained with a circular orbit

assumption followed by a least squares fit, the majority of newly catalogued objects are only observed over one night, never to be acquired again. The second problem is that the distance metric between orbit estimates is often determined *ad hoc* without regard of probabilistic or dynamical information in the observations. As such, track association is currently performed by human analysts at JSpOC, which processes data from the SSN [27]. Numerous probability-based distance metrics have been proposed to automate this procedure, such as the Mahalonobis, Bhattacharyya, and Kullback-Leibler distances, but all assume we have a good estimate on the uncertainty of the initial orbit estimate, which is seldom true [29]. These difficulties constitute the crux of the *too short arc* (TSA) problem [50, 82].

We propose a technique of associating multiple optical observations using highly constrained pdfs, which we refer to as *admissible regions* (ARs), in Poincaré orbital element space. By converting observation information into a pdf, the information can rationally be combined directly using Bayes' theorem. In fact, we may conduct an apples-to-apples comparison with any probabilistic data: e.g. density information from the JSpOC TLE catalog for correlation purposes. A significant computational bottleneck in this proposed method arises from the very large number of sample points that must be mapped non-linearly in both space and time to completely represent the AR in 6-D space. This problem is avoided by approximating the AR as a conglomerate of smaller subsets and linearly mapping these regions. A proof-of-concept implementation, in which simulated ground observations are processed, performs well for objects from low Earth orbit (LEO) to geosynchronous orbit (GEO). Monte Carlo-like test results suggest that this result is true even in the presence of observation error, albeit errors in the observations as well as any dynamical modeling errors impose a definite upper bound on the accuracy of state estimation. Situations where the proposed algorithm may not perform are identified: one where one object is observed simultaneously at two observatories and another where a satellite constellation is observed from one observatory.

The technique proposed serves as a fundamental solution technique for initial orbit determination given two precise optical observation tracks. The AR expresses our *limited* knowledge regarding the variables that are observed indirectly: range and range-rate [13]. In conventional filtering, pdfs of the observations only describe the error in the measurement variables and are realized in the state space as likelihoods. For underdetermined systems, the integral of the likelihood function over the state space is divergent as

we gain no information from the observations in coordinate directions corresponding to the variables indirectly observed. We realize, however, that knowledge in these directions is not completely *lacking* for many real-world systems as the likelihood function may suggest. That is, we may add physical constraints to the observed object's state such that we define a compact pdf still representative of all relevant states.

The AR method can be applied to space-based optical observations of RSOs as well. Compared to ground-based observations, those that are space-based allow for tracking of smaller objects regardless of weather [87]. Several missions have been flown to date. In 1997, the Space Based Visible (SBV) sensor on the Midcourse Space Experiment (MSX) satellite became a contributing sensor to the SSN after the completion of its primary mission for the Ballistic Missile Defense Organization [74, 77]. The Space Based Surveillance System (SBSS) launched in 2010 is a follow-up satellite to MSX/SBV dedicated to the task of space situational awareness (SSA)[1] [80]. Space agencies, corporations, and academia in Europe and Asia have also shown interest in space-based SSA [16, 30, 78]. Outside the realm of dedicated payloads, hosted payload sensors on spacecraft in geostationary or geostationary transfer orbits may provide observational capabilities at a much lower cost [24, 42, 75, 86].

To accommodate for the motion of the space-based observation point, we redefine the attributable vector. We address the issue of the observer's state always being a degenerate solution by excluding a small region about the observer's state in the AR. A proof-of-concept implementation shows that a LEO observer case works well, but a GEO observer case experiences numerical issues due to lack of relative motion. Therefore, if we are to place an observer close to the GEO region, we recommend a slightly eccentric and inclined orbit ($e \sim 10^{-3}$, $i \sim 10^{-1}\,^{\circ}$) and separating the observations by about 10 hours.

The above method is applied to optical observations of geosynchronous (GEO) belt objects taken at the Zimmerwald Observatory of AIUB [68]. Each tracklet consists of five images spanning over approximately two minutes. To account for observational errors as well as reduce false positive association due to ambiguity of orbital period, a "hybrid" AR + least squares approach is implemented. The IOD results from the direct Bayesian AR is fed into a least squares batch filter. The association of objects is determined through the (observed) - (computed) residuals of the filter fit; namely, both the root mean square and the

[1] http://www.boeing.com/defense-space/space/satellite/MissionBook.pdf

slope parameter of a simple linear regression of the residuals must meet a threshold value. Although the steps in this new process are similar to those in a traditional IOD [2], the justification of the association and the estimation are separated, thus improving robustness. Because the theory discussed above addresses the TSA problem in a much more probabilistically straightforward way than other IOD techniques, it allows one to reevaluate future observational strategies so that they minimize false positive / negative association solutions.

### 1.1.2 Analytical Non-Linear Propagation of Uncertainty

Another topic of recent interest is the accurate and *consistent* representation of an observed object's uncertainty under non-linear dynamics [5, 33, 34]. Traditional orbit estimation methods rely on linear propagation of Gaussian uncertainty [79]. It has been shown, however, that the Gaussian assumption is an inconsistent description of the actual uncertainty when the dynamics are highly unstable or when propagation times become long [33,38,39,56]. Several methods have been proposed to incorporate the non-linearity of the dynamics of objects in orbit and express the "non-Gaussianity" of the resulting probability distribution. The problem with many of them is that they require significant computational power. The most basic – and consequently the most computationally expensive – method is the Monte Carlo [47]. A large ensemble of sample points are propagated non-linearly. Probability cumulants and moments are estimated based on these samples. More efficient methods are often premised on the idea that computational cost should decrease as the number of sample points decreases. This includes Gaussian mixture methods where the uncertainty is sampled with Gaussian components [10, 22, 35] and quadrature methods that take fewer but judicious sample points [34, 36]. Other methods for the non-linear propagation of uncertainty are more direct: the Edgeworth filter expresses the uncertainty as a series of probability cumulants and propagates each cumulant [33] whereas polynomial chaos projects the stochastic solution of the dynamics upon orthogonal polynomial bases [37].

We propose a new method for the non-linear propagation of uncertainty in the context of SSA. In this approach, the probability density function (pdf) over the state space and its mean and covariance matrix are expressed analytically for all time via a special solution of the Fokker-Planck equations for deterministic

systems. In particular, we find that the probability is an integral invariant [66, 67]. Consequently, as long as one has an analytical description of the initial pdf and the solution to the dynamics, an analytical description of the pdf for all time can be obtained [56]. Given an analytical expression of the pdf, time propagation is extremely efficient as it is only a matter of changing the time parameter. This result holds for both conservative (i.e., Hamiltonian) and non-conservative systems. One way to express the solution of the dynamics, even for systems with no exact closed-form solutions, is via state transition tensors (STTs) [45, 56].

Overall, this method succeeds in accurately propagating uncertainty without excessive computational burden. For a proof-of-concept implementation under two-body dynamics, a second-order state transition tensor description of the dynamics is found to sufficiently capture the non-linear effects in the Poincaré orbital element space. We compare the analytically propagated 3-$\sigma$ error ellipsoid and pdf moments with those obtained from Monte Carlo simulations. As for non-conservative systems, we investigate the evolution of uncertainty for an Earth-orbiting object influenced by atmospheric drag by implementing the analytical results of King-Hele [40] in MATLAB. The Monte Carlo simulation involves the NRLMSISE-00 density model [59]. We find that the STT is an efficient method of uncertainty propagation even when non-conservative forces exist in the dynamics.

Analytically expressed pdfs can be incorporated in many practical tasks in SSA. One can compute the mean and covariance of the uncertainty, for example, with the moments of the initial pdf as inputs. This process does not involve any sampling and, under two-body dynamics, its accuracy can be determined *a priori*. Analytical pdfs may also be incorporated in a non-linear Bayesian estimator for orbit determination and conjunction assessment [76]. Finally, model parameter uncertainty, such as those for atmospheric drag, is readily implemented with little additional computational burden by adding the parameters in the state vector.

## 1.2 Organization and Contributions

We give a brief outline of the organization of this dissertation.

**Chapter 2** *Analytical Non-Linear Propagation of Uncertainty*

The Fokker-Plank equation, STTs, and King-Hele's analytical theory of orbital motion in an atmosphere are first introduced. A closed-form STT solution in the Poincaré orbital element space for the two-body problem, the two-body problem with secular perturbations from $J_2$ gravity field harmonics, and the two-body problem with an analytical atmospheric model are presented. This theoretical framework is implemented numerically in MATLAB. Finally, the prediction error metric as defined by Horwood et al. is computed to determine how well the proposed method maintains uncertainty consistency [33].

**Chapter 3** *Association of Short-Arc Optical Observations via The Direct Bayesian Admissible Region Method*

The too-short arc problem for Earth-orbiters is defined and the AR concept is introduced in this context. Next, the AR is rigorously generalized to be a pdf, which allows one to rationally associate observations via Bayes' rule. Methods of efficiently computing these generalized ARs via linearization and linear extrapolation are shown and demonstrated. Limiting cases of the direct Bayesian approach are acknowledged. Finally, simulated implementations are given for both ground- and space-based observations. Recommendations on orbits for a space-based sensor in the geosynchronous region are made based on the association results.

**Chapter 4** *Addressing Errors in The Direct Bayesian Admissible Region Method*

For ground-based observations, the linear map of a displacement in the attributable vector space to the Poincaré orbital element space is considered in Monte Carlo fashion over a sample set of reference orbits. The direction and magnitude of the mapped displacements are an indication of the "inflation" that occurs when measurement errors are added to the AR. For space-based observations, a simpler analysis focusing on the magnitude of mapped displacements is employed. Finally, we propose two ways to explicitly take into account errors: one where the linear extrapolation map is generalized to higher dimensions, and another where a least squares batch filter is applied to the direct Bayesian results.

**Chapter 5** *Applications to Short-Arc Data at The Astronomical Institute at The University of Bern*

The direct Bayesian admissible region concept is applied to actual optical short arcs of Earth-orbiting objects. In particular, we test the hybrid approach introduced in Section 4.4 on 212 tracklets of geosynchronous (GEO) belt objects taken at the Zimmerwald Observatory of the Astronomical Institute at the University of Bern (AIUB) [68]. Observation capabilities at AIUB, particularly of the ZimSMART telescope, are discussed. The association results are compared to the current orbit determination workflow at AIUB, which consists of conventional geometric tracklet correlation and least squares techniques. The results suggest new association possibilities as well as cast light on the fundamental limits of conducting tracklet association based solely on dynamical and geometrical information.

The most relevant previous research and our contributions are described below. As for ARs, Milani et al. first applied the concept to the TSA problem for heliocentric orbits to initialize a multiple hypothesis tracking (MHT) algorithm, where hypotheses are eliminated by minimizing an "attribution penalty" metric in the observable variables [50, 51]. Tommei et al. expanded this method to Earth orbiting objects [82]. The AR as an MHT initializer has also been studied by DeMars et al., Li et al., and Gadaleta et al [12,21,41]. On the other hand, instead of a brute force method, Farnocchia et al. proposed the use of constants of motion to find the most relevant orbit solutions in the AR [15]. Maruskin et al. introduced another method that maps the AR to Delaunay orbital element space as 2-dimensional projections [46], and DeMars and Jah reformulated orbit determination using ARs as a Gaussian mixture unscented Kalman filter (GMUKF) [11]. Our method maps the 2-dimensional AR to the full 6-dimensional Poincaré space; sparseness of the space allows for much faster association of observations and convergence upon the orbit estimate. Furthermore, since the maps can be performed numerically, we do not have to rely on a two-body assumption or purely analytical solutions to the dynamics. Table 1.1 is a summary of the above.

As for the analytical non-linear propagation of uncertainty via STTs, we expand upon the work by Park and Scheeres [56, 57]. We generalize STTs to any arbitrary order and apply this result to two-body dynamics. Furthermore, the calculations are done in orbital element space, in which uncertainties remains

Table 1.1: Contribution of existing work and thesis work on track association and initial orbit determination with admissible regions.

| **Existing Work** | **Contribution of Existing Work** | **Contribution of Thesis Work** |
|---|---|---|
| DeMars, et al. [12]<br>Gadaleta, et al. [21]<br>Li, et al. [41]<br>Milani, et al. [50, 51]<br>Tommei, et al. [82] | Applied the admissible region to initialize a multiple hypothesis tracking algorithm | Direct application of Bayes rule by exploiting the sparseness of the admissible region in state space |
| DeMars and Jah [11] | Expressed and filtered the admissible region via a Gaussian mixture model | |
| Farnocchia et al. [15]<br>Maruskin et al. [46] | Discussed methods of directly finding consistent solutions between tracklets | Rigorous propagation of uncertainty in a deterministic system allows for fast convergence to an orbit solution |

close to linear for longer than the cartesian space [38, 39]. Finally, in light of SSA, perturbations most relevant to Earth-orbiting objects are analytically presented, such as the secular effects of the $J_2$ spherical harmonics term and atmospheric drag. With respect to the other non-linear uncertainty propagation and filtering methods mentioned in Section 1.1.2, the STT method improves computational turnaround as the propagation is a one-time calculation. Furthermore, probability cumulants and moments are given analytically instead of via sampling. Table 1.2 is a summary of the above.

Table 1.2: Contribution of existing work and thesis work on the non-linear propagation of uncertainty in astrodynamics.

| **Existing Work** | **Contribution of Existing Work** | **Contribution of Thesis Research** |
|---|---|---|
| Park and Scheeres [56, 57] | State transition tensors defined in cartesian coordinates and propagated under Hamiltonian dynamics | Method expanded to deterministic systems defined in an orbital element space |
| DeMars [10]<br>Giza, et al. [22]<br>Horwood, et al. [35] | Applied Gaussian mixture models to non-linear propagation of uncertainty in astrodynamics | Improve computational turnaround in both uncertainty propagation and probability cumulant / moment computation by leveraging analytical techniques |
| Horwood, et al. [34]<br>Jia, et al. [36] | Applied quadrature methods to ... | |
| Horwood, et al. [33] | Applied Edgeworth filters to ... | |
| Jones, et al. [37] | Applied polynomial chaos to ... | |

What we aim to accomplish with the above contributions is to better utilize information content of short tracks and of the dynamical system in order to better express the current and future state uncertainty of Earth-orbiting objects. Unlike most tracking problems, SSA is a data-starved problem in that new observations of objects may not be available for days, if not weeks [33]. Therefore, in maintaining an accurate catalogue of objects in Earth orbit, it is absolutely crucial to maximize the amount of information extracted from each observation so that track association and correlation (with said catalogue) is in a timely manner. In addition, the dynamical system can be very well modeled as mentioned in Section 1.1.2, which may further supply information useful not only for track association / correlation but also for conjunction analysis.

Another goal is to quantitatively describe *how* accurate the mathematical description of the dynamics must be given a certain level of state uncertainty. Qualitatively, we understand that it is pointless to prop-

agate an object's state with extreme accuracy when its uncertainty is high [83]. We believe that analytical uncertainty propagation allows for a definite measure of modeling accuracy via STT order. By implementing a model representative of the actual near-Earth space environment as discussed previously, we take the first step in a quantitative understanding of this phenomenon, leading to automated and efficient propagation of uncertainty.

# Chapter 2

## Analytical Non-Linear Propagation of Uncertainty

One analytical approach of non-linear uncertainty propagation is to employ a special solution to the Fokker-Planck differential equations for deterministic dynamical systems. Given an analytical expression of the pdf, time propagation is extremely efficient as it is only a matter of changing the time parameter. The dynamics are expressed as a Taylor series expansion up to arbitrary order via state transition tensors (STTs) [45, 56]. In this chapter, this approach is detailed in orbital element space. In particular, ways to express, analytically and for all time, the probability density function (pdf) over Keplerian or Poincaré space is discussed. In order to describe the evolution of a pdf over time for a dynamical system with no diffusion, one only needs to find the solution flow to the dynamics regardless of whether the forces are conservative or not. As an example, the evolution of uncertainty for an Earth-orbiting object influenced by two-body gravity is investigated, followed by individual analyses with the effects of secular $J_2$, and atmospheric drag implementing the analytical results of King-Hele [40].

The outline of this chapter is as follows. Necessary mathematical concepts are first introduced, such as the Fokker-Plank equation, STTs, and King-Hele's analytical theory of orbital motion in an atmosphere. A closed-form STT solution in orbital element space for the two-body problem, the two-body problem with secular perturbations from $J_2$ gravity field harmonics, and the two-body problem with an analytical atmospheric model are presented. This theoretical framework is implemented numerically in MATLAB. For a circular orbit, the 3-$\sigma$ error ellipsoid, mean, and covariance of a Gaussian distribution in both state and parameter space is propagated using the STT approach. The 3-$\sigma$ ellipsoid is also propagated for slightly elliptic orbits. These results are compared with those obtained from Monte Carlo simulations. Finally,

the prediction error metric as defined by Horwood et al. is computed to determine how well the proposed method maintains uncertainty consistency [33]. It is found that the STT is an efficient method of uncertainty propagation even when non-conservative forces exist in the dynamics.

## 2.1 Solution of the Fokker-Planck Equation For a Deterministic Dynamical System

Suppose the dynamics of some system is expressed as

$$\dot{\mathbf{X}} = \boldsymbol{f}(t, \mathbf{X}), \tag{2.1}$$

where $\mathbf{X}$ is the state vector and $\boldsymbol{f}$ are the equations of motion [56]. Then, the solution of Eq. (2.1) is expressed as

$$\mathbf{X}(t) = \boldsymbol{\phi}(t; \mathbf{X}^0, t^0), \tag{2.2}$$

where $\mathbf{X}^0$ is the initial state at time $t^0$. $\boldsymbol{\phi}$ must satisfy the following conditions

$$\frac{\mathrm{d}\boldsymbol{\phi}}{\mathrm{d}t} = \boldsymbol{f}(t, \boldsymbol{\phi}(t; \mathbf{X}^0, t)) \tag{2.3}$$

$$\boldsymbol{\phi}(t^0; \mathbf{X}^0, t^0) = \mathbf{X}^0. \tag{2.4}$$

One can define the inverse solution flow $\boldsymbol{\psi}(t, \mathbf{X}; t^0)$

$$\mathbf{X}^0 = \boldsymbol{\psi}(t, \mathbf{X}; t^0) \tag{2.5}$$

which maps a current state back to the initial epoch. For a general solution flow, the inverse flow can be found by interchanging the initial and final states

$$\boldsymbol{\psi}(t, \mathbf{X}; t^0) = \boldsymbol{\phi}(t^0; \mathbf{X}, t). \tag{2.6}$$

For a system that satisfies the Itô stochastic differential equation, the time evolution of a pdf $p(\mathbf{X}, t)$ over $\mathbf{X}$ at time $t$ is described by the Fokker-Planck equation [47]

$$\frac{\partial p(\mathbf{X}, t)}{\partial t} = -\sum_{i=1}^{n} \frac{\partial}{\partial \mathbf{X}_i} \{p(\mathbf{X}, t) \boldsymbol{f}_i(\mathbf{X}, t)\} + \frac{1}{2} \sum_{i=1}^{n} \sum_{j=1}^{n} \frac{\partial^2}{\partial \mathbf{X}_i \partial \mathbf{X}_j} \left[ p(\mathbf{X}, t) \left\{ G(\mathbf{X}, t) Q(t) G^{\mathrm{T}}(\mathbf{X}, t) \right\}_{ij} \right], \tag{2.7}$$

where a single subscript indicates vector components and a double subscript indicates matrix components. Matrices $G$ and $Q$ characterize the diffusion. For a deterministic dynamical system, whether or not it is

Hamiltonian, it can be shown that the probability $\Pr(\mathbf{X} \in \mathcal{B})$ over some volume $\mathcal{B}$ in phase space is an integral invariant [56, 66, 67]

$$\Pr(\mathbf{X} \in \mathcal{B}) = \int_{\mathcal{B}} p[\mathbf{X}(t)]\mathrm{d}\mathbf{X} = \int_{\mathcal{B}^0} p[\boldsymbol{\phi}(t; \mathbf{X}^0, t^0)] \left| \frac{\partial \mathbf{X}}{\partial \mathbf{X}^0} \right| \mathrm{d}\mathbf{X}^0 = \int_{\mathcal{B}^0} p(\mathbf{X}^0)\mathrm{d}\mathbf{X}^0, \tag{2.8}$$

where $p[\mathbf{X}(t)]$ is the probability density function (pdf), $\mathcal{B}^0$ is the volume that corresponds to $\mathcal{B}$ at the initial time, and $|\cdot|$ is the determinant operator. Consequently, [6]

$$p[\boldsymbol{\phi}(t; \mathbf{X}^0, t^0)] = p(\mathbf{X}^0) \left| \frac{\partial \mathbf{X}}{\partial \mathbf{X}^0} \right|^{-1}. \tag{2.9}$$

The inverse of the determinant makes up for the change in phase volume due to the non-conservative forces in the system. For a Hamiltonian system, $|\partial \mathbf{X}/\partial \mathbf{X}^0| = 1$ from Liouville's theorem (i.e. phase volume is conserved), so

$$p[\boldsymbol{\phi}(t; \mathbf{X}^0, t^0)] = p(\mathbf{X}^0). \tag{2.10}$$

Note that for any deterministic system, as long as both the solution flow of the dynamics and the initial pdf are known analytically, the pdf for all time can also be expressed analytically. If one cannot obtain an analytical solution flow, it nevertheless may be approximated by a Taylor series expansion via STTs; details on this method are explained in subsequent sections.

Analytical expressions of the pdf are useful because propagation is then only a matter of changing the time parameter $t$. In particular, if the initial pdf is an $n$-dimensional Gaussian distribution

$$p(\mathbf{X}^0) = \frac{1}{\sqrt{(2\pi)^{2n}|[P^0]|}} \exp\left\{ \frac{1}{2} (\mathbf{X}^0 - \mathbf{M}^0)^T [P^0]^{-1} (\mathbf{X}^0 - \mathbf{M}^0) \right\}, \tag{2.11}$$

where the brackets indicate a matrix, $\mathbf{M}^0$ is the initial mean of the Gaussian, and $[P^0]$ is the initial covariance matrix. Then, the pdf at time $t$ is

$$p[\mathbf{X}(t)] = \frac{1}{\sqrt{(2\pi)^{2n}|[P^0]|}} \exp\left\{ \frac{1}{2} (\boldsymbol{\psi}(t, \mathbf{X}; t^0) - \mathbf{M}^0)^T [P^0]^{-1} (\boldsymbol{\psi}(t, \mathbf{X}; t^0) - \mathbf{M}^0) \right\}, \tag{2.12}$$

since $\mathbf{M}^0$ and $[P^0]$ are initial parameters of the system and are constants.

### 2.1.1 Prediction Error as an Uncertainty Consistency Metric

In the classical approach to statistical orbit determination, such as the Kalman filter, the uncertainty is modeled as a Gaussian distribution and propagated linearly about a reference trajectory [79]. The mean

of the state deviation, if assumed to be on the reference orbit, is zero for all time, and the covariance matrix $[P](t)$ is propagated with the state transition matrix $[\Phi](t, t^0)$

$$[P](t) = [\Phi](t, t^0) \circ [P^0] \circ [\Phi]^{\mathrm{T}}(t, t^0). \tag{2.13}$$

All higher order moments and cumulants are 0 for all time. Although this approach is mathematically well-studied and easy to implement, the assumption that the dynamics are linear has been shown to break down even after one orbit for an object in low Earth orbit (LEO), depending on the coordinate system used [38, 39]. The propagated uncertainty is then no longer an "accurate reflection of the discrepancy from truth exhibited by an estimated state" [33] due to the non-linearity of the dynamics [56]. That is, the uncertainty is *inconsistent*.

To distinguish the validity of various linear and non-linear uncertainty propagation techniques, Horwood et al. have proposed a simple online uncertainty consistency metric called the *prediction error* $\mathcal{PE}(t)$ that is defined as follows [33]

$$\mathcal{PE}(t) = \int p_1[\mathbf{X}(t)] p_2[\mathbf{X}(t)] \mathrm{d}\mathbf{X}, \tag{2.14}$$

where $p_1$ and $p_2$ are two arbitrary pdfs, and the integration is over the entire state space. Again, from Eq. (2.10), $\mathcal{PE}(t)$ should be time-independent assuming a deterministic Hamiltonian dynamical system and consistent uncertainty propagation. In Section 2.4.3, this metric is used to quantify the consistency of uncertainty propagation for the proposed method using solutions to the Fokker-Planck equation versus the classical linear propagation.

### 2.1.2 Example: Damped Harmonic Oscillator

As an example, the propagation of uncertainty is considered for the 1-D damped harmonic oscillator

$$\dot{x} = u \tag{2.15}$$

$$\dot{u} = -kx + \beta u, \tag{2.16}$$

where $k = 1$ and $\beta = 1$ are coefficients. The reference initial state is $\mathbf{X}^0 = (x, u) = (5, 0)$. The uncertainty is Gaussian and the standard deviation for each state variable is $\sigma_x = 1$, $\sigma_u = 0.1$. Figure 2.1 and Table 2.1 represent both the pdf and the local probability propagated over time. The pdf is computed as follows.

(1) The initial pdf is sampled at 2500 points such that each point is within the 3-$\sigma$ uncertainty ellipse.

(2) Each sample point is propagated by time $t$ according to Eqs. (2.15) and (2.16).

(3) The pdf is evaluated at the propagated points with Eq. (2.9).

This method is valid since probability is an integral invariant; i.e., the propagated region in state space corresponding to the initial 3-$\sigma$ ellipse will continue to contain a constant percentage of possible state outcomes. The local probability is approximated by multiplying the pdf at each sample point by the area of the polygon defined by its four adjacent points. The pdf indeed increases in value to compensate for the loss

Table 2.1: The sum over state space (Sum), the maximum value (Max), and the position of the maximum propagated back to the initial time ($\mathbf{X}^{0,\text{Max}} = (x, u)$) for both the pdf and the probability as a function of time. The Jacobian determinant at each time is also noted ($|\partial\mathbf{X}/\partial\mathbf{X}^0|$).

| **Time** | **Pdf** | | | **Probability** | | | $\lvert\partial\mathbf{X}/\partial\mathbf{X}^0\rvert$ |
|---|---|---|---|---|---|---|---|
| | Sum | Max | $\mathbf{X}^{0,\text{Max}}$ | Sum | Max | $\mathbf{X}^{0,\text{Max}}$ | |
| 0 | 6.907.E+2 | 1.592.E+0 | $(5, 0)$ | 0.9945 | 0.002292 | $(5, 0)$ | 1.000.E+0 |
| 1 | 1.877.E+3 | 4.326.E+0 | $(5, 0)$ | 0.9945 | 0.002292 | $(5, 0)$ | 3.679.E-1 |
| 2 | 5.103.E+3 | 1.176.E+1 | $(5, 0)$ | 0.9945 | 0.002292 | $(5, 0)$ | 1.353.E-1 |
| 5 | 1.025.E+5 | 2.362.E+2 | $(5, 0)$ | 0.9945 | 0.002292 | $(5, 0)$ | 6.738.E-3 |
| 10 | 1.521.E+7 | 3.506.E+4 | $(5, 0)$ | 0.9945 | 0.002292 | $(5, 0)$ | 4.540.E-5 |

of phase volume whereas the local probability remains constant.

## 2.2 Non-Linear Mapping of System Dynamics Using State Transition Tensors

One method of obtaining an analytical, non-linear approximation to the solution flow $\boldsymbol{\phi}(t; \mathbf{X}^0, t^0)$ is to use a concept called the *state transition tensor* (STT). If one takes a Taylor series expansion of the solution function Eq. (2.2) about some reference trajectory $\mathbf{X}^*$, the state deviation $\mathbf{x} = \mathbf{X} - \mathbf{X}^*$ is found as

$$\mathbf{x}_i(t) = \sum_{p=1}^{m} \frac{1}{p!} \Phi_{i,k_1 \ldots k_p} \mathbf{x}^0_{k_1} \ldots \mathbf{x}^0_{k_p}, \tag{2.17}$$

where the subscripts indicate the component of each tensor, $m$ is the order of the expansion and $\Phi$ is the STT of order $p$ [45, 56]. Einstein's summation notation is used, and the comma in the subscript simply denotes

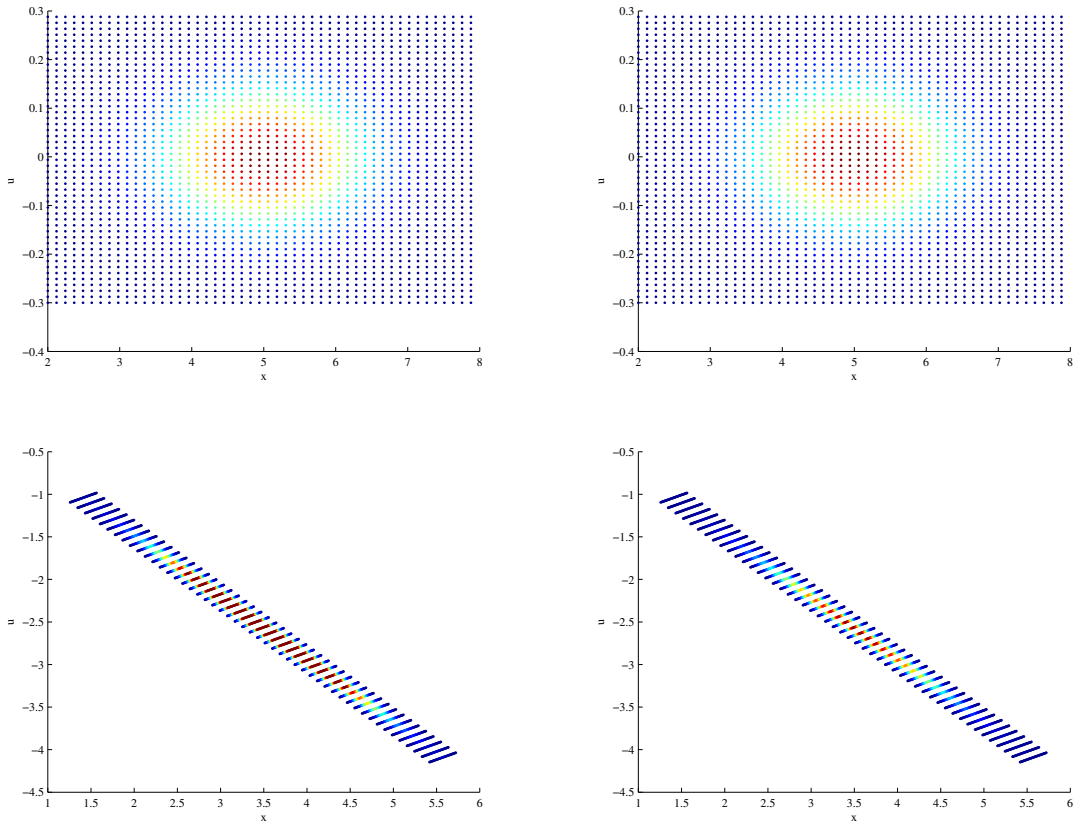


Figure 2.1: The evolution of the probability density function (left) and local probability (right) for a 1-D damped harmonic oscillator. Top figures are for $t = 0$, bottom figures are for $t = 0.909$. For each data type, the coloring is such that any value larger than maximum value at the initial time corresponds to a dark red.

that the $i$-th component is not summed over. Note that the STT is a generalization of the state transition matrix (STM) to any arbitrary order. For $m = 1$, one finds the familiar result

$$\mathbf{x}_i(t) = \Phi_{i,k_1}\mathbf{x}^0_{k_1} \Rightarrow \mathbf{x}(t) = [\Phi]\mathbf{x}^0. \tag{2.18}$$

Given the solution flow $\boldsymbol{\phi}$, the STT can be solved for

$$\Phi_{i,k_1\ldots k_p} = \left.\frac{\partial^p \mathbf{X}_i}{\partial \mathbf{X}^0_{k_1}\ldots\partial \mathbf{X}^0_{k_p}}\right|_*, \tag{2.19}$$

where the * indicates that $\Phi$ is evaluated over the reference trajectory $\mathbf{X}^*$. If $\mathbf{X}$ is not given as a function of $\mathbf{X}^0$, then the following differential equation is solved

$$\dot{\Phi}_{i,k_1\ldots k_p} = G(A_{i,k_1},\ldots,A_{i,k_1\ldots k_p};\Phi_{i,k_1},\ldots,\Phi_{i,k_1\ldots k_p}), \tag{2.20}$$

where

$$A_{i,k_1\ldots k_p} = \left.\frac{\partial^p \boldsymbol{f}_i}{\partial \mathbf{X}_{k_1}\ldots\mathbf{X}_{k_p}}\right|_* \tag{2.21}$$

is the local dynamics tensor (LDT), and $G$ is a function described as follows. Each term in $G$ is a product of an LDT and STTs so that

- the sum of the orders of the STTs add up to $p$
- the number of STTs in the term is equal to the order of the LDT

For instance, for $p = 5$, terms of the form

- $A_{i,l_1}\Phi_{l_1,k_1k_2k_3k_4k_5}\ \langle 1\rangle$
- $A_{i,l_1l_2}\Phi_{l_1,k_1k_2k_3k_4}\Phi_{l_2,k_5}\ \langle 5\rangle$; $A_{i,l_1l_2}\Phi_{l_1,k_1k_2k_3}\Phi_{l_2,k_4k_5}\ \langle 10\rangle$
- $A_{i,l_1l_2l_3}\Phi_{l_1,k_1}\Phi_{l_2,k_2}\Phi_{l_3,k_3k_4k_5}\ \langle 10\rangle$; $A_{i,l_1l_2l_3}\Phi_{l_1,k_1}\Phi_{l_2,k_2k_3}\Phi_{l_3,k_4k_5}\ \langle 15\rangle$
- $A_{i,l_1l_2l_3l_4}\Phi_{l_1,k_1}\Phi_{l_2,k_2}\Phi_{l_3,k_3}\Phi_{l_4,k_4k_5}\ \langle 10\rangle$
- $A_{i,l_1l_2l_3l_4l_5}\Phi_{l_1,k_1}\Phi_{l_2,k_2}\Phi_{l_3,k_3}\Phi_{l_4,k_4}\Phi_{l_5,k_5}\ \langle 1\rangle$

appear, where the number in $\langle\cdot\rangle$ is the number for permutations of $k_1,\ldots,k_p$ that exist; e.g. for $A_{i,l_1l_2}\Phi_{l_1,k_1k_2k_3k_4}\Phi_{l_2,k_5}$

$$A_{i,l_1l_2}\Phi_{l_1,k_2k_3k_4k_5}\Phi_{l_2,k_1}, A_{i,l_1l_2}\Phi_{l_1,k_1k_3k_4k_5}\Phi_{l_2,k_2}, A_{i,l_1l_2}\Phi_{l_1,k_1k_2k_4k_5}\Phi_{l_2,k_3},$$
$$A_{i,l_1l_2}\Phi_{l_1,k_1k_2k_3k_5}\Phi_{l_2,k_4}, A_{i,l_1l_2}\Phi_{l_1,k_1k_2k_3k_4}\Phi_{l_2,k_5}. \tag{2.22}$$

$G$ is the sum of all possible forms and permutations mentioned above. Again, for $n = 5$

$$\begin{aligned}
&G(A_{i,k_1},\ldots,A_{i,k_1k_2k_3k_4k_5};\Phi_{i,k_1},\ldots,\Phi_{i,k_1k_2k_3k_4k_5}) = \\
&\quad A_{i,l_1}\Phi_{l_1,k_1k_2k_3k_4k_5} + A_{i,l_1l_2}\Phi_{l_1,k_2k_3k_4k_5}\Phi_{l_2,k_1} + A_{i,l_1l_2}\Phi_{l_1,k_1k_3k_4k_5}\Phi_{l_2,k_2} \\
&+ A_{i,l_1l_2}\Phi_{l_1,k_1k_2k_4k_5}\Phi_{l_2,k_3} + A_{i,l_1l_2}\Phi_{l_1,k_1k_2k_3k_5}\Phi_{l_2,k_4} + A_{i,l_1l_2}\Phi_{l_1,k_1k_2k_3k_4}\Phi_{l_2,k_5} \\
&+ A_{i,l_1l_2}\Phi_{l_1,k_1k_2k_3}\Phi_{l_2,k_4k_5} + \cdots + A_{i,l_1l_2l_3}\Phi_{l_1,k_1}\Phi_{l_2,k_2}\Phi_{l_3,k_3k_4k_5} + \cdots + A_{i,l_1l_2l_3}\Phi_{l_1,k_1}\Phi_{l_2,k_2k_3}\Phi_{l_3,k_4k_5} + \ldots \\
&\quad + A_{i,l_1l_2l_3l_4}\Phi_{l_1,k_1}\Phi_{l_2,k_2}\Phi_{l_3,k_3}\Phi_{l_4,k_4k_5} + \cdots + A_{i,l_1l_2l_3l_4l_5}\Phi_{l_1,k_1}\Phi_{l_2,k_2}\Phi_{l_3,k_3}\Phi_{l_4,k_4}\Phi_{l_5,k_5}.
\end{aligned} \tag{2.23}$$

The initial values for the integration of Eq. (2.20) are $\Phi_{i,a} = 1$ for $i = a$ and 0 for all other entries. $A$ and $G$ are the generalization of the linear dynamics matrix to any arbitrary order. Again, when $m = 1$, one finds the familiar result

$$\dot{\Phi}_{i,k_1} = A_{i,l_1}\Phi_{l_1,k_1} \Rightarrow [\dot{\Phi}] = [A][\Phi]. \tag{2.24}$$

### 2.2.1 Non-Linear Mapping of Probability Cumulants Using State Transition Tensors

Combining results from the above two sections, the mean $\mathbf{M}(t) = \mathbf{m}(t) + \mathbf{X}^*(t)$ of a pdf $p[\mathbf{X}(t)]$ can be propagated non-linearly as

$$\mathbf{M}(t) = \int_\infty \mathbf{X}(t)p[\mathbf{X}(t)]\mathrm{d}\mathbf{X} = \int_\infty \boldsymbol{\phi}(t;\mathbf{X}^0,t^0)p(\mathbf{X}^0)\left|\frac{\partial\mathbf{X}}{\partial\mathbf{X}^0}\right|^{-1}\mathrm{d}\mathbf{X}^0 \tag{2.25}$$

$$\Leftrightarrow \mathbf{m}_i(t) = \sum_{p=1}^{m}\frac{1}{p!}\Phi_{i,k_1\ldots k_p}\int_\infty p(\mathbf{x}^0)\left|\frac{\partial\mathbf{X}}{\partial\mathbf{X}^0}\right|^{-1}\mathbf{x}^0_{k_1}\ldots\mathbf{x}^0_{k_p}\mathrm{d}\mathbf{x}^0. \tag{2.26}$$

Similarly, the covariance matrix is propagated as

$$[P](t) = \int_\infty [\mathbf{X}(t)-\mathbf{M}(t)]^{\mathrm{T}}[\mathbf{X}(t)-\mathbf{M}(t)]p[\mathbf{X}(t)]\mathrm{d}\mathbf{X} \tag{2.27}$$

$$= \int_\infty [\boldsymbol{\phi}(t;\mathbf{X}^0,t^0)-\mathbf{M}(t)]^{\mathrm{T}}[\boldsymbol{\phi}(t;\mathbf{X}^0,t^0)-\mathbf{M}(t)]p(\mathbf{X}^0)\left|\frac{\partial\mathbf{X}}{\partial\mathbf{X}^0}\right|^{-1}\mathrm{d}\mathbf{X}^0 \tag{2.28}$$

$$\Leftrightarrow [P]_{ij}(t) = \left[\sum_{p=1}^{m}\sum_{q=1}^{m}\frac{1}{p!q!}\Phi_{i,k_1\ldots k_p}\Phi_{j,l_1\ldots l_q}\int_{\infty} p(\mathbf{x}^0)\left|\frac{\partial \mathbf{X}}{\partial \mathbf{X}^0}\right|^{-1}\mathbf{x}^0_{k_1}\ldots\mathbf{x}^0_{k_p}\mathbf{x}^0_{l_1}\ldots\mathbf{x}^0_{l_q}\mathrm{d}\mathbf{x}^0\right] - \mathbf{m}_i(t)\mathbf{m}_j(t) \tag{2.29}$$

Again, for Hamiltonian systems, $|\partial\mathbf{X}/\partial\mathbf{X}^0| = 1$, so the results simplifies to

$$\mathbf{m}_i(t) = \sum_{p=1}^{m}\frac{1}{p!}\Phi_{i,k_1\ldots k_p}E\left[\mathbf{x}^0_{k_1}\ldots\mathbf{x}^0_{k_p}\right] \tag{2.30}$$

$$[P]_{ij}(t) = \left(\sum_{p=1}^{m}\sum_{q=1}^{m}\frac{1}{p!q!}\Phi_{i,k_1\ldots k_p}\Phi_{j,l_1\ldots l_q}E\left[\mathbf{x}^0_{k_1}\ldots\mathbf{x}^0_{k_p}\mathbf{x}^0_{l_1}\ldots\mathbf{x}^0_{l_q}\right]\right) - \mathbf{m}_i(t)\mathbf{m}_j(t), \tag{2.31}$$

where $E$ is the expected value operator

$$E[f(\mathbf{x})] = \int_{\infty} f(\mathbf{x})p[\mathbf{x}(t)]\mathrm{d}\mathbf{x}. \tag{2.32}$$

Up to an $2m$ order moment of the initial pdf is required to propagate the covariance matrix, where an $n$-th order moment $\kappa^{i_1\ldots i_n}$ is defined as [34, 48]

$$\kappa^{i_1\ldots i_n} = E[\mathbf{x}_{i_1}\ldots\mathbf{x}_{i_n}]. \tag{2.33}$$

Thus, even for a fourth order dynamics expansion, to propagate the covariance matrix, one requires up to an 8th order moment, which for a 6-dimensional state space is comprised of $6^8 \approx 10^6$ terms. Memory burden may be reduced by exploiting the fact that the moment is a symmetric tensor. Another useful property to speed up computation is as follows. Also define an $n$-th order cumulant $\kappa^{i_1,\ldots,i_n}$ as

$$\kappa^{i_1,\ldots,i_n} = E\left[(\mathbf{x}_{i_1} - \mathbf{m}_{i_1})\ldots(\mathbf{x}_{i_n} - \mathbf{m}_{i_n})\right]. \tag{2.34}$$

Then, the $n$-th order moment can be expressed in terms of cumulants of order up to $n$

$$\kappa^{i_1\ldots i_n} = H(\kappa^{i_1},\ldots,\kappa^{i_1,\ldots,i_n}), \tag{2.35}$$

where $H$ is a function defined similar to the function $G$ of the differential equations of the STT. That is, each term in $H$ is a product of the cumulants such that the sum of their orders add up to $n$. $H$ is the sum of all possible forms and permutations of such terms. For an initial Gaussian distribution, many terms in $H$ drop out as all cumulants of order 3 and greater are 0. In fact, for such a case, an $n$-th order moment can be expressed entirely in terms of the mean and covariance matrix. Despite this simplification, to propagate such a higher order moment still requires high-rank STTs, which acts as a computational block to describing a

pdf in terms of its moments. It must be emphasized that, with this formulation, it is not necessary to compute these higher order moments to determine the pdf at some future time. Rather, computation of these moments is restricted to situations in which they convey some specific meaning or have some specific use, such as initialization of an orbit determination algorithm.

## 2.3 State Transition Tensors of Earth-Orbiters

Motion of satellites in Earth orbit is particularly amenable to having their solution described through analytic or semi-analytic techniques. Even when stronger non-gravitational perturbations such as solar radiation pressure and atmospheric drag are encountered, these perturbations generally have deterministic components that are substantially larger than their time-varying stochastic components, meaning that they can be modeled either numerically or, in some cases, analytically. These facts open the door to the application of analytical or semi-analytical techniques to describe the motion of a satellite, even accounting for uncertainty in model parameters – so long as they do not contain dynamical stochastic variations that dominate the deterministic component. In particular, if an approximate technique is found for describing the dynamics of a satellite over time, such a solution can be applied to a range of important questions related to the dynamical propagation of an object's pdf.

To this end, in this section, the STTs for two-body dynamics, two-body dynamics with averaged $J_2$ gravity field perturbations, and two-body dynamics with King-Hele's equations of motion in an atmosphere are explicitly derived in orbital element space. Although it has been indicated in the previous section how this approach can be applied to general and fully perturbed dynamical systems, in this thesis, it is applied only to systems with analytical solution flows in order to simplify the math considerably.

### 2.3.1 Two-Body Dynamics

In two-body dynamics, the solution flow $\boldsymbol{\phi}(t; \mathbf{X}^0, t^0)$ is given analytically

$$\begin{aligned} \mathfrak{L}(t) &= \mathfrak{L}^0 & \mathfrak{l}(t) &= \mathfrak{l}^0 + \mu^2/(\mathfrak{L}^0)^3(t - t^0) \\ \mathfrak{G}(t) &= \mathfrak{G}^0 & \mathfrak{g}(t) &= \mathfrak{g}^0 \\ \mathfrak{H}(t) &= \mathfrak{H}^0 & \mathfrak{h}(t) &= \mathfrak{h}^0, \end{aligned} \tag{2.36}$$

where $\mu$ is the standard gravitational parameter and $\mathbf{X}(t) = (\mathfrak{L}(t), \mathfrak{l}(t), \mathfrak{G}(t), \mathfrak{g}(t), \mathfrak{H}(t), \mathfrak{h}(t))$ are the Poincaré orbital elements [84]. The Poincaré orbital elements are the canonical counterpart to the non-singular equinoctial orbital elements. Their main advantage is that the variables can be naturally grouped into coordinate-momenta symplectic pairs. Furthermore, they are defined and nonsingular even for circular and zero-inclination orbits. With respect to the Keplerian orbital elements

$$\begin{aligned} \mathfrak{L} &= \sqrt{\mu a} & \mathfrak{l} &= \Omega + \omega + M \\ \mathfrak{G} &= -\mathfrak{g}\tan(\omega + \Omega) & \mathfrak{g} &= \sqrt{2\mathfrak{L}\left(1 - \sqrt{1 - e^2}\right)}\cos(\omega + \Omega) \\ \mathfrak{H} &= -\mathfrak{h}\tan\Omega & \mathfrak{h} &= \sqrt{2\mathfrak{L}\sqrt{1 - e^2}\,(1 - \cos i)}\cos\Omega, \end{aligned} \tag{2.37}$$

where $a$ is the semi-major axis, $e$ is the eccentricity, $i$ is the inclination, $\Omega$ is the right ascension of the ascending node, $\omega$ is the argument of periapsis, and $M$ is the mean anomaly. Since the angular position of an object with respect to the reference line (first point in Aries) is always defined regardless of the shape or orientation of the orbit, $\mathfrak{l}$ is nonsingular. Furthermore, $\mathfrak{g}$, $\mathfrak{h}$, $\mathfrak{G}$, and $\mathfrak{H}$ are defined so that they are driven to 0 for circular ($e = 0$) and zero-inclination ($i = 0$) orbits. The inverse dynamical map $\boldsymbol{\psi}(t, \mathbf{X}; t^0)$ is

$$\begin{aligned} \mathfrak{L}^0(t) &= \mathfrak{L} & \mathfrak{l}^0(t) &= \mathfrak{l} + \mu^2/\mathfrak{L}^3(t^0 - t) \\ \mathfrak{G}^0(t) &= \mathfrak{G} & \mathfrak{g}^0(t) &= \mathfrak{g} \\ \mathfrak{H}^0(t) &= \mathfrak{H} & \mathfrak{h}^0(t) &= \mathfrak{h}. \end{aligned} \tag{2.38}$$

From Eq. (2.36), $\Phi$ is expected to be very sparse as derivatives higher than and including second order for all variables except $\mathfrak{l}$ is 0

$$\Phi_{i,k_1\ldots k_p} = \begin{cases} [(-1)^p \mu^2 (p+2)!\Delta t/2!]/[(\mathfrak{L}^0)^{p+3}] & i = 2 \text{ and } k_1 = k_2 = \cdots = k_p = 1 \\ 1 & p = 1 \text{ and } k_1 = i \\ 0 & \text{elsewhere,} \end{cases} \tag{2.39}$$

where $\Delta t = t - t^0$ is the time duration of the propagation. Similarly, the STT $\Psi$ of order $p$ corresponding to the inverse flow is simply

$$\Psi_{i,k_1\ldots k_p} = \begin{cases} [(-1)^p \mu^2 (p+2)!(-\Delta t)/2!]/[(\mathfrak{L})^{p+3}] & i = 2 \text{ and } k_1 = k_2 = \cdots = k_p = 1 \\ 1 & p = 1 \text{ and } k_1 = i \\ 0 & \text{elsewhere.} \end{cases} \tag{2.40}$$

### 2.3.2 Two-Body Dynamics + Averaged $J_2$ Perturbations

The effects of the averaged (or secular) $J_2$ gravity field perturbations are now added to the above two-body STT. In Keplerian orbital elements, the results are well known [84]

$$\begin{aligned} \dot{a}_{\text{sec}} &= 0 & \dot{\Omega}_{\text{sec}} &= -\frac{3n^0 {r_E}^2 J_2}{2(p^0)^2}\cos i^0 \\ \dot{e}_{\text{sec}} &= 0 & \dot{\omega}_{\text{sec}} &= \frac{3n^0 {r_E}^2 J_2}{4(p^0)^2}\left(4 - 5\sin^2 i^0\right) \\ \dot{i}_{\text{sec}} &= 0 & \dot{M^0}_{\text{sec}} &= \frac{-3n^0 {r_E}^2 J_2 \sqrt{1-(e^0)^2}}{4(p^0)^2}\left(3\sin^2 i^0 - 2\right), \end{aligned} \tag{2.41}$$

where $n^0 = \sqrt{\mu/(a^0)^3}$ is the mean motion, $r_E$ is the radius of the Earth, $p = a^0(1-(e^0)^2)$ is the semi-parameter, and $M^0$ is the mean anomaly at epoch. The superscripts "0" are to emphasize that the above rates are all constant given initial conditions. Therefore

$$\begin{aligned} a(t) &= a^0 & \Omega(t) &= \Omega^0 + \dot{\Omega}_{\text{sec}}\Delta t \\ e(t) &= e^0 & \omega(t) &= \omega^0 + \dot{\omega}_{\text{sec}}\Delta t \\ i(t) &= i^0 & M(t) &= M^0 + \left(n^0 + \dot{M^0}_{\text{sec}}\right)\Delta t. \end{aligned} \tag{2.42}$$

These relationships must be translated to Poincaré orbital elements. To do so, the Delaunay orbital elements $(L, l, G, g, H, h)$ are introduced. With respect to the Keplerian orbital elements, they are defined as

follows [84]:

$$\begin{aligned} L &= \sqrt{\mu a} & l &= M \\ G &= L\sqrt{1-e^2} & g &= \omega \\ H &= G\cos i & h &= \Omega, \end{aligned} \tag{2.43}$$

and with respect to the Poincaré orbital elements

$$\begin{aligned} L &= \mathfrak{L} & l &= \mathfrak{l} + \arctan(\mathfrak{G}/\mathfrak{g}) \\ G &= \mathfrak{L} - \frac{\mathfrak{G}^2+\mathfrak{g}^2}{2} & g &= \arctan(\mathfrak{H}/\mathfrak{h}) - \arctan(\mathfrak{G}/\mathfrak{g}) \\ H &= \mathfrak{L} - \frac{\mathfrak{G}^2+\mathfrak{g}^2+\mathfrak{H}^2+\mathfrak{h}^2}{2} & h &= -\arctan(\mathfrak{H}/\mathfrak{h}). \end{aligned} \tag{2.44}$$

For just this section, the state expressed in Delaunay elements is explicitly denoted as ${}^{D}\mathbf{X}(t)$, in Poincaré elements as ${}^{P}\mathbf{X}(t)$, and their initial states as ${}^{D}\mathbf{X}^0$ and ${}^{P}\mathbf{X}^0$, respectively. The goal in this section, then, is to find ${}^{P}\mathbf{X}(t)$ as a function of ${}^{P}\mathbf{X}^0$. Eq. (2.42) is transformed into Delaunay orbital elements as [46]

$$\begin{aligned} L(t) &= L^0 & l(t) &= l^0 + \left[\frac{-3\mu^4 {r_E}^2 J_2\left\{(G^0)^2 - 3(H^0)^2\right\}}{4(L^0)^4(G^0)^5} + \frac{\mu^2}{(L^0)^3}\right]\Delta t \\ G(t) &= G^0 & g(t) &= g^0 + \left\{\frac{-3\mu^4 {r_E}^2 J_2}{4(L^0)^3(G^0)^4} + \frac{15\mu^4 {r_E}^2 J_2 (H^0)^2}{4(L^0)^3(G^0)^6}\right\}\Delta t \\ H(t) &= H^0 & h(t) &= h^0 - \frac{3\mu^4 {r_E}^2 J_2 H^0}{2(L^0)^3(G^0)^5}\Delta t. \end{aligned} \tag{2.45}$$

At this point, substitute Eq. (2.45) into the inverse relationship of Eq. (2.44)

$$\begin{aligned} \mathfrak{L} &= L & \mathfrak{l} &= l + g + h \\ \mathfrak{G} &= -\mathfrak{g}\tan(h+g) & \mathfrak{g} &= \sqrt{2(L-G)}\cos(h+g) \\ \mathfrak{H} &= -\mathfrak{h}\tan(h) & \mathfrak{h} &= \sqrt{2(G-H)}\cos(h). \end{aligned} \tag{2.46}$$

and further express ${}^{D}\mathbf{X}^0$ in terms of ${}^{P}\mathbf{X}^0$ via Eq. (2.44) to obtain ${}^{P}\mathbf{X}(t)$ as a function of ${}^{P}\mathbf{X}^0$. Then, calculating the STTs is, albeit tedious, algebraic work.

As will be seen in Section 2.4.1.2, the averaged perturbation due to $J_2$ is dynamically slow enough compared to the two-body acceleration such that a first order approximation (i.e., STM) of the perturbing

dynamics is often sufficient to consistently propagate uncertainty. In such a case, a simpler way to compute the STM is to use the chain rule of differentiation

$$\frac{\partial^P \mathbf{X}(t)}{\partial^P \mathbf{X}^0} = \left(\frac{\partial^P \mathbf{X}(t)}{\partial^D \mathbf{X}(t)}\right) \circ \left(\frac{\partial^D \mathbf{X}(t)}{\partial^D \mathbf{X}^0}\right) \circ \left(\frac{\partial^D \mathbf{X}^0}{\partial^P \mathbf{X}^0}\right) \tag{2.47}$$

The first Jacobian matrix is a direct consequence of Eq. (2.46), the second of Eq. (2.45), and the third of Eq. (2.44). The resulting STM does not contain any singularities; refer to Appendix A for details. Again, for the higher order STTs, it is assumed that contributions from the averaged $J_2$ accelerations can be ignored and simply use the two-body solution as in Eq. (2.39).

### 2.3.3 Two-Body Dynamics + Atmospheric Drag

Here, the analytical motion of an object in a circular or slightly elliptic orbit subject to atmospheric drag as derived by King-Hele are introduced [40]. The STTs are then derived in the Keplerian orbital element space. If desired, the results may be mapped into the Poincaré orbital elements via coordinate transformation Eq. (2.37). Some important assumptions are that the atmosphere is spherically symmetrical, the atmospheric density model is exponential with constant parameters in time, the atmosphere rotates at the same angular rate as the Earth, and the Earth's gravitational field is approximated as a point mass. The following initial states and dynamical system parameters are used in this section unless otherwise noted

$$a^0 = 6678.1 \text{ km}, i^0 = 0.26179 \text{ rad}, \omega_E = 7.2722 \times 10^{-5} \text{ rad/s}, \mu = 398600 \,\text{km}^3\text{s}^{-2}, \tag{2.48}$$

where $\omega_E$ is the Earth's rotational rate and $\mu$ is the standard gravitational parameter. The initial orbit period is thus 90.52 minutes. The atmospheric parameters are

$$H = 40 \text{ km}, \rho^* = 10^{-11} \,\text{kg/m}^3, \text{BC} = 10^2 \,\text{kg/m}^2, \tag{2.49}$$

where $H$ is scale height, $\rho$ is atmospheric density, BC is the ballistic coefficient, and in this section, superscript * indicates that the value is at the reference altitude of 300 km; i.e., $a^* = 6678.1$ km.

#### 2.3.3.1 Circular Orbits

For an initial circular orbit, only the semi-major axis, and consequently the mean anomaly, change with time due to drag effects. The semi-major axis is given as a function of time as

$$a(t;a^0) = a^0 + H\ln\left[1 - \frac{2\pi\delta\rho^*(a^0)^2 e^{\beta(a^*-a^0)}t}{HT^0}\right] = a^0 + H\ln(1+\epsilon t), \tag{2.50}$$

where

$$T^0 = 2\pi\sqrt{\frac{(a^0)^3}{\mu}} \tag{2.51}$$

$$\delta = \frac{(1 - a^0\omega_E\sqrt{a^0/\mu}\cos i^0)^2}{\mathrm{BC}} \tag{2.52}$$

$$\epsilon = -\frac{2\pi\delta\rho^*(a^0)^2 e^{\beta(a^*-a^0)}}{HT^0}, \tag{2.53}$$

Next, to find the mean anomaly, the mean motion $n(t)$ is integrated over time

$$M(t;a^0,M^0) = M^0 + \int_0^t n(t)\mathrm{d}\tau = M^0 + \int_0^t \sqrt{\frac{\mu}{a(\tau)^3}}\mathrm{d}\tau. \tag{2.54}$$

Now, for $a \sim 6700$ km and greater, $\epsilon$ is often very small ($\sim 10^{-8}$). Therefore, $n$ may be expanded as a polynomial of $\epsilon$:

$$\frac{n(t)}{\sqrt{\mu}} = \frac{1}{(a^0)^{3/2}} - \frac{3H\epsilon t}{2(a^0)^{5/2}} + O(\epsilon^2), \tag{2.55}$$

which allows for the analytical integration of Eq. (2.54)

$$M \approx M^0 + \sqrt{\frac{\mu}{(a^0)^3}}t - \frac{3H\epsilon}{4}\sqrt{\frac{\mu}{(a^0)^5}}t^2. \tag{2.56}$$

Note that for a 300 km altitude circular orbit, a fourth order expansion of $n$ with respect to $\epsilon$ results in $\sim 10^{-7}$ radian accuracy in mean anomaly ($\sim 10^0$ meter accuracy in in-track position) after 100 periods of the initial orbit; refer to Figure 2.2 for details. The object drops about 2.5 km in altitude over this time.

Regarding the STTs, the only non-zero values are

$$\frac{\partial M}{\partial M^0}, \frac{\partial^i a}{\partial (a^0)^i}, \frac{\partial^i M}{\partial (a^0)^i}, \tag{2.57}$$

where $i$ goes up to the order of the expansion. Since $a(t;a^0)$ and $M(t;a^0,M^0)$ are known explicitly, the STTs can also be solved for via Eq. (2.19). Now, for this system, note that $|\partial\mathbf{X}/\partial\mathbf{X}^0| = \partial a/\partial a^0$, which simplifies

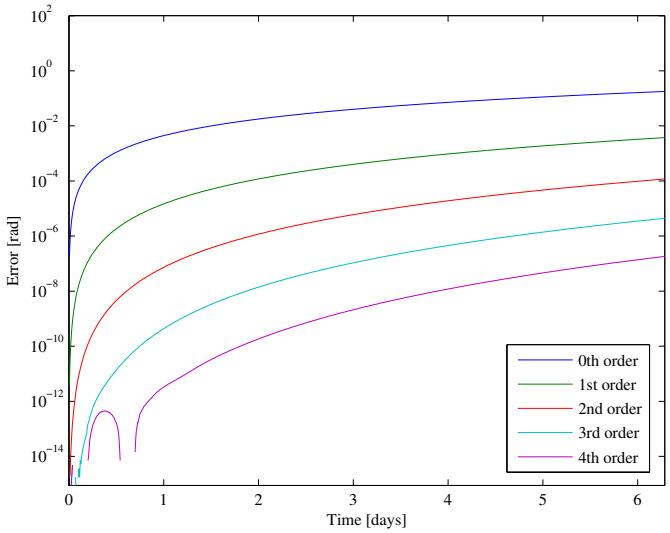


Figure 2.2: The difference in the numerically and analytically integrated mean anomaly (i.e., "Error") for different orders of expansion of mean motion $n$. The reference orbit is a 300 km altitude circular orbit with an inclination of 15°. The errors are plotted for up to 100 orbit periods of the initial orbit.

to the form

$$\frac{\partial a}{\partial a^0} = 1 + \frac{N_1/N_2 - 1}{N_3/N_2\, t^{-1} + 1}, \tag{2.58}$$

where

$$N_1 = \frac{Ha^0}{2}\rho^* \mathrm{e}^{(a^*-a^0)/H}\left[-\sqrt{\frac{\mu}{a^0}}\mu + 8a^0\mu\omega_\mathrm{E}\cos i^0 - 7(a^0)^3\sqrt{\frac{\mu}{a^0}}\omega_\mathrm{E}^2\cos^2 i^0\right] \tag{2.59}$$

$$N_2 = -(a^0)^2\rho^* \mathrm{e}^{(a^*-a^0)/H}\left[\sqrt{\frac{\mu}{a^0}}\mu - 2a^0\mu\omega_\mathrm{E}\cos i^0 + (a^0)^3\sqrt{\frac{\mu}{a^0}}\omega_\mathrm{E}^2\cos^2 i^0\right] \tag{2.60}$$

$$N_3 = a^0 H \mathrm{BC}\mu \tag{2.61}$$

But if one substitute values in Eq. (2.48),

$$\frac{N_1}{N_2} = 0.0018333, \frac{N_3}{N_2} = -8.7877 \times 10^6, \tag{2.62}$$

and so $\partial a/\partial a^0 = 1 + \varepsilon$ for practical values of propagation time $t$, where the absolute value $\|\varepsilon\| \ll 1$. In other words, the change in phase volume is negligible. When the cumulants are to be computed analytically, the problem may be simplified as being Hamiltonian without large errors; refer to Section 2.4.2.2 for details.

If one would like to consider uncertainty in parameter space, such as the ballistic coefficient, the parameters are added as state variables so that the uncertainty of parameters influences that of position and velocity. Again, assuming that atmospheric parameters are constant in time, the dynamics are simply

$$\frac{\mathrm{d}\,\mathrm{BC}}{\mathrm{d}t} = 0. \tag{2.63}$$

The partial derivatives (i.e. STTs) of the states with respect to the ballistic coefficient may still be solved explicitly.

#### 2.3.3.2 Slightly Elliptic Orbits

For an initial elliptic orbit, the semi-major axis, eccentricity, and mean anomaly change with time due to drag effects. Below, the argument is constructed for when $e^0 < 0.2$ and $0 < a^0 e^0/H < 3$ (i.e., near-zero eccentricities), but the steps are similar for when $e^0 < 0.2$ and $a^0 e^0/H > 3$. Future work is to consider highly eccentric orbits which are relevant for missions such as Magnetospheric Multiscale Mission (MMS) [7]. The

eccentricity is given as a function of time as

$$e(t; a^0, e^0) = e^0 \sqrt{1 - \frac{t}{t_L}}, \tag{2.64}$$

where

$$z^0 = \frac{a^0 e^0}{H} \tag{2.65}$$

$$I_1(z) = \frac{\mathrm{e}^z}{\sqrt{2\pi z}} \left(1 - \frac{3}{8z} - \frac{15}{128z^2} - \dots\right) \tag{2.66}$$

$$B = \frac{2\pi}{T^0} \delta \rho_{p^0} a^0 e^0 I_1(z^0) \mathrm{e}^{z^0} \tag{2.67}$$

$$t_L = \frac{(e^0)^2}{2B} \left[1 + \frac{H}{2a^0} \left(1 - \frac{9}{20}(z^0)^2\right)\right]. \tag{2.68}$$

$\rho_{p^0}$ is the atmospheric density at initial periapsis and $I_1(z)$ is the series expansion of the Bessel function of the first kind and first order imaginary argument. The semi-major axis is

$$a(t; a^0, e^0) = a^0 \left(1 - \frac{3H}{2a^0} \ln \frac{z^0 I_1(z^0)}{z I_1(z)}\right)^{2/3}, \tag{2.69}$$

where

$$z = z^0 \sqrt{1 - \frac{t}{t_L}}. \tag{2.70}$$

It is expected that, similar to the circular orbit case, $a$ can be well-approximated as a linear function in time particular for $a \sim 6700$ km or greater. Time no longer appears as a linear term, but nevertheless, one can take $t = 0$ as a reference point

$$M(t; a^0, e^0, M^0) \approx M^0 + \sqrt{\frac{\mu}{(a^0)^3}} t - \frac{1}{2} \left(\left.\frac{\partial n}{\partial t}\right|_0\right) t^2, \tag{2.71}$$

where the subscript 0 indicates that the derivative is evaluated at $t = 0$. All relevant states are now expressed as explicit functions of time and their initial conditions, and thus the STT may be computed analytically as in Eq. (2.19). Although the accuracy of $M$ worsens toward the end of the object's lifetime due to the dominance of the drag force, for an orbit described as Eq. (2.48) except now $e = 0.01$, a fourth order expansion still ensures $\sim 10^1$ meter level accuracy in position (i.e., $\sim 10^{-6}$ radians in mean anomaly) for one day in orbit; refer to Figure 2.3 for details. If higher fidelity is required, one may switch to numerical techniques to compute the STTs [56].

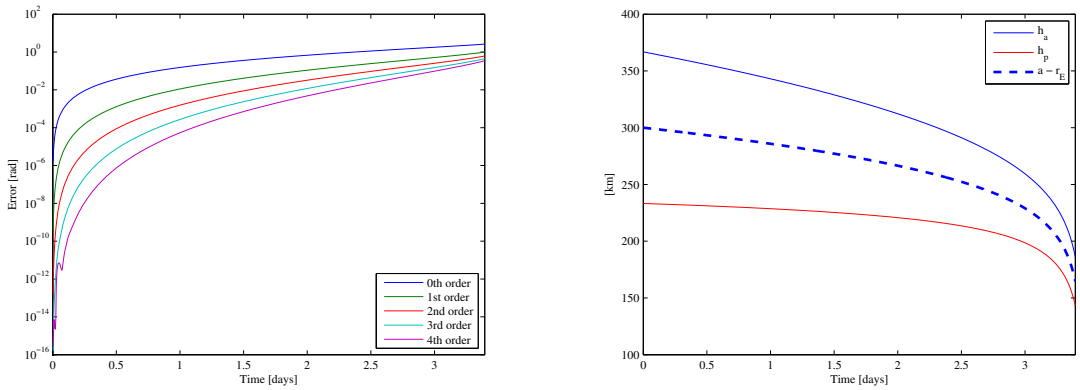


Figure 2.3: For an object with a semi-major axis of 300 km, eccentricity of 0.01, and an inclination of 15°, left: the difference in the numerically and analytically integrated mean anomaly (i.e. "Error") for different orders of expansion of mean motion $n$. Right: the apoapsis ($h_a$) and periapsis ($h_p$) altitude along with semi-major axis minus Earth radii ($a - \mathrm{r_E}$). Both are plotted for up to 54 orbit periods, which is the orbital lifetime of the object.

## 2.4 Simulated Examples

In this section, results of MATLAB implementations of the analytical theory discussed above are shown. A graphical representation is first given through the propagation of the 3-$\sigma$ error ellipse. The propagation of cumulants of the pdf is then explored. Each result is compared to a numerically propagated Monte Carlo (MC) simulation. Unless explicitly stated, the units of numerical values are in the Earth radii - kg - hour system.

### 2.4.1 Propagation of the 3-$\sigma$ Ellipse

In order to show integral invariance of probability for deterministic systems as well as the accuracy of STT approximations derived above, the analytically propagated 3-$\sigma$ bounds of a Gaussian distribution in orbital element (and additionally model parameter) space are compared with propagated points from a sample set of the same distribution.

#### 2.4.1.1 Two-body dynamics

For this example, the classical and Poincaré orbital elements of the truth orbit are given as follows

$$a = 1.09437, e = i = \Omega = \omega = M = 0 \Rightarrow \mathfrak{L} = 4.6679, \mathfrak{l} = \mathfrak{G} = \mathfrak{g} = \mathfrak{H} = \mathfrak{h} = 0. \tag{2.72}$$

The orbit period is 96.73 minutes. For this analysis, only the $\mathfrak{L}$-$\mathfrak{l}$ subspace is considered since only $\mathfrak{l}$ dynamically evolves in the two-body problem and its rate is a function of $\mathfrak{L}$. The initial Gaussian uncertainty is zero-mean, and two cases **(i)** and **(ii)** of initial covariance matrices are considered

$$\textbf{(i)} \quad [P] = \begin{bmatrix} \sigma_{\mathfrak{L}}^2 & \mu_{\mathfrak{L}\mathfrak{l}} \\ \mu_{\mathfrak{L}\mathfrak{l}} & \sigma_{\mathfrak{l}}^2 \end{bmatrix} = \begin{bmatrix} 4.4723 \times 10^{-5} & 0 \\ 0 & 3.0461 \times 10^{-8} \end{bmatrix} \tag{2.73}$$

$$\textbf{(ii)} \quad [P] = \begin{bmatrix} 0.06243 & 0 \\ 0 & 3.0461 \times 10^{-8} \end{bmatrix}. \tag{2.74}$$

The corresponding 1-$\sigma$ uncertainty in the semi-major axis direction is 20 km for case (i) and 745 km for case (ii). Both (i) and (ii) correspond to a 0.01 degree uncertainty in the mean longitude. Although the

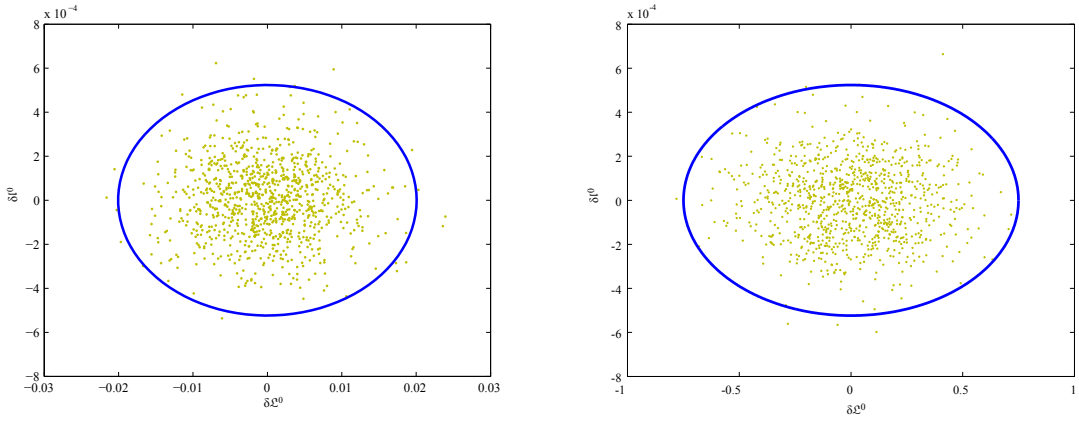


Figure 2.4: Initial Gaussian distribution of the state deviation in the $\Omega^0$-$\imath^0$ plane (sampled with the yellow points) with the corresponding 3-$\sigma$ ellipse (blue curve) for cases (i) (left) and (ii) (right) in Section 2.4.1.1.

uncertainty in case (ii) is unrealistically large, it will be used to show the robustness of the proposed method as well as provide numerical stability in Section 2.4.2.1. For the MC simulation, $10^6$ points distributed to be consistent with the initial uncertainty are generated and propagated using the "complete" two-body dynamics as in Eq. (2.36). For the STT propagation, $10^3$ points are taken on the initial 3-$\sigma$ ellipse and propagated using the "approximate" two-body dynamics as in Eq. (2.39). Figure 2.4 is a representation of these initial distributions.

Figures 2.5-2.6 shows the results of the propagation for case (i). From Eq. (2.10), the propagated 3-$\sigma$ ellipses are expected to still enclose a large number of the propagated MC sample points. Indeed, as the order of the STT used increases, the uncertainty map converges to the MC solution. The 3-$\sigma$ ellipse propagated with first order dynamics encloses a small portion of the MC points, whereas those propagated with higher order STTs continue to enclose a majority. By about second order, the STT approximation is close enough to the full dynamics. Also, the non-linearity grows as the propagation time is made longer, as expected. Figure 2.6 is a representation of the MC results and the propagated 3-$\sigma$ ellipses after 100 orbital periods, or about 161 hours. The second order and higher STTs continue to be sufficient approximations to the complete two-body dynamics even after such long propagation times.

Figure 2.7 shows the results of the propagation for case (ii). Even for such an extreme initial distribution with faster dynamics, the STT propagation, particularly above third order, continues to retain uncer-

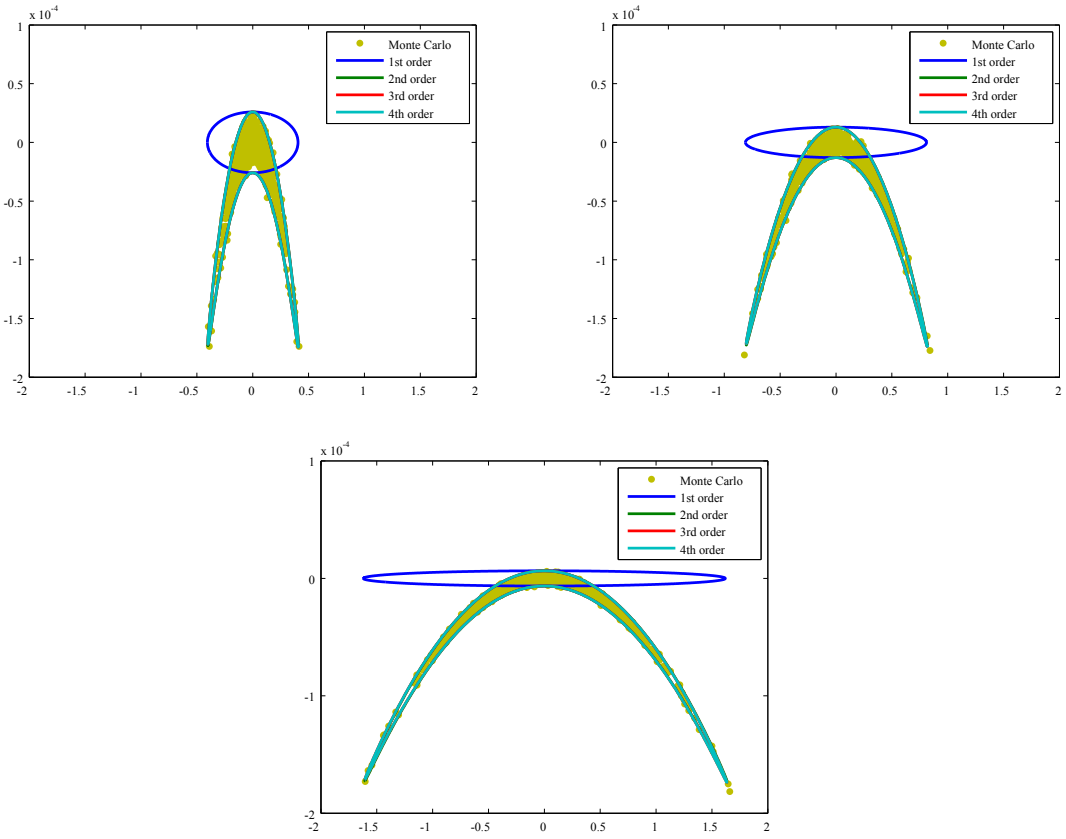


Figure 2.5: The Gaussian distribution of the state deviation propagated for 5 (top left), 10 (top right), and 20 (bottom) orbit periods using various propagation methods for case (i) under two-body dynamics. The $\mathcal{Q}$-I plane is rotated so that the axes of the plot corresponds to the principal axis directions of the linearly propagated ellipse. The second order and higher curves are nearly identical. Points from the Monte Carlo run (labeled "Monte Carlo") represent the "complete" non-linear dynamics. The lines (labeled "$n$ order") represent how the edges of the initial 3-$\sigma$ ellipse propagate with $n$-th order state transition tensors.

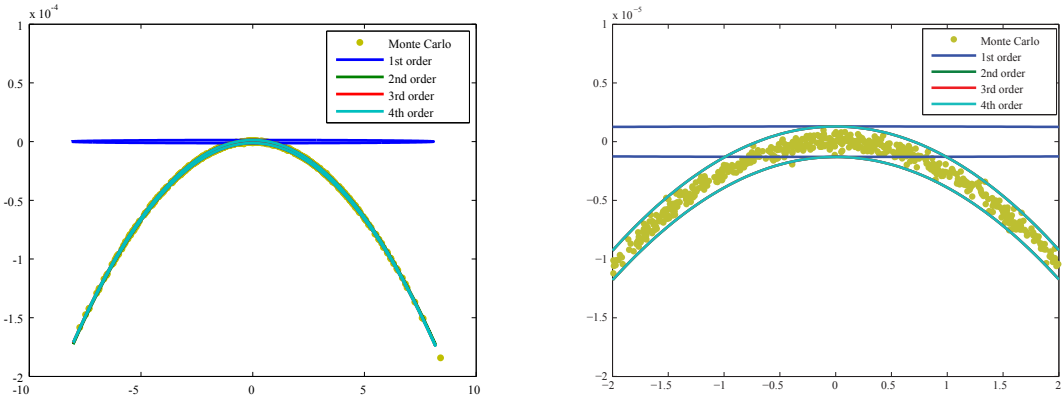


Figure 2.6: The Gaussian distribution of the state deviation propagated for 100 orbital periods using various propagation methods under two-body dynamics. The figures have been rotated as in Figure 2.5. The figure on the right is a zoom up near the origin.

tainty consistency after ~ 161 hours. It is also more clear for this case how the expansion of the dynamics converges upon the true dynamics as one includes higher order effects.

#### 2.4.1.2 Two-Body Dynamics + Averaged $J_2$ Perturbations

For this example, the classical and Poincaré orbital elements of the truth orbit are given as follows

$$a = 1.09437, e = 0.1, i = \pi/6, \Omega = \pi/4, \omega = \pi/3, M = \pi/2 \tag{2.75}$$

$$\Rightarrow \mathfrak{L} = 4.6679, \mathfrak{l} = 3.4034, \mathfrak{G} = -0.20895, \mathfrak{g} = -0.055989, \mathfrak{H} = -0.78882, \mathfrak{h} = 0.78882. \tag{2.76}$$

The orbit period is 96.73 minutes. The analysis is conducted in the full 6-dimensional state space since all Poincaré elements except $\mathfrak{L}$ are functions of time. The initial Gaussian uncertainty is defined in the Keplerian orbital element space and mapped linearly into the Poincaré space. The mean is zero and the covariance matrix is

$$[P] = \text{diag}(\sigma_a^2, \sigma_e^2, \sigma_i^2, \sigma_\Omega^2, \sigma_\omega^2, \sigma_M^2) \tag{2.77}$$

$$= \text{diag}(9.8328 \times 10^{-6}, 2.5 \times 10^{-5}, 3.0462 \times 10^{-6}, 3.0462 \times 10^{-6}, 3.0462 \times 10^{-6}, 3.0462 \times 10^{-8}), \tag{2.78}$$

where diag represents a diagonal matrix. This value corresponds to a 1-$\sigma$ uncertainty of 20 km in $a$; 0.005 in $e$; 0.1 degree in $i$, $\Omega$, and $\omega$; and 0.01 degree in $M$. Figure 2.8 is a representation of this initial distribution in Poincaré space. The data points are generated as follows:

**MC Simulation** $10^4$ points are distributed to be consistent with the initial uncertainty and propagated analytically using the "complete" averaged $J_2$ dynamics as in Eq. (2.41).

**STT Propagation** $3.2 \times 10^6$ points are taken on the initial 3-$\sigma$ hyper-ellipsoid and propagated analytically using the "approximate" averaged $J_2$ dynamics up to first order as in Eq. (2.47).

Figure 2.9 shows the results of the propagation after 20 orbit periods (~ 32 hr). To highlight the effects on the uncertainties due to only the averaged $J_2$ term, the point-mass gravity term is omitted from the dynamics. The dynamics due to the $J_2$ gravity field harmonics are slow enough so that a linear propagation of the uncertainty is consistent. Therefore, oftentimes for the problem of two-body dynamics + averaged $J_2$

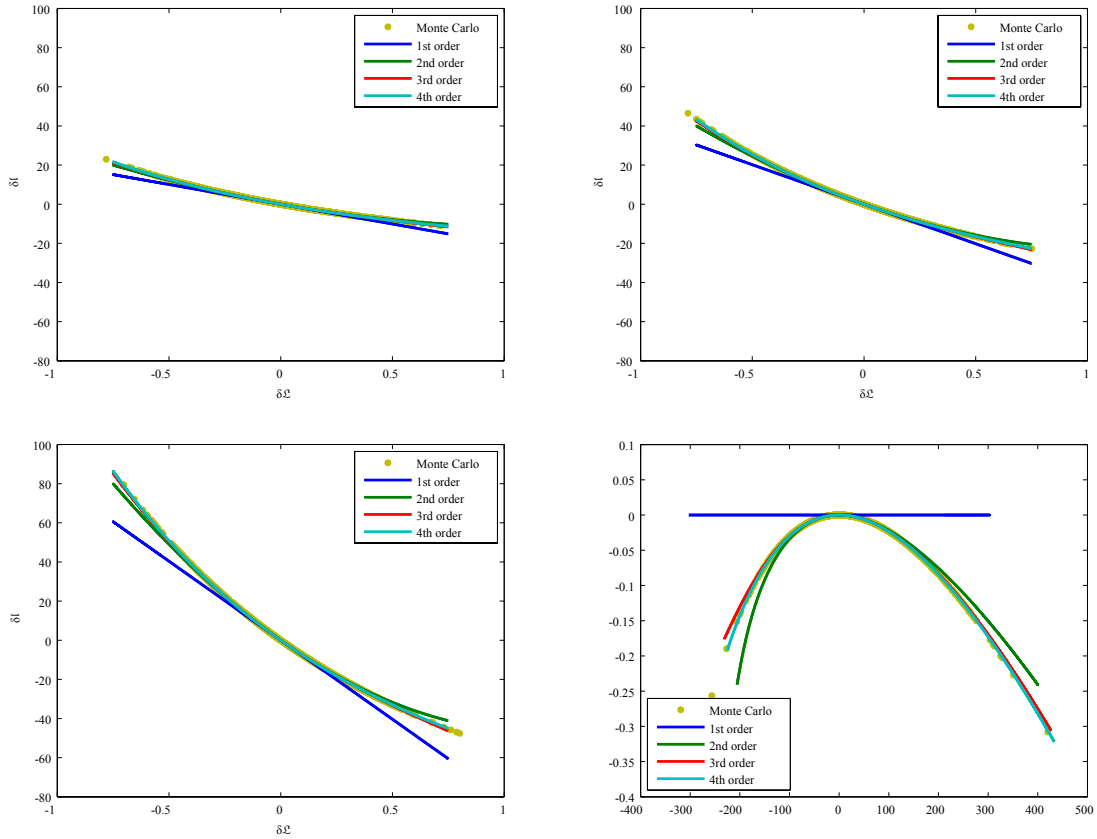


Figure 2.7: The Gaussian distribution of the state deviation propagated for 5 (top left), 10 (top right), 20 (bottom left), and 100 orbit periods (bottom right) using various propagation methods for case (ii) under two-body dynamics. The second order and higher curves are nearly identical. The figure for 100 orbit periods has been rotated as in Figure 2.5.

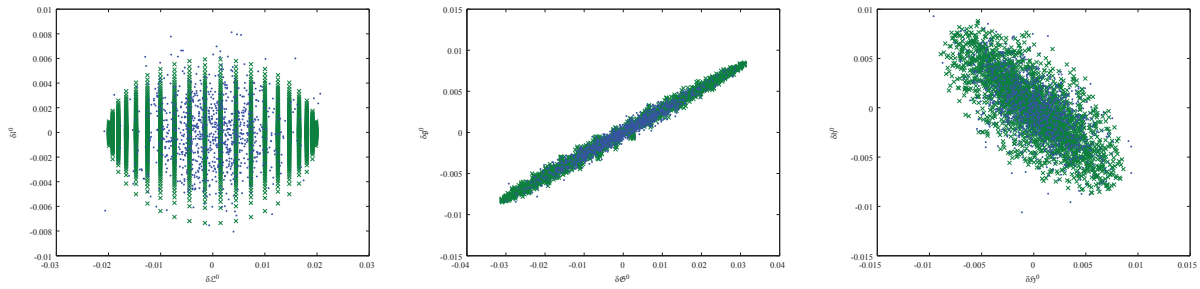

Figure 2.8: Initial Gaussian distribution of the state deviation (sampled with the blue points) projected onto the $\mathfrak{L}^0$-$\mathfrak{l}^0$ (top left), $\mathfrak{G}^0$-$\mathfrak{g}^0$ (top right), and $\mathfrak{H}^0$-$\mathfrak{h}^0$ (bottom) subspaces with the corresponding 3-$\sigma$ hyper-ellipsoid (sampled with green points) in Section 2.4.1.2.

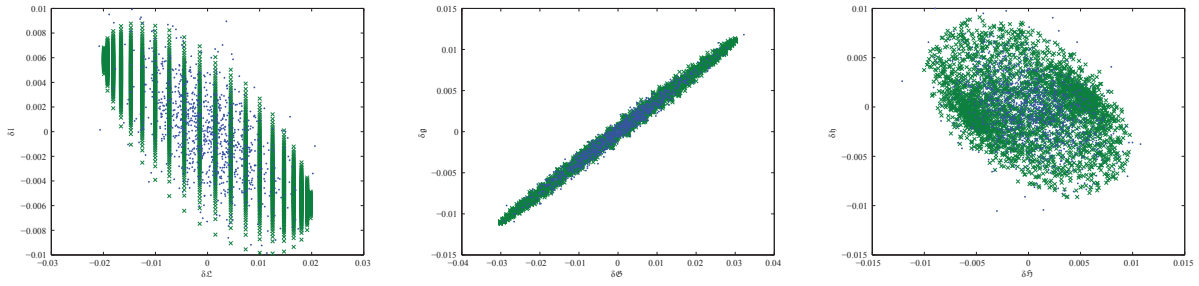

Figure 2.9: The Gaussian distribution of the state deviation propagated for 20 orbital periods under $J_2$ averaged perturbations only and projected onto the $\mathfrak{Q}$-$\mathfrak{I}$ (top left), $\mathfrak{G}$-$\mathfrak{g}$ (top right), and $\mathfrak{H}$-$\mathfrak{h}$ (bottom) subspaces. Monte Carlo results are in blue points and STT propagation results in green points.

perturbations, it is necessary to include second order and higher expansions of only the point-mass gravity term. This is indeed the case in Figure 2.10; when the two-body dynamics are included via STTs up to second order, the MC points remain included in the propagated 3-$\sigma$ hyper-ellipsoid. Note that, here, only the $\mathfrak{Q}$-$\mathfrak{I}$ subspace is shown as all other coordinates are unaffected by the point mass gravity.

#### 2.4.1.3 Two-Body Dynamics + Atmospheric Drag In a Circular Orbit

For the analysis in this section, the semi-major axis ($a$) / mean anomaly ($M$) / ballistic coefficient (BC) space is employed. Note that the results may be mapped one-to-one to the Poincaré orbital element space if desired. The same circular orbit is used as in Eq. (2.48) with BC = $10^2$ kg/m$^2$ as the nominal orbit. Two simulation epoch are tested: February 8, 2009, which will be referred to as *Calm*, and July 11, 2000, referred to as *Storm*, to indicate the intensity of geomagnetic activity. In each case, the uncertainty is propagated for 6.286 days, or 100 orbital periods with the initial semi-major axis. The central body is approximated as a point mass. Figure 2.11 shows the density and $A_p$ geomagnetic index history for both epochs. Figure 2.12 is a representation of the initial distribution in the orbital elements.

The data points are generated as follows. For the MC simulation, 2,000 sample points are first distributed normally in the $a$-$M$ space with a covariance

$$[P] = \begin{bmatrix} \sigma_a^2 & \mu_{aM} \\ & \sigma_M^2 \end{bmatrix} = \begin{bmatrix} (20\text{ km})^2 & 0 \\ & (0.01^\circ)^2 \end{bmatrix}. \tag{2.79}$$

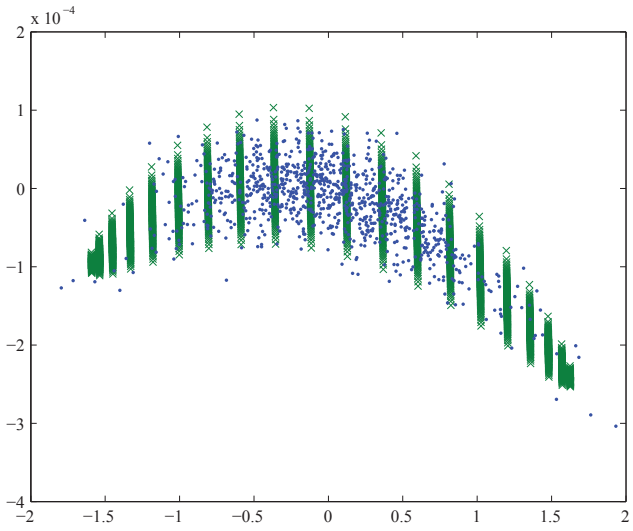


Figure 2.10: The Gaussian distribution of the state deviation propagated for 20 orbital periods using a second order expansion of the two-body dynamics + a first order expansion of the averaged perturbation due to $J_2$. The distribution is projected onto the $\mathfrak{L}$-$\mathfrak{l}$ subspace, then rotated so that the axes of the plot corresponds to the principal axis directions of the propagated covariance matrix. Monte Carlo results are in blue points and state transition tensor propagation results in green points.

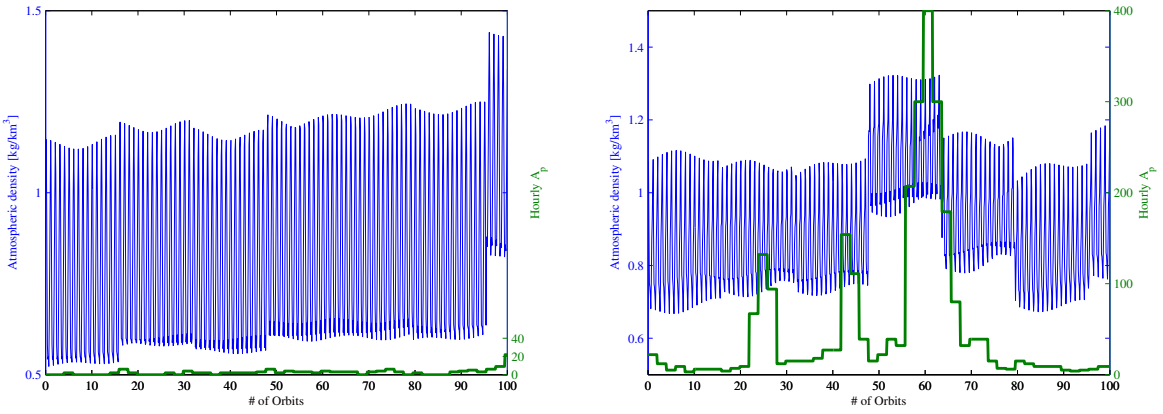


Figure 2.11: Atmospheric density at the reference state as computed by the NRLMSISE-00 model and the hourly $A_p$ index starting February 8, 2009 (left, *Calm*) and July 11, 2000 (right, *Storm*). Units of time are in orbit periods of the initial orbit ($\approx$ 90.52 minutes).

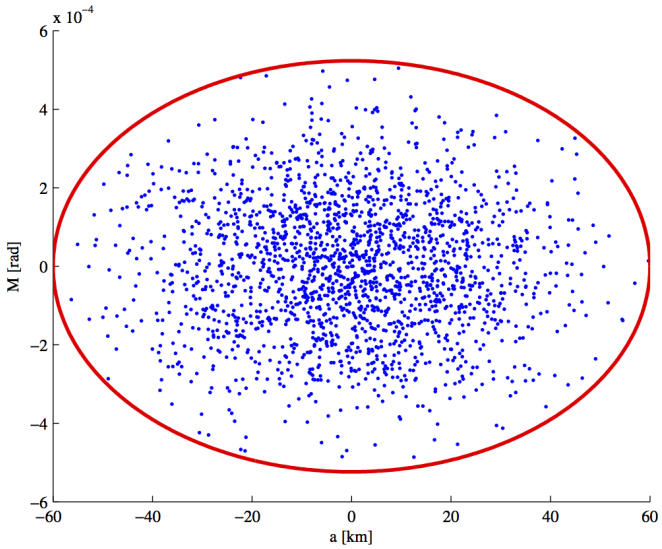


Figure 2.12: Initial Gaussian distribution of the state deviation in the *a*-*M* plane (sampled with the blue points) with the corresponding 3-$\sigma$ ellipse (red curve) in Section 2.4.1.3.

BC changes over time sinusoidally

$$\mathrm{BC}(t) = \mathrm{BC}^0 + A_{\mathrm{BC}} \sin(\frac{2\pi}{\tau_{\mathrm{BC}}} t + \phi_{\mathrm{BC}}), \tag{2.80}$$

and the parameters $A_{\mathrm{BC}} \in [-2{\times}10, 2{\times}10]\,\mathrm{kg/m^2}$, $\tau_{\mathrm{BC}} \in [100, 10000]$ sec, $\phi_{\mathrm{BC}} \in [0, 2\pi]$ are picked randomly for each sample point. The drag accelerations are given as

$$\ddot{\mathbf{r}}_{\mathrm{drag}} = \frac{1}{2\mathrm{BC}} \rho V \mathbf{V}, \tag{2.81}$$

where $\mathbf{V}$ is the relative velocity of the spacecraft relative to the atmosphere. It is assumed that the atmosphere is spherical and rotates at the same rate as the Earth's daily rotation about its axis. The density $\rho$ is simulated with the NRLMSISE-00 model [59].

On the other hand, for the STT propagation, $10^3$ points are taken on the initial 3-$\sigma$ ellipsoid where the uncertainty in the orbital elements is the same as the MC simulation and $\sigma_{\mathrm{BC}} = 5\,\mathrm{kg/m^2}$. Expansion of King-Hele's theory up to fourth order is considered. The reference density $\rho^*$ and scale height $H$ are determined by fitting the NRLMSISE-00 computed densities between altitudes of 240 km and 360 km over the first orbital period. The results are $(\rho^*, H) = (7.262 \cdot 10^{-12}\,\mathrm{kg/km^3}, 36.49\,\mathrm{km})$ for the *Calm* scenario and $(3.897 \cdot 10^{-11}\,\mathrm{kg/km^3}, 55.22\,\mathrm{km})$ for *Storm*. For simplicity, $n$ is expanded only up to first order in $\epsilon$; as found in Section 2.3.3.1, $\sim 10^{-3}$ rad accuracy in mean anomaly is still ensured.

Figure 2.13 shows the results of the propagation. As expected, since probability is an integral invariant regardless of whether the system is conservative, the 3-$\sigma$ curve converges upon the distribution of MC points as the order of the STT is increased. Indeed, due to the highly non-linear nature of the dynamics, many MC points fall outside of the linearly propagated uncertainty ellipsoid. Furthermore, by explicitly accounting for the uncertainty in BC, the analytic model succeeds in capturing the effects of time-varying $\rho$ and BC. This result suggests that even though the drag force is stochastic, it has a dominant deterministic component whose uncertainties are sufficiently expressed as parametric errors. Therefore, computationally efficient analytic techniques are an attractive option for uncertainty propagation.

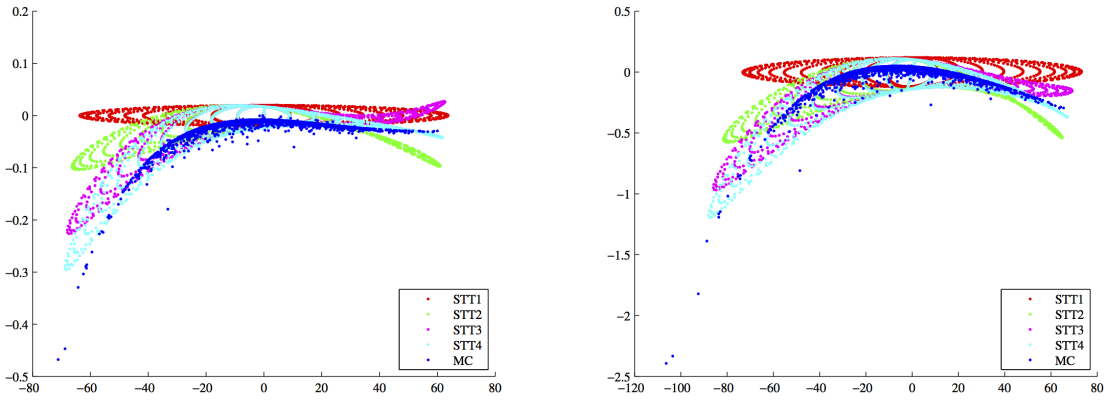


Figure 2.13: An initial Gaussian distribution of the state deviation propagated numerically (MC) and analytically (STT; number indicates expansion order) over 6.286 days under two-body dynamics plus atmospheric drag for the *Calm* (left) and *Storm* (right) scenarios in a circular orbit. The results are projected on the semi-major axis ($a$) / mean anomaly ($M$) space in units of km-rad and subsequently rotated so that the axes of the plot corresponds to the principal axis directions of the linearly propagated ellipse.

#### 2.4.1.4 Two-Body Dynamics + Atmospheric Drag In a Slightly Elliptic Orbit

The analytical propagation an initial Gaussian distribution in the semi-major axis ($a$) / mean anomaly ($M$) / eccentricity ($e$) / ballistic coefficient (BC) space is now demonstrated for slightly elliptic orbits. The same orbit and drag parameters as in the previous section are considered but $e = 0.01$. Due to the shorter orbit lifetime compared to the previous simulation, the uncertainty is propagated for half the time, or 3.143 days. The covariance of the initial uncertainty is

$$[P] = \begin{bmatrix} \sigma_a^2 & \mu_{aM} & \mu ae \\ & \sigma_M^2 & \mu_{Me} \\ & & \sigma_e^2 \end{bmatrix} = \begin{bmatrix} (20\text{ km})^2 & 0 & 0 \\ & (0.01^\circ)^2 & 0 \\ & & 0.0005^2 \end{bmatrix}. \tag{2.82}$$

The reference density $\rho^*$ and scale height $H$ are determined by fitting the NRLMSISE-00 computed densities between altitudes of 150 km and 400 km over the first orbital period. The results are $(\rho^*, H) = (8.337 \cdot 10^{-12}\text{ kg/km}^3, 32.74\text{ km})$ for the *Calm* scenario and $(4.389 \cdot 10^{-11}\text{ kg/km}^3, 48.32\text{ km})$ for *Storm*.

Figure 2.14 and 2.15 show the results of the propagation. Again, the 3-$\sigma$ curve converges upon the distribution of MC points as the order of the STT is increased. Just like the ballistic coefficient, the addition of eccentricity uncertainty "inflates" the $a$-$M$ subspace particularly along the semi-minor axis of the linearly propagated error ellipsoid.

### 2.4.2 Propagation of Probability Cumulants

Here, results of the mean and covariance matrix propagated using STTs and those computed by a Monte Carlo sampling of the uncertainty are compared. Note that for the former, the results are strictly analytical in that no sampling is required; refer to Eqs. (2.30) and (2.31). The first example considers two-body gravity only; analytic relationships are found between the true and STT propagated probability moments which may be computed *a priori*. The second example adds atmospheric drag where, again, the numerical MC simulation includes a realistic drag model.

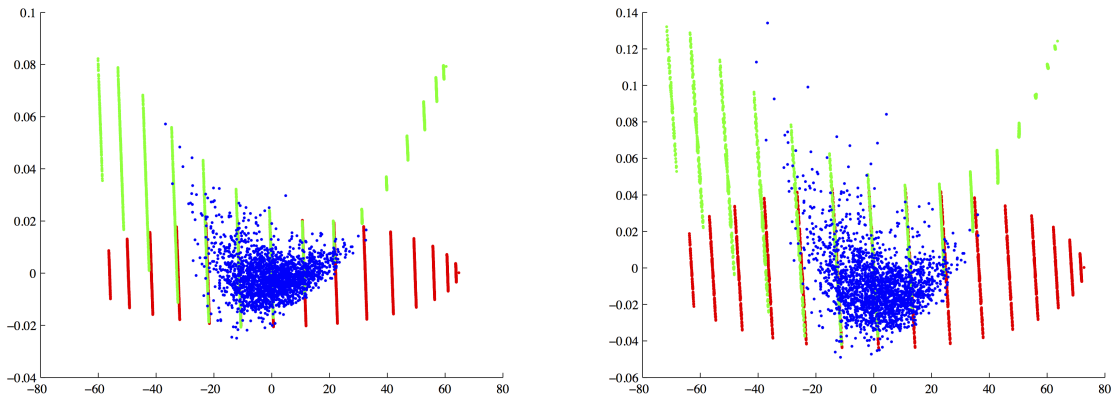

Figure 2.14: An initial Gaussian distribution of the state deviation propagated numerically (blue) and analytically (red: 1st order, green: 2nd order) over 3.143 days for the *Calm* (left) and *Storm* (right) scenarios under two-body dynamics plus atmospheric drag in a slightly elliptic orbit. The results are projected on the semi-major axis ($a$) / mean anomaly ($M$) space in units of km-rad and subsequently rotated so that the axes of the plot corresponds to the principal axis directions of the linearly propagated ellipse.

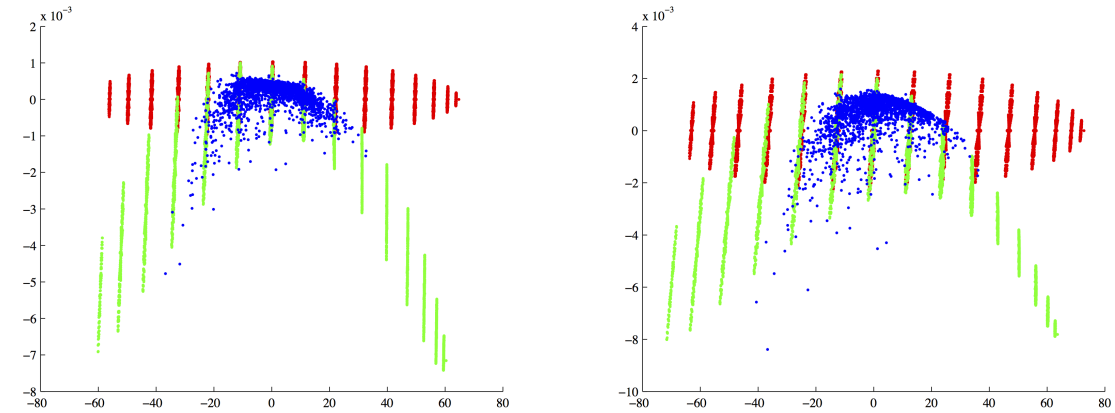

Figure 2.15: Same distribution as Figure 2.14 but the results are projected on the semi-major axis ($a$) / eccentricity ($e$) space in units of km-[ ] and subsequently rotated so that the axes of the plot corresponds to the principal axis directions of the linearly propagated ellipse.

#### 2.4.2.1 Two-Body Dynamics

For this example, the truth trajectory is the same as Eq. (2.72). Solely due to limitations of the random number generator in MATLAB, this initial uncertainty is defined to have an unrealistically large covariance

$$[P] = \begin{bmatrix} \sigma_{\mathfrak{Q}}^2 & \mu_{\mathfrak{Q}\mathfrak{l}} \\ \mu_{\mathfrak{Q}\mathfrak{l}} & \sigma_{\mathfrak{l}}^2 \end{bmatrix} = \begin{bmatrix} 0.06243 & 0 \\ 0 & 3.0461 \times 10^{-8} \end{bmatrix}, \tag{2.83}$$

or case (ii) in Section 2.4.1.1. For the MC results, the mean and covariance matrices from 100 MC runs are averaged, with each run consisting of $10^6$ sample points. Table 2.2 compares the propagated mean after 5, 10, 20, and 100 orbits, and Table 2.3, the covariance matrix.

Table 2.2: The mean $\delta\bar{\mathfrak{l}}$ of the deviation of Poincaré element $\mathfrak{l}$ for different numerical and analytical propagation methods under two-body dynamics. "Δ[%]" indicates relative error with respect to the Monte Carlo results in percentages.

| | **Monte Carlo** | **1st order** | | **2nd order** | | **3rd order** | | **4th order** | |
|---|---|---|---|---|---|---|---|---|---|
| | $\delta\bar{\mathfrak{l}}$ | $\delta\bar{\mathfrak{l}}$ | Δ[%] | $\delta\bar{\mathfrak{l}}$ | Δ[%] | $\delta\bar{\mathfrak{l}}$ | Δ[%] | $\delta\bar{\mathfrak{l}}$ | Δ[%] |
| 5 orbits | 0.5521 | 0 | 100 | 0.5401 | 2.176 | 0.5401 | 2.176 | 0.5517 | 0.074 |
| 10 orbits | 1.1042 | 0 | 100 | 1.0802 | 2.176 | 1.0802 | 2.176 | 1.1034 | 0.074 |
| 20 orbits | 2.2084 | 0 | 100 | 2.1604 | 2.176 | 2.1604 | 2.176 | 2.2068 | 0.074 |
| 100 orbits | 11.042 | 0 | 100 | 10.802 | 2.176 | 10.802 | 2.176 | 11.034 | 0.074 |

The mean changes only in the $\mathfrak{l}$-direction for MC and high order STT propagation, which is expected as two-body dynamics influences only the mean longitude. Similarly, the covariance matrix changes only for the variance of $\mathfrak{l}$ and the covariance between $\mathfrak{Q}$ and $\mathfrak{l}$. The error in the mean and covariance matrix becomes smaller as the order of propagation increases, as expected, but two interesting points are noted. First, the value of the mean is equal when using either second order or third order dynamics. This is because, from Eq. (2.30), the difference between these two orders are the terms that include the initial third order moment of the pdf. Now, if assuming an initial Gaussian distribution, Eq. (2.35) for the third order moment is [56]

$$\kappa^{i_1 i_2 i_3} = \kappa^{i_1}\kappa^{i_2}\kappa^{i_3} + (\kappa^{i_1}\kappa^{i_2,i_3} + \kappa^{i_2}\kappa^{i_1 i_3} + \kappa^{i_3}\kappa^{i_1,i_2}). \tag{2.84}$$

But zero initial mean (i.e., first order cumulant) is also assumed, so $\kappa^{i_1 i_2 i_3} = 0$, and the third order STT does not contribute to the polynomial expansion. In fact, any odd order expansion of the dynamics greater than or equal to order 3 will result in the same propagated mean as the even order expansion of one less order.

Table 2.3: Elements from the covariance matrix for different numerical and analytical propagation methods under two-body dynamics.

| | **Monte Carlo** | | **1st order** | | | | **3rd order** | | | |
|---|---|---|---|---|---|---|---|---|---|---|
| | $\mu_{\mathfrak{l}\mathfrak{Q}}$ | $\sigma^2_{\mathfrak{l}}$ | $\mu_{\mathfrak{l}\mathfrak{Q}}$ | $\Delta[\%]$ | $\sigma^2_{\mathfrak{l}}$ | $\Delta[\%]$ | $\mu_{\mathfrak{l}\mathfrak{Q}}$ | $\Delta[\%]$ | $\sigma^2_{\mathfrak{l}}$ | $\Delta[\%]$ |
| 5 orbits | -1.2975 | 27.626 | -1.2605 | 2.851 | 25.451 | 7.871 | -1.2966 | 0.068 | 27.528 | 0.353 |
| 10 orbits | -2.5951 | 110.50 | -2.5211 | 2.851 | 101.80 | 7.871 | -2.5933 | 0.068 | 110.11 | 0.353 |
| 20 orbits | -5.1902 | 442.01 | -5.0422 | 2.851 | 407.22 | 7.871 | -5.1867 | 0.068 | 440.45 | 0.353 |
| 100 orbits | -25.951 | 11050 | -25.211 | 2.851 | 10181 | 7.871 | -25.933 | 0.068 | 11011 | 0.353 |

Second, the relative error of the mean, variance, and covariance remain almost constant as the propagation time is increased. This does not imply, however, that the pdf remains consistent for all time even for low order STTs, as is demonstrated in Section 2.4.1.1. Consider first the mean. From Eqs. (2.17) and (2.39), the state deviation $\delta\tilde{\mathfrak{l}}$ in the $\mathfrak{l}$-direction at time $t$ found from STTs can be written as

$$\delta\tilde{\mathfrak{l}}(t) = (\Phi_{\mathfrak{l},\mathfrak{Q}}\delta\mathfrak{Q}^0 + \Phi_{\mathfrak{l},\mathfrak{l}}\delta\mathfrak{l}^0) + \frac{1}{2}\Phi_{\mathfrak{l},\mathfrak{Q}\mathfrak{Q}}(\delta\mathfrak{Q}^0)^2 + \dots \tag{2.85}$$

$$= \delta\mathfrak{l}^0 - 3(\mathfrak{Q}^0)^{-4}\mu^2\Delta t\,(\delta\mathfrak{Q}^0) + 6(\mathfrak{Q}^0)^{-5}\mu^2\Delta t\,(\delta\mathfrak{Q}^0)^2 + \dots, \tag{2.86}$$

where $\delta\mathfrak{Q}^0$ and $\delta\mathfrak{l}^0$ are the initial state deviations. Factoring out all of the terms with $\Delta t$,

$$\delta\tilde{\mathfrak{l}}(t) = \delta\mathfrak{l}^0 + \delta\hat{\mathfrak{l}}\Delta t. \tag{2.87}$$

$\delta\hat{\mathfrak{l}}$ is constant in time. Next, from the complete two-body dynamics, the deviation $\delta\mathfrak{l}$ is

$$\delta\mathfrak{l}(t) = \delta\mathfrak{l}^0 + \mu^2\left\{(\mathfrak{Q}^0)^{-3} - (\mathfrak{Q}^0_*)^{-3}\right\}\Delta t, \tag{2.88}$$

where the asterisk denotes the reference orbit. Therefore, the absolute error between the mean calculated using MC runs and using STTs is

$$E[\delta\mathfrak{l}(t)] - E[\delta\tilde{\mathfrak{l}}(t)] = E[\delta\mathfrak{l}(t) - \delta\tilde{\mathfrak{l}}(t)] = E\left[\mu^2\left\{(\mathfrak{Q}^0)^{-3} - (\mathfrak{Q}^0_*)^{-3}\right\} - \delta\hat{\mathfrak{l}}\right]\Delta t, \tag{2.89}$$

which grows proportionally with propagation time. The relative error is then

$$\frac{E[\delta\mathfrak{l}(t)] - E[\delta\tilde{\mathfrak{l}}(t)]}{E[\delta\mathfrak{l}(t)]} = \frac{E\left[\mu^2\left\{(\mathfrak{Q}^0)^{-3} - (\mathfrak{Q}^0_*)^{-3}\right\} - \delta\hat{\mathfrak{l}}\right]\Delta t}{E\left[\delta\mathfrak{l}^0 + \mu^2\left\{(\mathfrak{Q}^0)^{-3} - (\mathfrak{Q}^0_*)^{-3}\right\}\Delta t\right]}. \tag{2.90}$$

But initially zero mean so $E[\delta\mathfrak{l}^0] = 0$, and denoting $S \equiv \mu^2\{(\mathfrak{L}^0)^{-3} - (\mathfrak{L}_*^0)^{-3}\}$ constant in time,

$$\frac{E[\delta\mathfrak{l}(t)] - E[\delta\tilde{\mathfrak{l}}(t)]}{E[\delta\mathfrak{l}(t)]} = \frac{\left(E[S] - E[\delta\hat{\mathfrak{l}}]\right)\Delta t}{E[\delta\mathfrak{l}^0] + E[S]\Delta t} = 1 - \frac{E[\delta\hat{\mathfrak{l}}]}{E[S]}, \tag{2.91}$$

which does not depend on propagation time, as the results indicate. $E[\delta\hat{\mathfrak{l}}]$ and $E[S]$ can both be determined *a priori*; thus, it is possible to estimate the amount of relative error the mean of a pdf will incur at an arbitrary order of the dynamics simply given the initial reference state and information regarding the initial probability distribution.

Next, for the variance $\sigma_{\mathfrak{l}}^2$,

$$\sigma_{\mathfrak{l}}^2 = E[(\delta\mathfrak{l} - \delta\bar{\mathfrak{l}})^2] = E[\delta\mathfrak{l}^2] - \delta\bar{\mathfrak{l}}^2, \tag{2.92}$$

where bar indicates mean. Now, for the complete two-body dynamics,

$$E[\delta\mathfrak{l}^2] = (\delta\mathfrak{l}^0)^2 - \frac{2\,\delta\mathfrak{l}^0\,\mu^2}{(\mathfrak{L}_*^0)^3}\Delta t + \frac{\mu^4}{(\mathfrak{L}_*^0)^6}\Delta t^2 + 2\,\delta\mathfrak{l}^0\,\mu^2\,E[(\mathfrak{L}^0)^{-3}]\Delta t - \frac{2\mu^4}{(\mathfrak{L}_*^0)^3}E[(\mathfrak{L}^0)^{-3}]\Delta t^2 + \mu^4\,E[(\mathfrak{L}^0)^{-6}]\Delta t^2 \tag{2.93}$$

$$\delta\bar{\mathfrak{l}}^2 = (\delta\mathfrak{l}^0)^2 - \frac{2\,\delta\mathfrak{l}^0\,\mu^2}{(\mathfrak{L}_*^0)^3}\Delta t + \frac{\mu^4}{(\mathfrak{L}_*^0)^6}\Delta t^2 + 2\,\delta\mathfrak{l}^0\,\mu^2\,E[(\mathfrak{L}^0)^{-3}]\Delta t - \frac{2\mu^4}{(\mathfrak{L}_*^0)^3}E[(\mathfrak{L}^0)^{-3}]\Delta t^2 + \mu^4\left(E[(\mathfrak{L}^0)^{-3}]\right)^2\Delta t^2 \tag{2.94}$$

Therefore,

$$\sigma_{\mathfrak{l}}^2 = \mu^4\left\{E[(\mathfrak{L}^0)^{-6}] - \left(E[(\mathfrak{L}^0)^{-3}]\right)\right\}\Delta t^2 \equiv \mu^4\,E[K]\Delta t^2 \tag{2.95}$$

Next, for the approximate dynamics from the STTs,

$$E[\delta\tilde{\mathfrak{l}}^2] = (\delta\mathfrak{l}^0)^2 + 2\,\delta\mathfrak{l}^0\,E[\delta\hat{\mathfrak{l}}]\Delta t + E[\delta\hat{\mathfrak{l}}^2]\Delta t^2 \tag{2.96}$$

$$\left(E[\delta\tilde{\mathfrak{l}}]\right)^2 = (\delta\mathfrak{l}^0)^2 + 2\,\delta\mathfrak{l}^0\,E[\delta\hat{\mathfrak{l}}]\Delta t + \left(E[\delta\hat{\mathfrak{l}}]\right)^2\Delta t^2 \tag{2.97}$$

Thus,

$$\tilde{\sigma}_{\mathfrak{l}}^2 = \left\{E[\delta\hat{\mathfrak{l}}^2] - \left(E[\delta\hat{\mathfrak{l}}]\right)^2\right\}\Delta t^2 \equiv E[\hat{K}]\Delta t^2 \tag{2.98}$$

The relative error is

$$\frac{\sigma_{\mathfrak{l}}^2 - \tilde{\sigma}_{\mathfrak{l}}^2}{\sigma_{\mathfrak{l}}^2} = 1 - \frac{E[\hat{K}]}{\mu^4\,E[K]}, \tag{2.99}$$

which, again, is independent of the propagation time.

Finally, for the covariance $\mu_{\mathfrak{l}\mathfrak{L}}$

$$\mu_{\mathfrak{l}\mathfrak{L}} = E\left[(\delta\mathfrak{l} - \delta\bar{\mathfrak{l}})(\delta\mathfrak{L} - \delta\bar{\mathfrak{L}})\right] = E[\delta\mathfrak{l}\,\delta\mathfrak{L}] - \delta\bar{\mathfrak{l}}\,\delta\bar{\mathfrak{L}} \tag{2.100}$$

$$\tilde{\mu}_{\mathfrak{l}\mathfrak{L}} = E\left[(\delta\tilde{\mathfrak{l}} - E[\delta\tilde{\mathfrak{l}}])(\delta\mathfrak{L} - \delta\bar{\mathfrak{L}})\right] = E[\delta\tilde{\mathfrak{l}}\,\delta\mathfrak{L}] - E[\delta\tilde{\mathfrak{l}}]\,\delta\bar{\mathfrak{L}} \tag{2.101}$$

But $\delta\mathfrak{Q} = \delta\mathfrak{Q}^0$, so $E[\delta\mathfrak{l}\,\delta\mathfrak{Q}] = E[\delta\mathfrak{l}\,\delta\mathfrak{Q}^0]$ and $\delta\bar{\mathfrak{Q}} = \delta\bar{\mathfrak{Q}}^0 = 0$ from the zero initial mean assumption. Next, from Eq. (2.87) and (2.88),

$$E[\delta\mathfrak{l}\,\delta\mathfrak{Q}^0] = E[\delta\mathfrak{Q}^0(\delta\mathfrak{l}^0 + S\,\Delta t)] = E[\delta\mathfrak{Q}^0\,\delta\mathfrak{l}^0] + E[\delta\mathfrak{Q}^0\,S\,]\Delta t \tag{2.102}$$

$$E[\delta\tilde{\mathfrak{l}}\,\delta\mathfrak{Q}^0] = E[\delta\mathfrak{Q}^0(\delta\mathfrak{l}^0 + \delta\hat{\mathfrak{l}}\Delta t)] = E[\delta\mathfrak{Q}^0\,\delta\mathfrak{l}^0] + E[\delta\mathfrak{Q}^0\,\delta\hat{\mathfrak{l}}]\Delta t, \tag{2.103}$$

where both $E[\delta\mathfrak{Q}^0\,\delta\hat{\mathfrak{l}}]$ and $E[\delta\mathfrak{Q}^0\,S\,]$ are constants in time. In addition, recall that for this particular example, the initial covariance is 0 (i.e., off-diagonals of the covariance matrix are 0), so $E[\delta\mathfrak{Q}^0\,\delta\mathfrak{l}^0] = 0$. As a consequence, the relative error is

$$\frac{\mu_{\mathfrak{l}\mathfrak{Q}} - \tilde{\mu}_{\mathfrak{l}\mathfrak{Q}}}{\mu_{\mathfrak{l}\mathfrak{Q}}} = 1 - \frac{E[\delta\mathfrak{Q}^0\,\delta\hat{\mathfrak{l}}]}{E[\delta\mathfrak{Q}^0\,S\,]}, \tag{2.104}$$

which is independent of the propagation time.

#### 2.4.2.2 Two-Body Dynamics + Atmospheric Drag in a Circular Orbit

In this section, the initial uncertainty is assumed to be Gaussian as in Eq. (2.82) but only in the semi-major axis ($a$) and mean anomaly ($M$) directions; the ballistic coefficient is assumed to be constant at BC = $10^2$ kg/m$^2$. The central body is again approximated as a point mass.

The mean and covariance are computed using both a numerical MC simulation and the analytical dynamics via the STT method. In the MC simulation, the initial distribution is sampled at $10^4$ sample points that span across $\pm 6\sigma$ in both $a$ and $M$. The moments of the pdf along with the Jacobian determinant are numerically integrated with Eqs. (2.24), (2.25), and (2.28). These results are regarded as the truth. Conversely, in the STT propagation, since the contraction of the state space is slow for objects with realistic parameters such as in Eq. (2.48), it is assumed that $|\partial\mathbf{X}/\partial\mathbf{X}_0| \approx 1$ and thus the mean and covariance are computed with Eqs. (2.30) and (2.31), respectively. The dynamics are expanded up to 4th order, with the mean motion $n$ expanded up to first order. All computation is analytic.

The same two epochs are tested (*Calm* and *Stormy*) and the uncertainty is propagated for 1.257 days; a shorter propagation time is chosen only to ensure that the Monte Carlo converges in a reasonable time. Table 2.4 shows the relative error of the STT propagated cumulants with respect to the MC simulation. Overall, the analytically propagated cumulants are within 1% relative error for all coordinate directions. The accuracy

of the analytical covariance is consistently worse than the mean by an order of magnitude. A possible explanation is that the covariance can be thought of as a direct measure of the "volume" of the uncertainty, and thus is more strongly influenced by the phase volume contraction than the mean. Nevertheless, it may be concluded that approximating the phase volume as constant when computing for pdf cumulants analytically is acceptable for many low area-to-mass ratio objects in LEO.

Table 2.4: Relative error of analytically propagated cumulants compared to a numerically computed truth under two-body dynamics plus atmospheric drag.

| | **Rel. Err. Mean [%]** | | **Rel. Err. Cov. [%]** | | |
|---|---|---|---|---|---|
| **Scenario** | $\bar{a}$ | $\bar{M}$ | $\sigma_a^2$ | $\mu_{aM}$ | $\sigma_M^2$ |
| Calm | 0.0127 | -0.0145 | -0.5417 | -0.1815 | -0.3042 |
| Stormy | 0.0004 | -0.0220 | -0.7657 | -0.5939 | -0.4225 |

Finally, Table 2.5 compares computation time of cumulants between the MC and STT methods on a quad-core Xeon workstation with double floating point precision for the above example. Again, since the STTs are purely analytic, once the STTs have been solved for, all that is required for propagation is to change the time parameter accordingly. As a result, the STT propagation is not only many orders of magnitude faster than the Monte Carlo but also does not scale with propagation time (assuming constant expansion order) nor sampling resolution of the state space. Overall, these results indicate that the STT method is both accurate and efficient in non-linearly propagating uncertainty even in the presence of non-conservative forces.

Table 2.5: Computation time required to compute the mean and covariance with the Monte Carlo (MC) and state transition tensor (STT) techniques under two-body dynamics plus atmospheric drag. The process is split up into uncertainty propagation (Prop.), and mean (Mean) and covariance computation (Cov.) The results are an average over 10 simulation runs.

| | **MC** | **STT** |
|---|---|---|
| Prop. [s] | $2.370 \times 10^4$ | $7.033 \times 10^{-3}$ |
| Mean [s] | $1.763 \times 10^0$ | $1.328 \times 10^{-4}$ |
| Cov. [s] | $1.531 \times 10^0$ | $1.682 \times 10^{-4}$ |
| **Total [s]** | $2.370 \times 10^4$ | $7.334 \times 10^{-3}$ |

### 2.4.3 Conservation of the Prediction Error

Here, a comparison is conducted of how well the uncertainty consistency metric Eq. (2.14) is conserved when **(a)** the proposed approach of propagating the pdfs with the solution to the Fokker-Planck Eq. (2.10) for deterministic Hamiltonian systems is implemented, and when **(b)** the classical approach of propagating only the first two cumulants linearly along a reference trajectory with the state transition matrix Eq. (2.13) is implemented. Recall from Section 2.1.1 that the more $\mathcal{PE}(t)$ changes with propagation time, the less accurate the representation of the uncertainty becomes. Of the two truth orbits to be considered, the initial state of the first (Object 1) is Eq. (2.72), and the second (Object 2) is given as

$$a = 1.10064, e = i = \Omega = \omega = M = 0 \Rightarrow \mathfrak{L} = 4.6812, \mathfrak{l} = \mathfrak{G} = \mathfrak{g} = \mathfrak{H} = \mathfrak{h} = 0. \tag{2.105}$$

Initial pdfs $p_1(\mathbf{X}^0)$ and $p_2(\mathbf{X}^0)$ are defined corresponding to Object 1 and 2, respectively, to have zero mean about each reference orbit and a covariance Eq. (2.74), or case (ii) in Section 2.4.1.1. Only two-body dynamics are considered for this example.

To compute $\mathcal{PE}(t)$

**(a) Fokker-Planck** (1) Propagate initial pdfs with forward flow $\boldsymbol{\phi}(t; \mathbf{X}^0, t^0)$.

(2) Sample pdfs and propagate each point back to time $t^0$ with either the complete inverse flow $\boldsymbol{\psi}(t, \mathbf{X}; t^0)$ or its corresponding STT $\Psi$.

(3) Evaluate the pdf at each $\mathbf{X}^0$ and assign this value to $\mathbf{X}$.

(4) Integrate $p_1 p_2$ over state space $\mathbf{X}$ with a quadrature.

**(b) Linear** (1) Propagate the mean and covariance matrices of the initial pdfs with the STM.

(2) Sample pdfs and evaluate them at each sample point.

(3) Integrate $p_1 p_2$ over state space $\mathbf{X}$ with a quadrature.

Figure 2.16 shows the evolution of $\mathcal{PE}(t)$ over 20 orbit periods of Object 1, and Table 2.6 is a summary of $\mathcal{PE}(t)$ after 20 orbit periods. As expected, $\mathcal{PE}(t)$ is best conserved for method (a) with complete inverse dynamics, followed by that with the higher order STT dynamics. The solution from method (a) with first

order STTs and those from method (b) are equivalent and their uncertainty consistency is considerably worse than all of the other methods. These results quantify the robustness of the proposed method of uncertainty propagation that was mentioned in Section 2.4.1.1.

Table 2.6: Change in $\mathcal{PE}$ after 20 orbit periods of Object 1 under two-body dynamics. "F-P" indicates propagation via the Fokker-Planck solution, and the number after "STT" indicates the order of the expansion of the dynamics.

| | Linear | F-P (STT:1) | F-P (STT:2) | F-P (STT:3) | F-P (STT:4) | F-P (Complete) |
|---|---|---|---|---|---|---|
| $\Delta\mathcal{PE}$ | 23725.31 | 23725.31 | 116.8219 | 0.003063 | $8.71507 \times 10^{-5}$ | $3.82374 \times 10^{-6}$ |

Again, linear propagation of uncertainty becomes inconsistent with the actual probability distribution even after a couple of orbits. Furthermore, the performance improvement diminishes for propagation via the Fokker-Planck solution as the order of the inverse STT dynamics is increased. These results suggest that second order dynamics may provide sufficient uncertainty consistency for many applications. For the two-body problem, the MATLAB implementation is able to generate both first- and second order STTs in less than a second on a dual-core Core 2 Duo laptop with double floating point precision. Even for more complex dynamical systems that do not have analytical solution flows, $6^2 + 6^3 = 252$ ODEs in Eq. (2.20) need to be solved to generate STTs up to second order. The proposed method has the potential of consistently propagating pdfs with less computational burden than existing techniques. For example, an Edgeworth filter attaining the same level of accuracy as the second order STT requires the evaluation of 2021 sigma points [33]. Furthermore, unlike a MC analysis where the dynamics must be integrated for every sample point of every epoch, the STT needs to be integrated only once per epoch [47, 56].

## 2.5 Conclusions

In this chapter, an analytical method of non-linear uncertainty propagation including non-conservative effects was discussed. A special solution to the Fokker-Planck equations for deterministic systems and the state transition tensor concept are combined so that, given an analytical expression of both the initial probability distribution and the dynamics, the probability distribution may be expressed analytically for all time.

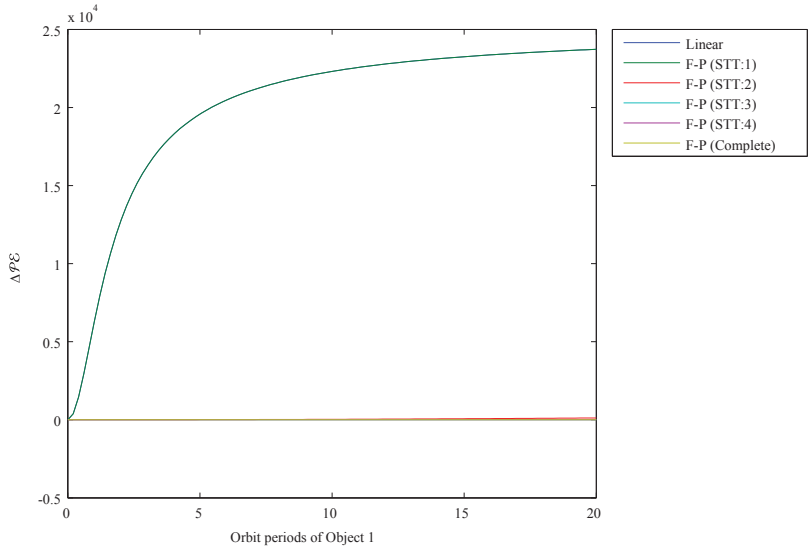


Figure 2.16: The change in $\mathcal{PE}(t)$ over time using various propagation methods under two-body dynamics. "F-P" indicates propagation via the Fokker-Planck solution, and the number after "STT" indicates the order of the expansion of the dynamics. The Linear and F-P (STT:1) curves, and the F-P (STT:2) through F-P (Complete) curves are nearly identical, respectively.

Propagation of uncertainty is then only a matter of changing the time parameter $t$. In particular, two-body dynamics, two-body dynamics plus secular effects of the oblateness of the Earth, and King-Hele's theory on orbital motion influenced by atmospheric drag are applied to the above framework. The propagation results are compared with a numerical Monte Carlo simulation. This example demonstrated the potential efficiency and accuracy of analytical uncertainty propagation even when compared to numerical results employing realistic parameter models.

Future work of this research is to further incorporate additional perturbations relevant to Earth-orbiting objects, such as the full effects due to the oblateness of the Earth. Including secular variations alone is not enough, especially when the effects of atmospheric drag are modeled, as the short period oscillations in the semi-major axis as well as resonance due to tesseral harmonics greatly influence the drag force exerted on the object. Therefore, more sophisticated solutions to the dynamics are required [9, 31, 32, 73]. As a preliminary step, the propagated 3-$\sigma$ ellipsoid for a circular orbit using the semi-empirical method by Parks is shown in Figure 2.17 [58]. Although Parks' method does not produce probabilistic moments, the continued good agreement between the analytic and Monte Carlo results suggests that further investigation in analytic uncertainty propagation may indeed be fruitful.

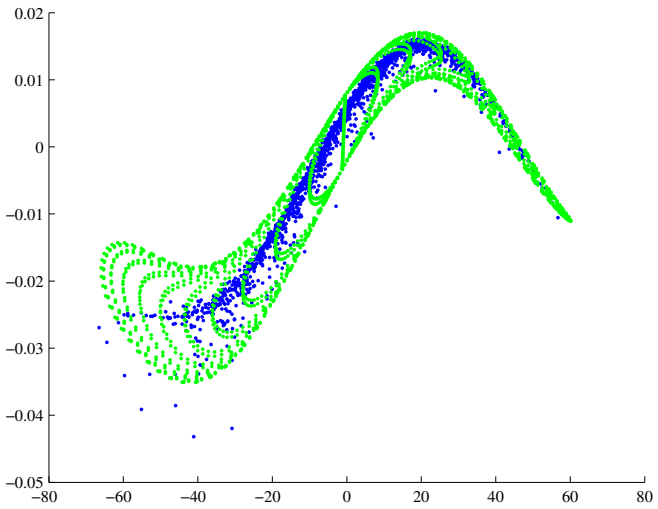


Figure 2.17: An initial Gaussian distribution propagated numerically (blue) and analytically (green) over 1.2572 days for the *Storm* scenario in a circular orbit with $J_2$ effects included. The result is projected on the semi-major axis ($a$) / mean anomaly ($M$) space in units of km-rad and subsequently rotated so that the axes of the plot correspond to the principal axis directions of the linearly propagated ellipse.

# Chapter 3

## Association of Short-Arc Optical Observations via The Direct Bayesian Admissible Region Method

Consistent characterization of the uncertainty associated with resident space objects (RSOs) such as active satellites and space debris is crucial in maintaining an accurate catalog of objects in Earth orbit. For instance, the geometry of observational uncertainty is significantly influenced by the type of observation made. In this chapter, we present an *a priori* state-free direct Bayesian approach to observation association and initial orbit determination that takes into account both the highly directional spread of uncertainty for optical observations and the deterministic nature of the dynamical environment. Optical observations are expressed as probability density functions (pdfs) called *admissible regions* (AR) that predominantly span in the undetermined but physically constrained range and range-rate directions. A small "thickness" may also be added in the remaining 4 dimensions of the state space corresponding to the errors in angle and angle-rates. These pdfs, along with any other pdfs associated with tracked objects or uncorrelated tracks (UCTs), are propagated analytically and non-linearly via a special solution to the diffusionless Fokker-Planck equation discussed in Chapter 2 and combined via Bayes' rule.

The outline of this chapter is as follows. The too-short arc problem for Earth-orbiters is defined and the AR concept is introduced in this context. The sparseness of ARs is discussed by applying the Theory of General Position in topology. Next, the AR is rigorously generalized to be a pdf, which allows one to rationally associate observations. Methods of efficiently computing these generalized ARs via linearization and linear extrapolation are shown and demonstrated. Limiting cases of the direct Bayesian approach exist, namely, processing simultaneous observations as well as observations from a satellite constellation. Finally,

simulated implementations are given for both ground- and space-based observations. In both cases, the algorithm succeeds in associating $\sim 10^2$ observations in various orbits taken from the public two-line element catalog. Recommendations on orbits for a space-based sensor in the geosynchronous region are made based on the association results.

## 3.1 The Too-Short Arc Problem

Regardless of where the observation is made, from the ground or from space, for optical-only observations of Earth-orbiting objects, the measured state variables are the object's angles plus their time stamps; that is, per observation, the range and range-rate remain largely unconstrained. Consequently, orbit determination has traditionally been conducted with some type of batch or sequential estimation algorithm, whose reference state is supplied via geometric techniques known as initial orbit determination (IOD) [79, 83]. Here, the association of observations must be assumed initially and then deduced from the quality of the least-squares fit; that is, the association of observations is a direct function of the quality of the orbit estimation and vice versa. This approach becomes problematic especially in a survey-type observation strategy. Usually, only a limited number of observations are available per night per object, each over short observation arcs, or *tracklets*, that span a few minutes [46]. Given such a small window of data, a large subset of the state space remains consistent with each tracklet, leading to poor convergence to the true solution if not divergence. The association of observations, therefore, cannot be inferred confidently. Figure 3.1 shows the time history of the residuals in the angular variables when fitting two tracklets of a geosynchronous (GEO) satellite to its true state (Object 1) as well as a fictitious state (Object 2) separated by at least 270 km but still consistent with the observations. Table 3.1 shows the RMS of the residuals. Each tracklet spans 2 minutes and consists of 5 observations; the two tracklets are separated by 20 minutes. A 2 arcsec 1-$\sigma$ Gaussian noise is added to the observed angles. The Kelperian orbit elements ($a$ [km], $e$, $i$ [deg], $\Omega$ [deg], $\omega$ [deg], $M$ [deg]) for each object at the simulation epoch is as follows:

**Object 1** $(42164.154, 10^{-6}, 0.1, 0, 0, 0)$

**Object 2** $(41079.037, 0.01965, 0.1060, -18.29, -161.8, -179.9)$.

We find that, in this situation, the residuals give us no indication which state is more likely.

Table 3.1: The root mean square of the residuals in right ascension ($\delta$RA) and declination ($\delta$DEC) for a simulated observation of a GEO object when fit to its truth state (Object 1) and a consistent but false state (Object 2).

| | **Object 1** | **Object 2** |
|---|---|---|
| $\delta$RA [arcsec] | 1.83405 | 1.72122 |
| $\delta$DEC [arcsec] | 2.37513 | 2.86219 |

Furthermore, in order to derive tractable geometric relationships between line-of-sight vectors, a simplistic dynamical model must be incorporated in the IOD. For example, the orbit may be assumed to be circular, or the Earth's gravity field may be considered as a point mass [17]. The former fails to incorporate eccentric orbits such as those in a geostationary transfer orbit (GTO) or high area-to-mass ratio (HAMR) objects [63]. The latter, although valid for celestial bodies that are predominantly influenced by gravity, is less effective for RSOs which experience many perturbing forces including atmospheric drag, irregularities of the central body, and solar radiation pressure, just to name a few.

These difficulties in the association of optical observations of RSOs as well as the subsequent orbit determination are referred to as the *too-short arc* (TSA) problem [82]. A similar problem, albeit in longer time scales, has been studied for heliocentric orbits; in fact, the original idea of the admissible region was devised for the astrometry of celestial bodies [50, 51]. The more general problem of multiple target tracking using bearing-only sensors continues to be tackled in the filtering community, but most solutions require a reference state, a Gaussian assumption on the error distribution, or great computational power [23, 62].

## 3.2 The Attributable Vector

Each optical tracklet can be mathematically expressed in terms of an *attributable vector* $\mathcal{A}$ at epoch $t^0$ of the observation [82]

$$\mathcal{A} = (\alpha^0, \delta^0, \dot{\alpha}^0, \dot{\delta})^0 \in [-\pi, \pi) \times (-\pi/2, \pi/2) \times \mathbb{R}^2, \tag{3.1}$$

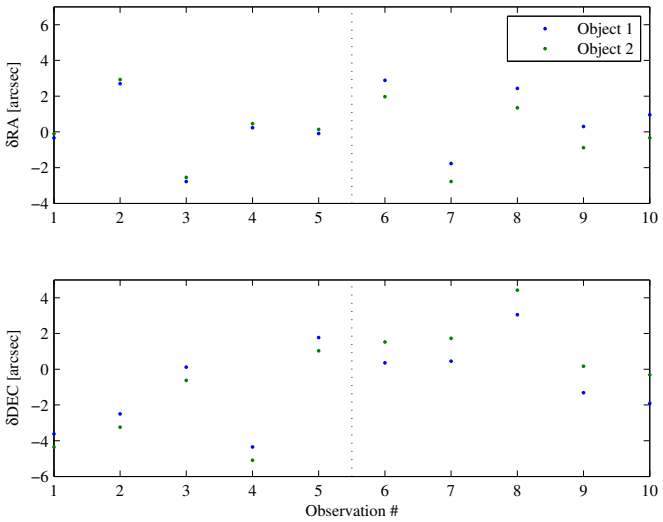


Figure 3.1: History of residuals in right ascension ($\delta$RA) and declination ($\delta$DEC) for a simulated observation of a geostationary orbit object fit to its true state (Object 1) and a consistent but false state (Object 2).

where $\alpha$ and $\delta$ specify the topocentric angular position of the object. Nominally, J2000 is chosen as the coordinate system so that $\alpha$ is the right ascension and $\delta$ is the declination. To estimate the angle rates at the tracklet epoch from a given track of data, the measured angles are fit to a polynomial kinematic model in time, such as for the right ascension

$$\alpha(t) = \alpha^0 + \dot{\alpha}^0(t - t_0) + \frac{1}{2}\ddot{\alpha}^0(t - t_0)^2, \tag{3.2}$$

where subscript 0 denotes the state at epoch [46]. A more detailed discussion on the attributable vector including error bounds is in Maruskin et al [46]. In addition, information regarding time and the location of the observer should be stored for a more complete description of the track, leading to an extended set $\mathfrak{Y}$

$$\mathfrak{Y} = (\mathcal{A}, t^0, h, \phi, \Theta), \tag{3.3}$$

where $h$ is the altitude of location of observation, and $\Theta$ and $\phi$ are the angular position of the observatory in a geocentric spherical coordinate system. The coordinate system is such that $\Theta$ is the latitude and $\phi$ is the longitude of the observation point. In the following discussion, $h$ is ignored for simplicity; it is justified since $h$ is often much less than a percent of the position vector norm of the object.

When the observation is made from a space-based sensor, the observed object and the observer follow the same equations of motion, whereas for ground-based observations, the dynamics of the observer are solely determined by the Earth's rotation. Therefore, for a more general description of the track, the geocentric position $\mathbf{P}_O$ and velocity $\dot{\mathbf{P}}_O$ of the observation point can be appended in addition to the epoch time $t^0$

$$\mathfrak{Y} = (\mathcal{A}, t^0, \mathbf{P}_O, \dot{\mathbf{P}}_O). \tag{3.4}$$

In this chapter, perfect knowledge regarding the state of the observing satellite is assumed. This assumption allows us to use the same formulation of the attributable vector between ground-based and space-based observations except for the dynamics of the observation point. Qualitatively, this assumption is expected to be good especially when the observer is in a low Earth orbit (LEO) orbit because the errors in the observer's state ($10^1$ meter-level in position, $10^0$ millimeter/second-level in velocity [83, 87]) is much less than the uncertainty in range / range-rate.

## 3.3 The Classical Admissible Region

For some attributable vector $\mathfrak{Y}$, one can take different values of range and range-rate $(\rho, \dot{\rho})$ to complete the topocentric coordinates of the object and thus obtain different physical orbits. Visually, one can imagine taking different points in the topocentric range / range-rate plane. However, not all of these orbits are relevant for any given application. Rather, a closed region of the $(\rho, \dot{\rho})$ plane can be defined such that all of the physically relevant orbits are contained within the interior of this region. This region is defined as the *classical admissible region* (AR), and each discretized point on the AR as a *Virtual Object* (VO). A set of criteria $C$ defining the classical AR has been proposed by Tommei et al, and later refined by Maruskin et al. [46, 82]

$$C = \bigcap_{i=1}^{4} C_i, \tag{3.5}$$

and

$$C_1 = \{(\rho, \dot{\rho}) : E \leq 0\} \qquad C_2 = \{(\rho, \dot{\rho}) : \rho_{\text{MIN}} \leq \rho \leq \rho_{\text{MAX}}\} \tag{3.6}$$

$$C_3 = \{(\rho, \dot{\rho}) : 1.03 \leq r_p\} \qquad C_4 = \{(\rho, \dot{\rho}) : r_a \leq 25\}, \tag{3.7}$$

where $E$ is the specific geocentric energy of the object, $\rho_{\text{MIN}}$ and $\rho_{\text{MAX}}$ are bounds for the physical range of the object chosen *a priori*, and $r_a$ and $r_p$ are the apoapsis and periapsis radii of the orbit in units of Earth radii, respectively. For the ground-based observations simulated in this chapter, $(\rho_{\text{MIN}}, \rho_{\text{MAX}}) = (0.3, 20)$ Earth radii so as to include all objects observable by optical sensors but outside of the range of radar sensors, corresponding to an altitude of 2000 kilometers (0.3 Earth radii) to 130,000 kilometers (20 Earth radii) [19]. Similarly for space-based observations, $(\rho_{\text{MIN}}, \rho_{\text{MAX}}) = (0, 14)$ Earth radii from the observation geometry. Note that any of these criteria are flexible, and in some cases, not necessary. For example, if the observer is only interested in surveying objects in and near the GEO belt, $C$ may be modified to

$$C_1 = \{(\rho, \dot{\rho}) : E \leq 0\} \qquad C_2 = \{(\rho, \dot{\rho}) : 5 \leq \rho \leq 8, -1 \leq \dot{\rho} \leq 1\} \tag{3.8}$$

$$C_3 = \{(\rho, \dot{\rho}) : 5 \leq r_p\} \qquad C_4 = \{(\rho, \dot{\rho}) : r_a \leq 8\}. \tag{3.9}$$

Figure 3.2 and 3.3 are examples of classical ARs.

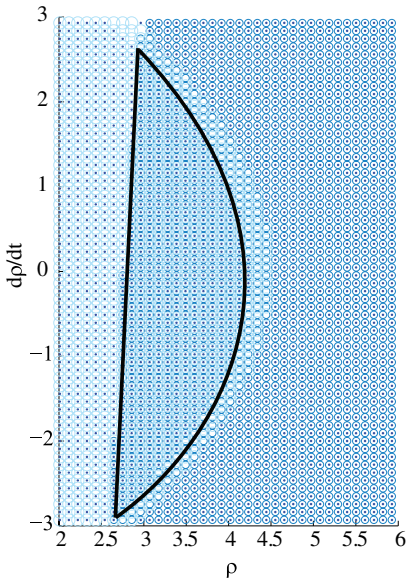


Figure 3.2: A classical admissible region for a simulated ground-based observation, where $\mathcal{A}$ = ($\alpha$, $\delta$, $\dot{\alpha}$, $\dot{\delta}$) = (118.258 deg, -13.625 deg, 29.060 arcsec/sec, 3.747 arcsec/sec). The inertial longitude $\Theta$ and latitude $\Phi$ of the observatory are ($\Theta$, $\Phi$) = (275.0 deg, 5.7 deg). The different shadings represent the different regions which satisfy each criterion in set $C$ ($C_1$: light circle, $C_2$: satisfied for the region plotted, $C_3$: dark circle, $C_4$: dark dot). The admissible region is where all types of shading overlap, or the region outlined by the black line. Unit of range are in Earth radii, range-rate in Earth radii / hour.

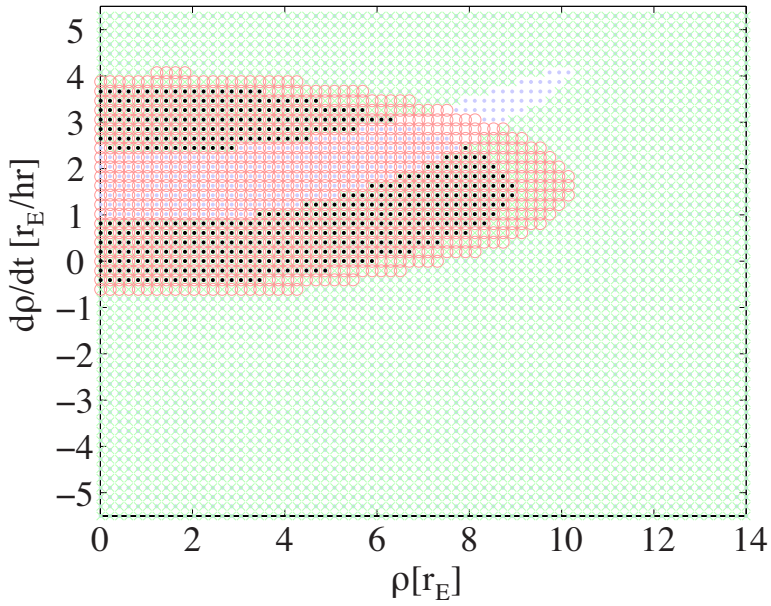


Figure 3.3: An admissible region for a simulated space-based observation, where $\mathcal{A} = (\alpha, \delta, \dot{\alpha}, \dot{\delta})$ = (53.09 deg, -18.74 deg, 12.17 arcsec/sec, 0.5872 arcsec/sec). The position $\mathbf{P}_O$ and velocity $\dot{\mathbf{P}}_O$ of the observer are (-37590.4, 17091.2, 7205.36) km and (-1.56206, -2.66918, -0.0225619) km/s, respectively. The different shadings represent the different regions which satisfy each criterion in set $C_1$ (circle), $C_3$ (cross), and $C_4$ (light dot). The admissible region is where all types of shading overlap, or the region indicated by the dark dots.

## 3.4 Transformation of Virtual Objects

Consider the transformation of VOs from topocentric spherical coordinates (i.e. $\alpha$,$\delta$,$\dot{\alpha}$,$\dot{\delta}$,$\rho$,$\dot{\rho}$) into Poincaré variables as defined with respect to the Keplerian orbital elements in Eq. (2.37). First, the exact, non-linear transformation is shown. Then, the procedure is linearized about an arbitrary reference point. The linearized results will be used later on to improve computational turnaround of the classical AR map. A similar discussion in terms of Delaunay orbital elements is given by Maruskin et al [46].

### 3.4.1 Exact Transformation

The exact transformation from topocentric spherical coordinates to Poincaré orbital elements is performed in several steps. First, from topocentric spherical coordinates to geocentric Cartesian coordinates

$$T_1 : \langle \rho, \dot{\rho}, \mathfrak{Y} \rangle \rightarrow \langle x, y, z, \dot{x}, \dot{y}, \dot{z} \rangle, \tag{3.10}$$

then to orbital elements [84]

$$T_2 : \langle x, y, z, \dot{x}, \dot{y}, \dot{z} \rangle \rightarrow \langle a, e, i, \Omega, \omega, M \rangle, \tag{3.11}$$

where $a$ is the semi-major axis, $e$ is the eccentricity, $i \in [0, \pi]$ is the inclination, $\Omega \in [-\pi, \pi]$ is the right ascension of the ascending node, $\omega \in [-\pi, \pi]$ is the argument of periapsis, and $M \in [-\pi, \pi]$ is the mean anomaly. Finally, the orbital elements are transformed to Poincaré variables

$$T_3 : \langle a, e, i, \Omega, \omega, M \rangle \rightarrow \langle \mathfrak{L}, \mathfrak{l}, \mathfrak{G}, \mathfrak{g}, \mathfrak{H}, \mathfrak{h} \rangle. \tag{3.12}$$

For a static problem (i.e. no time propagation,) a transformation $T_S$ from topocentric spherical coordinates to Poincaré variables is defined as

$$T_S = T_3 \circ T_2 \circ T_1. \tag{3.13}$$

The transformation to the time-evolved Poincaré space is described generally as

$$T_4(\tau, t^0) : \left\langle \mathfrak{L}(t^0), \mathfrak{l}(t^0), \mathfrak{G}(t^0), \mathfrak{g}(t^0), \mathfrak{H}(t^0), \mathfrak{h}(t^0) \right\rangle \rightarrow \langle \mathfrak{L}(\tau), \mathfrak{l}(\tau), \mathfrak{G}(\tau), \mathfrak{g}(\tau), \mathfrak{H}(\tau), \mathfrak{h}(\tau) \rangle, \tag{3.14}$$

where time is propagated from $t^0$ to $\tau$. Here, the results of $T_S$ which originate from observations at time $t^0$ are propagated to some other time $\tau$. For the unperturbed two-body case, we saw in Section 2.3.1 that the transformation simplifies to

$$T_{4,\text{two-body}}(\tau, t^0) : \left\langle \mathfrak{L}(t^0), \mathfrak{l}(t^0), \mathfrak{G}(t^0), \mathfrak{g}(t^0), \mathfrak{H}(t^0), \mathfrak{h}(t^0) \right\rangle \tag{3.15}$$

$$\rightarrow \left\langle \mathfrak{L}(t^0), \mathfrak{l}(t^0) + \frac{\mu^2}{\mathfrak{L}(t^0)^3}(\tau - t^0), \mathfrak{G}(t^0), \mathfrak{g}(t^0), \mathfrak{H}(t^0), \mathfrak{h}(t^0) \right\rangle, \tag{3.16}$$

where the only Poincaré variable that evolves over time is $\mathfrak{l}$. Note that the discussion in this chapter does not rely on a two-body approximation, and that it is used here solely as an example. It is possible to incorporate more detailed dynamical models into the method, such as those accounting for effects due to a non-spherical Earth, third-bodies, solar radiation pressure, atmospheric drag, and so on. The complete transformation from topocentric spherical coordinates to Poincaré variables including time evolution is written most generally as

$$T(\tau, t^0) = T_4(\tau, t^0) \circ T_S(t^0) \tag{3.17}$$

### 3.4.2 Linear Transformation

Given some reference point $(\rho^*, \dot{\rho}^*)$ and its exact transformation into Poincaré variables ($\mathfrak{l}^*$, $\mathfrak{L}^*$, $\mathfrak{g}^*$, $\mathfrak{G}^*$, $\mathfrak{h}^*$, $\mathfrak{H}^*$), one can linearize the transformation $T$ around this point. That is, define some $6 \times 2$ matrix $\Phi$ such that

$$(\delta\mathfrak{l}, \delta\mathfrak{L}, \delta\mathfrak{g}, \delta\mathfrak{G}, \delta\mathfrak{h}, \delta\mathfrak{H})^T = \Phi \begin{pmatrix} \delta\rho \\ \delta\dot{\rho} \end{pmatrix}, \tag{3.18}$$

where $\delta$ indicates a small deviation from the reference point.

The linear transformation is also constructed in steps. First, linearize $T_1$

$$\Phi_1 = \left.\frac{\partial(x, y, z, \dot{x}, \dot{y}, \dot{z})^T}{\partial(\rho, \dot{\rho})^T}\right|_* = \begin{bmatrix} \cos\alpha\cos\delta & 0 \\ \sin\alpha\cos\delta & 0 \\ \sin\delta & 0 \\ -\dot{\alpha}\sin\alpha\cos\delta - \dot{\delta}\cos\alpha\sin\delta & \cos\alpha\cos\delta \\ \dot{\alpha}\cos\alpha\cos\delta - \dot{\delta}\sin\alpha\sin\delta & \sin\alpha\cos\delta \\ \dot{\delta}\cos\delta & \sin\delta \end{bmatrix}_*, \tag{3.19}$$

where the $*$ indicates that the matrix is evaluated at the reference point. Similarly,

$$\Phi_2 = \left.\frac{\partial(a,e,i,\Omega,\omega,M)^T}{\partial(x,y,z,\dot{x},\dot{y},\dot{z})^T}\right|_* \tag{3.20}$$

$$\Phi_3 = \left.\frac{\partial(\mathfrak{L},\mathfrak{l},\mathfrak{G},\mathfrak{g},\mathfrak{H},\mathfrak{h})^T}{\partial(a,e,i,\Omega,\omega,M)^T}\right|_* . \tag{3.21}$$

An efficient method to find $\Phi_2$ is introduced in Montenbruck and Gill [52]. The linear counterpart to transformation $T_S$ is defined as

$$\Phi_S = \Phi_3 \cdot \Phi_2 \cdot \Phi_1 = \left.\frac{\partial(x,y,z,\dot{x},\dot{y},\dot{z})^T}{\partial(\rho,\dot{\rho})^T}\right|_* \cdot \left.\frac{\partial(a,e,i,\Omega,\omega,M)^T}{\partial(x,y,z,\dot{x},\dot{y},\dot{z})^T}\right|_* \cdot \left.\frac{\partial(\mathfrak{L},\mathfrak{l},\mathfrak{G},\mathfrak{g},\mathfrak{H},\mathfrak{h})^T}{\partial(a,e,i,\Omega,\omega,M)^T}\right|_* . \tag{3.22}$$

The linearization of $T_4$ is equivalent to the state transition matrix from time $t^0$ to $\tau$ for the Poincaré elements. Therefore, the general complete linear map from topocentric range / range-rate given some observation at time $t^0$ to Poincaré variables at time $\tau$ is

$$\Phi(\tau,t^0) = \Phi_4(\tau,t^0)\cdot\Phi_S(t^0). \tag{3.23}$$

Again, for unperturbed two-body dynamics, we may write $\Phi_4$ analytically as

$$\Phi_{4,\text{two-body}}(\tau,t^0) = \frac{\partial(\mathfrak{L}(\tau),\mathfrak{l}(\tau),\mathfrak{G}(\tau),\mathfrak{g}(\tau),\mathfrak{H}(\tau),\mathfrak{h}(\tau))^T}{\partial(\mathfrak{L}(t^0),\mathfrak{l}(t^0),\mathfrak{G}(t^0),\mathfrak{g}(t^0),\mathfrak{H}(t^0),\mathfrak{h}(t^0))^T} \tag{3.24}$$

$$= \begin{bmatrix} 1 & 0 & 0 & 0 & 0 & 0 \\ -3\mu^2(\tau-t^0)/\mathfrak{L}(t^0)^4 & 1 & 0 & 0 & 0 & 0 \\ 0 & 0 & 1 & 0 & 0 & 0 \\ 0 & 0 & 0 & 1 & 0 & 0 \\ 0 & 0 & 0 & 0 & 1 & 0 \\ 0 & 0 & 0 & 0 & 0 & 1 \end{bmatrix}, \tag{3.25}$$

as discussed in Section 2.3.1.

## 3.5 The Geometry of Classical Admissible Regions

Since the transformation from topocentric range / range-rate to Poincaré element space, as described in Section 3.4, is one-to-one and invertible, the map of the classical AR in the 6-dimensional Poincaré

space is a 2-dimensional bounded submanifold, or a disk [46]. Consequently, these submanifolds have co-dimension 4 relative to the phase space. Suppose there exist maps from two observations which have been dynamically evolved or regressed to a common epoch $\tau$. From the Theory of General Position, the dimension of intersection $d$ between a pair of disks of dimension $k$ and $l$ in $n$-dimensional space is given as

$$d = (k + l) - n, \tag{3.26}$$

where if $d < 0$, the two disks do not intersect generically [4]. For this problem, $d = (2 + 2) - 6 = -2$, so from the above argument, if two AR maps intersect at all, it is not a coincidental event. Therefore, we may conclude that it is extremely likely that the two observations of concern are related. The probability of two such distributions intersecting is similar to the probability of two points moving in a random direction in 3-dimensional space hitting each other: in this case, $d = (0 + 0) - 3 = -3 < 0$. In addition, Eq. (3.26) indicates that if one embeds these disks in 5-dimensional Poincaré space such as the ($\mathfrak{L}$, $\mathfrak{G}$, $\mathfrak{g}$, $\mathfrak{H}$, $\mathfrak{h}$) space, they will still not intersect generically. Similarly, for 4-dimensional Poincaré space they intersect at a point, for 3 dimensions a line, and for 2 dimensions an area.

## 3.6 Direct Bayesian Association of Observations

In this section, we generalize the classical AR concept by regarding ARs as probability density functions (pdfs) that describe any type of observation of arbitrary dimension. We then rigorously define the association of multiple observations via Bayes' rule: hence the name *direct Bayesian admissible region* method. The theory is applied back to optical observations of RSOs.

### 3.6.1 The Generalized Admissible Region

Let $\mathcal{X}$ be the $n$-dimensional state space and define an invertible transformation $\mathcal{F} : \mathcal{X} \mapsto \mathcal{Y}$ to some space $\mathcal{Y}$. Further, let $\bar{\mathcal{Y}}$ be a $m$ ($\leq n$) dimensional subset of $\mathcal{Y}$. An *attributable vector* $\mathfrak{Y}^{t^0} \equiv \mathfrak{Y}^0 \in \bar{\mathcal{Y}}$ is a vector containing all of the directly observed variables for a given observation at time $t^0$. Any variables in set $\mathcal{Y} \setminus \bar{\mathcal{Y}}$ are referred to as *unobserved*. Furthermore, suppose that, given some set of criteria $C$, $A$ is a compact set in $\mathcal{X}$ that meet $C$. Then, the *generalized admissible region* $F_C[\mathbf{X}(t^0); \mathfrak{Y}^0]$ is a pdf over $\mathcal{X}$ assigned to an

attributable vector $\mathfrak{Y}^0$ such that the probability $p$ that the observed object exists in region $B \subset A$ at time $t^0$ is

$$p[\mathbf{X}(t^0)] = \int_B F_C[\mathbf{X}(t^0); \mathfrak{Y}^0] \mathrm{d}X_1^0 \mathrm{d}X_2^0 \ldots \mathrm{d}X_n^0, \tag{3.27}$$

where $\mathbf{X}(t^0) \in \mathcal{X}$ and

$$\mathbf{X}(t^0) \equiv \mathbf{X}^0 = (X_1^0, X_2^0, \ldots, X_n^0). \tag{3.28}$$

Note that we impose $\int_A F_C[\mathbf{X}(t^0); \mathfrak{Y}^0] \mathrm{d}\mathbf{X}^0 = 1$. Also, the support of a generalized AR can be regarded to be mathematically equivalent as the classical AR, and thus is a compact $n-m$ dimensional manifold embedded in an $n$ dimensional space.

The generalized AR expresses our *limited* knowledge regarding the variables that are observed indirectly [13]. In conventional filtering, pdfs of the observations only describe the error in the attributable vector and are realized in the state space as likelihoods. For underdetermined systems, the integral of the likelihood function over the state space is divergent as we gain no information from the observations in coordinate directions corresponding to the variables indirectly observed. We realize, however, that knowledge in these directions is not completely *lacking* for many real-world systems as the likelihood function may suggest. That is, we may add physical constraints $C$ to the observed object's state such that we define a compact pdf $F$ that is still representative of all physically relevant states. Note that we refer to generalized ARs as simply "admissible regions" from here on unless a clear distinction must be made between them and classical ARs.

### 3.6.2 Association of Observations

By converting observation information into a pdf and propagating them to a common epoch, observations can be rationally combined with any other probabilistic data using Bayes' theorem, be it new observations or density information from the Joint Space Operations Center (JSpOC) two-line element (TLE) catalog, for example. An event $E_{O^1}(V^\tau)$ where some observation $O^1$ made at time $t^1$ is *consistent* with some region $V^\tau$ in state space at time $\tau$ if, given $P$ is a probability measure and $f[\mathbf{X}(t^1); O^1]$ is the pdf associated

with $O^1$,

$$P[E_{O^1}(V^\tau)] = \int_{V^\tau} \left\{\mathcal{T}(\tau, t^1) \circ f[\mathbf{X}(t^1); O^1]\right\} \mathrm{d}\mathbf{X}, \tag{3.29}$$

where $\mathcal{T}(\tau, t^1)$ is a transformation that maps $f$ from time $t^1$ to $\tau$ and $\mathbf{X} \equiv \mathbf{X}(\tau)$. Here, the term *observation* is used in the statistical sense: it is not limited to physical observations but rather apply to results from any kind of experiment or analysis. Generally, one must solve the Fokker-Planck equation to solve for $\mathcal{T}$; for deterministic systems, however, we saw in Section 2.1 that $\mathcal{T}$ is a function of the solution flow of the dynamics, and for Hamiltonian systems, they coincide. Thus the transformation $T(\tau, t^i)$ in Section 3.4 is applicable [56]. In addition, a generalized AR with a uniform distribution can be processed with the same methods and algorithms as a classical AR.

Let $E_{O^2=O^1}$ be an event where some observation $O^2$ made at time $t^2$ is of the same object as $O^1$. Then, if the pdf associated with $O^2$ is $g[\mathbf{X}(t^2); O^2]$,

$$P[E_{O^1}(V^\tau)|E_{O^2=O^1}] = \int_{V^\tau} h[\mathbf{X}(\tau)]\mathrm{d}\mathbf{X} \tag{3.30}$$

where

$$h[\mathbf{X}(\tau)] = \frac{\{\mathcal{T}(\tau, t^1) \circ f[\mathbf{X}(t^1); O^1]\}\{\mathcal{T}(\tau, t^2) \circ g[\mathbf{X}(t^2); O^2]\}}{\int\{\mathcal{T}(\tau, t^1) \circ f[\mathbf{X}(t^1); O^1]\}\{\mathcal{T}(\tau, t^2) \circ g[\mathbf{X}(t^2); O^2]\}\mathrm{d}\mathbf{X}}, \tag{3.31}$$

and operator "|" indicates conditional probability. The integral in Eq. (3.31) is over the entire state space. That is, given $E_{O^1}(V^\tau)$ true, for $E_{O^2=O^1}$ to also be true, we require $E_{O^2}(V^\tau)$ for any choice of $V^\tau$. Therefore,

$$P[E_{O^2=O^1}|E_{O^1}(V^\tau)] = P[E_{O^2}(V^\tau)] = \int_{V^\tau} \{\mathcal{T}(\tau, t^2) \circ g[\mathbf{X}(t^2); O^2]\}\mathrm{d}\mathbf{X}. \tag{3.32}$$

Then apply Bayes' theorem [61].

Now, for systems where the pdfs $f$ and $g$ are of high codimension, the sparseness of the problem allows for efficient ways to associate observations and simultaneously obtain a state estimate. For observations $O^1$ and $O^2$ such that

$$\dim\left\{f[\mathbf{X}(t^1); O^1]\right\} + \dim\left\{g[\mathbf{X}(t^2); O^2]\right\} < \dim(\mathbf{X}), \tag{3.33}$$

$P[E_{O^2=O^1}] = 0$ if for all $\mathbf{X}$,

$$\{\mathcal{T}(\tau, t^1) \circ f[\mathbf{X}(t^1); O^1]\}\{\mathcal{T}(\tau, t^2) \circ g[\mathbf{X}(t^2); O^2]\} = 0. \tag{3.34}$$

from the Theory of General Position Eq. (3.26). Therefore, for a set of observations that satisfy Eq. (3.33), their association does not have to be assumed as it is determined as a consequence of the combination process Eq. (3.30). We conclude that this method can be particularly robust to outlier observations.

Furthermore, as discussed in Section 3.7, if $f$ and $g$ have high codimension, we can employ linear extrapolation to rapidly discretize the pdfs and evaluate Eq. (3.30) numerically, limiting the consequences of the so called *curse of dimensionality*. Eq. (3.33) suggests that if the two pdfs are associated with the same object, then more and more constraints must be met locally for their intersection to have higher dimensions. The *a posteriori* pdfs, then, would most likely span a very small region in state space if not singularly defined at a point. Subsequent application of Eq. (3.33) becomes computationally trivial. Assuming that the support of $f$ and $g$ are manifolds, the pdfs are locally homeomorphic to $\mathbb{R}^{n-m}$, where $n$ is the dimension of the state space and $m$ is the dimension of the observable variable space. Then, we can describe points near some $\mathbf{X}^*$ on $f$ as follows

$$\mathbf{X} = \mathbf{X}^* + s_1\mathbf{v}_1 + s_2\mathbf{v}_2 + \cdots + s_{n-m}\mathbf{v}_{n-m}, \tag{3.35}$$

where $\{\mathbf{v}\}$ are some independent bases of $\mathbb{R}^{n-m}$, and $s_j \in \mathbb{R}$ for $j = 1, 2, \ldots, n-m$. Similarly on $g$ near some $\mathbf{Y}^*$,

$$\mathbf{Y} = \mathbf{Y}^* + t_1\mathbf{u}_1 + t_2\mathbf{u}_2 + \cdots + t_{n-m}\mathbf{u}_{n-m}. \tag{3.36}$$

Then, locally, the intersection of the manifolds is described as

$$\mathbf{X} = \mathbf{Y} \tag{3.37}$$

$$\Leftrightarrow \mathbf{z} = \mathrm{M}\,\mathbf{s}, \tag{3.38}$$

where

$$\mathrm{M} = \begin{bmatrix} & & & & & & \\ \mathbf{v}_1 & \mathbf{v}_2 & \cdots & \mathbf{v}_{n-m} & -\mathbf{u}_1 & \cdots & -\mathbf{u}_{n-m} \\ & & & & & & \end{bmatrix} \tag{3.39}$$

$$\mathbf{s} = \begin{bmatrix} s_1 & s_2 & \cdots & s_{n-m} & t_1 & \cdots & t_{n-m} \end{bmatrix}^T \tag{3.40}$$

$$\mathbf{z} = \mathbf{X}^* - \mathbf{Y}^*. \tag{3.41}$$

For $f$ and $g$ that satisfy Eq. (3.33), M cannot be inverted since M is not full rank. By taking the pseudoinverse we find

$$\tilde{\mathbf{s}} = (\mathrm{M}^T\mathrm{M})^{-1}\mathrm{M}^T\mathbf{z} \tag{3.42}$$

$$= \tilde{\mathrm{M}}\,\mathbf{z}. \tag{3.43}$$

For the two pdfs to intersect at $\mathbf{s} = \tilde{\mathbf{s}}$, it is necessary that $\mathbf{z}$ have components of 0 in the direction of the null-space bases of $\tilde{\mathrm{M}}$. This condition acts as constraints on the local orientation of the manifolds that must be met for them to intentionally intersect. For instance, if $\tilde{\mathrm{M}}$ is rank $2(n-m)$, then $\ker(\tilde{\mathrm{M}}) = n-\{2(n-m)\} = 2m-n$, so there are $2m-n$ constraints on $\mathbf{z}$. If $\tilde{\mathrm{M}}$ is rank $2(n-m)-1$, then one pair of bases $(\mathbf{u}_j, \mathbf{v}_k)$ is linearly dependent. This dependency creates one constraint for $\tilde{\mathrm{M}}$ in addition to the $2m-n+1$ constraints applicable to $\mathbf{z}$ for a total of $2m-n+2$ constraints on Eq. (3.42). For two pdfs that satisfy Eq. (3.33) and intersect, the local dimension $d_\times$ of the intersection is

$$d_\times = 2(n-m) - \mathrm{rank}(\tilde{\mathrm{M}}). \tag{3.44}$$

At the intersection of the local Euclidian space equivalents of pdfs $f$ and $g$, the two spaces must share bases. Therefore, $d_\times$ is the number of dependent column pairs in M. Note that $\min(\mathrm{rank}(\tilde{\mathrm{M}})) = n-m \Rightarrow \max(d_\times) = n-m$, since we assumed $\{\mathbf{v}\}$ and $\{\mathbf{u}\}$ both spanned $\mathbb{R}^{n-m}$.

### 3.6.3 Application to Space Situational Awareness

Applying the theory in the previous section back to the realm of the too-short arc problem, consider bearing-only observations where angular rates are regarded as directly observed: if the state space is 6-dimensional, the codimension of each pdf is 4. Suppose we have multiple generalized ARs $F_C[\mathbf{X}(t^1); \mathfrak{Y}^1]$, $F_C[\mathbf{X}(t^2); \mathfrak{Y}^2]$, ..., $F_C[\mathbf{X}(t^n); \mathfrak{Y}^n]$, based on a set of criteria $C$, each corresponding to unassociated optical tracks at different times. To determine whether these observations are associated to each other, we map their respective generalized ARs to a common state space and propagate them to a common epoch time $\tau$ with some transformation $\mathcal{T}(\tau, t^i)$, where $i = 1, 2, \ldots, n$. Assuming Hamiltonian dynamics, $\mathcal{T}(\tau, t^i) = T(\tau, t^i)$. If the observations are related, we expect a non-zero posterior pdf $h(\tau; \mathfrak{Y}_1, \mathfrak{Y}_2, t_1, t_2)$ if we were to apply

Bayes' rule to their corresponding generalized ARs

$$h(\tau;\mathfrak{Y}_1,\mathfrak{Y}_2,t_1,t_2)=\frac{\left[T(\tau,t^1)\circ F_C[\mathbf{X}(t^1);\mathfrak{Y}^1]\right]\cdot\left[T(\tau,t^2)\circ F_C[\mathbf{X}(t^2);\mathfrak{Y}^2]\right]}{\int\{[T(\tau,t_1)\circ F_C[\mathbf{X}(t^1);\mathfrak{Y}^1]]\cdot[T(\tau,t_2)\circ F_C[\mathbf{X}(t^2);\mathfrak{Y}^2]]\}\,\mathrm{d}\mathbf{X}}, \tag{3.45}$$

where the integral is over the entire state space $\mathbf{X}$. Graphically, if $h\neq 0$, then the support of the generalized ARs intersect because $h>0$ for a subspace where both $f>0$ and $g>0$, and the probability expressed by $h$ is one that is evaluated over this intersection. Figure 3.4 is a graphical representation of these pdfs. Again, since the support of two generalized ARs do not intersect generically in a 6-dimensional space, one can simply look at whether $h>0$ for some region in the state space to deduce with confidence whether or not the two observations are associated. Furthermore, $h$ provides an initial orbit estimate of the observed object with an associated pdf. This estimate can be introduced as the reference orbit for a statistical orbit determination method, such as the Kalman filter [79].

By treating the information from the optical observations as pdfs, not only are we able to combine the information from multiple optical tracks, we can also fuse different types of observations as long as they are similarly expressed as pdfs over the state space. For instance, information regarding the spatial distribution of debris can be extracted from a model such as MASTER-2005 so that unrealistic objects are excluded from the AR [55].

## 3.7 Efficient Algorithms For Admissible Region Mapping

In Section 3.6.2, a technique of correlating two optical observations by computing the intersection between their generalized ARs in a discretized standard the state space was proposed. This method, however, requires mapping a large number of sample points from range / range-rate space to, say, Poincaré space to ensure accuracy. Attempting to exactly map these points can be computationally expensive. This section shows how to speed up this process via linearization and linear extrapolation. Numerical examples that illustrates the speed and accuracy of such methods over Monte Carlo are also provided.

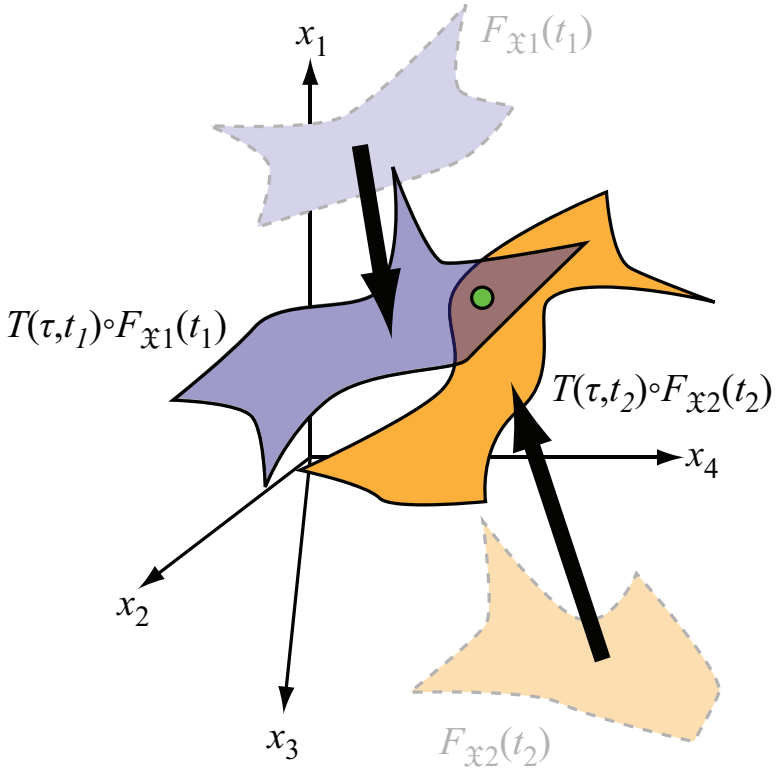


Figure 3.4: Map $T$ evolves admissible regions $F_{\mathfrak{Y}1}(t_1)$ (blue) and $F_{\mathfrak{Y}2}(t_2)$ [orange] from two separate observations to a common epoch $\tau$. The intersection point [green] is where the observed object most likely exists in state space.

### 3.7.1 Linearization Algorithm

Suppose that the state space is discretized with $M$ bins. Given some attributable vector $\mathfrak{Y}$, its AR is computed and an infinite sample set $S_2$ is formed. Define $\tilde{S}_2$ as a subset of $S_2$ that includes enough samples to fill in every bin that $S_2$ does. Consider the smallest possible $\tilde{S}_2$ (i.e. it has just enough samples to fill in all the relevant bins) and let $\Xi = n(\tilde{S}_2)$ in this case, where $n(\cdot)$ gives the number of elements in the input set. Generally, $\Xi$ is very large. Even if restricted to a 3-dimensional the state space, $\Xi \sim 10^7$ for $M \sim 10^{12}$, and this value is expected to be larger for the full 6-dimensional analysis. Mapping so many points exactly (non-linearly) can become a bottleneck for the correlation algorithm.

In the linear method, some smaller subset of $S_2$ composed of $\xi$ ($< \Xi$) elements is used, which is defined as $\tilde{\tilde{S}}_2$, and only these points are mapped exactly. $\xi$ should be chosen so that it balances map accuracy and computational speed. Again, $\tilde{\tilde{S}}_2$ is uniform over $\rho$-$\dot{\rho}$ space. Consider one element of $\tilde{\tilde{S}}_2$ located at $(\rho^*, \dot{\rho}^*)$ in $\rho$-$\dot{\rho}$ space and $\mathbf{X}^*$ in the state space. Then, to first order accuracy, some point $(\rho, \dot{\rho})$ in the vicinity of $(\rho^*, \dot{\rho}^*)$ is mapped to the state space as

$$\mathbf{X} = \mathbf{X}^* + \delta\mathbf{X} \approx \mathbf{X}^* + \Phi \begin{pmatrix} \delta\rho \\ \\ \delta\dot{\rho} \end{pmatrix}, \tag{3.46}$$

from Eq. (3.18). $\delta$ denotes a small deviation and $\Phi$ is the linear map from $\rho$-$\dot{\rho}$ to the state space. Figure 3.5 shows a grid over $\rho$-$\dot{\rho}$ space defined by points from $\tilde{\tilde{S}}_2$ as asterisks, and the particular element of interest as vertex 1. The coordinate $\mathbf{X}_1$ of vertex 1 in the state space is, by definition, $\mathbf{X}_1 = \mathbf{X}^*$.

The aim here is to map the bounded plane $323'2'$ linearly from $\rho$-$\dot{\rho}$ space to the state space. Analytically, it can be shown that only two adjacent vertices need to be mapped from the plane to the state space to accomplish this goal: enough points are obtained to define the normal vector of the plane in the $\rho$-$\dot{\rho}$ space, and the coordinates of its boundaries can be found by symmetry. For instance, using Eq. (3.46), map vertices

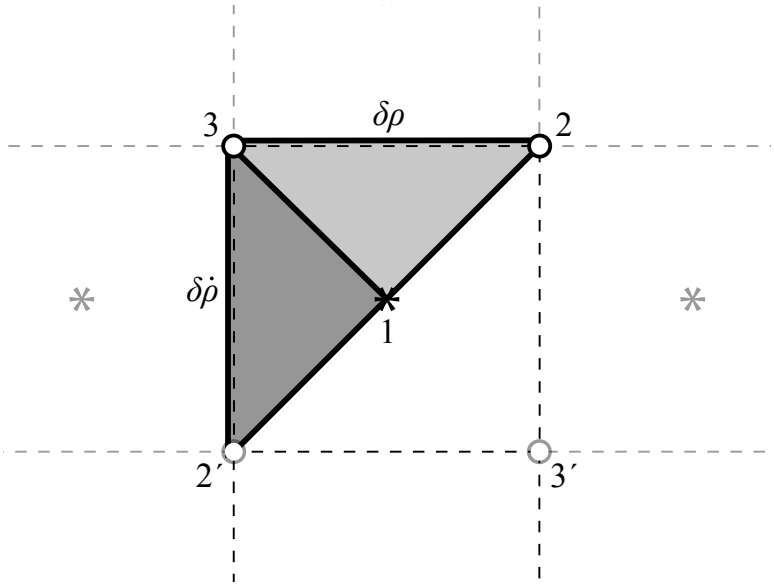


Figure 3.5: Grid in $\rho$-$\dot{\rho}$ for the linear map of $\tilde{\tilde{S}}_2$.

2 and 3 to the state space

$$\mathbf{X}_2 \approx \mathbf{X}_1 + \Phi \begin{pmatrix} \delta\rho/2 \\ \delta\dot{\rho}/2 \end{pmatrix} \tag{3.47}$$

$$\mathbf{X}_3 \approx \mathbf{X}_1 + \Phi \begin{pmatrix} -\delta\rho/2 \\ \delta\dot{\rho}/2 \end{pmatrix}, \tag{3.48}$$

where now $\delta\rho$ and $\delta\dot{\rho}$ are explicitly the width and height of the $\tilde{\tilde{S}}_2$ element grid. Furthermore, just as in the $\rho$-$\dot{\rho}$ space, $2'$ should be the mirror point of 2 with respect to line 13 in the state space as well. Similarly, $3'$ should be the mirror point of 3 with respect to line 12. As a consequence, the coordinates $\mathbf{X}_{2'}$ and $\mathbf{X}_{3'}$ of vertices $2'$ and $3'$, respectively, in the state space is

$$\begin{aligned} \mathbf{X}_{2'} &= -\mathbf{X}_2 + 2\mathbf{X}_1 \\ \mathbf{X}_{3'} &= -\mathbf{X}_3 + 2\mathbf{X}_1. \end{aligned} \tag{3.49}$$

Numerically, one would like to uniformly sample the $323'2'$ map with as few points as possible without losing information regarding its location and boundaries in the state space. That is, the objective is to know all the bins that the map fills, and how much each bin is filled – the former is considered in this section, and the latter in Section 3.7.2. Suppose we assign to each bin a unique bin index vector $\mathbf{i} = (i_1, i_2, \ldots, i_j, \ldots, i_n)^T \in \mathbb{N}^n$ such that $1 \leq i_j \leq M_j$ for all $j \in \mathbb{N}, 1 \leq j \leq n$, where $\mathbf{M} = (M_1, M_2, \ldots, M_j, \ldots, M_n)^T$ is the number of bins in each coordinate direction. For a general $n$-dimensional space, it is useful to let the axes of $\mathbf{i}$ align with the axes of $\mathbf{X} = (x_1, x_2, \ldots, x_n)^T$ and resize the state space to match the scaling of the index vector space. Define the state space coordinates $\bar{\mathbf{X}} = (\bar{x}_1, \bar{x}_2, \ldots, \bar{x}_n)^T$ such that

$$i_j = \text{floor}(\bar{x}_j) = \begin{cases} \text{floor}\left[M_j(x_j - x_{j,\min})/(x_{j,\max} - x_{j,\min}) + 1\right] & (x_j \neq x_{j,\max}) \\ M_j & (x_j = x_{j,\max}) \end{cases} \tag{3.50}$$

where $1 \leq j \leq n$ and $\mathbf{X}_{\max} = (x_{1,\max}, x_{2,\max}, \ldots, x_{j,\max}, \ldots, x_{n,\max})^T$ and $\mathbf{X}_{\min} = (x_{1,\min}, x_{2,\min}, \ldots, x_{j,\min}, \ldots, x_{n,\min})^T$ are the maximum and minimum possible values of $\mathbf{X}$ in each coordinate direction as determined by the discretization, respectively. With this transformation, $1 \leq \bar{x}_j \leq M_j$ like $i_j$, except $i_j \in \mathbb{N}$ but $\bar{x}_j \in \mathbb{R}$.

Now map points 1, 2, 2′, and 3 as described by Eqs. (3.46) and (3.50) to $\bar{\mathbf{X}}$ the state space. The reason why vertex 3′ need not be mapped will become apparent later. Linear features in $\rho$-$\dot{\rho}$ space remain linear in the map, so the following can be said regarding points on the map of line segment 23

$$\bar{\mathbf{X}}(\kappa) = (\bar{\mathbf{X}}_3 - \bar{\mathbf{X}}_2)\kappa + \bar{\mathbf{X}}_2 \;\Rightarrow\; \bar{x}_j(\kappa) = (\bar{x}_{3,j} - \bar{x}_{2,j})\kappa + \bar{x}_{2,j}, \tag{3.51}$$

where $\bar{\mathbf{X}}_2 = (\bar{x}_{2,1}, \bar{x}_{2,2}, \ldots, \bar{x}_{2,n})^T$ and so on, and $\kappa$ is some parameter such that $0 \leq \kappa \leq 1$. As an example, Figure 3.6 graphically represents each component of some $\bar{\mathbf{X}}(\kappa)$ along a line segment in 3-space as it changes with $\kappa$. $\kappa$ is minimally sampled without losing information by, in addition to initial condition $\kappa = 0$, solving for the $\kappa$ values where these discontinuities occur, which are indicated by the black dotted lines in Figure 3.6. Taking the inverse of Eq. (3.51),

$$\kappa = \frac{i_j - \bar{x}_{2,j}}{\bar{x}_{3,j} - \bar{x}_{2,j}}, \tag{3.52}$$

where $\text{floor}(\min(\bar{x}_{2,j}, \bar{x}_{3,j})) < i_j \leq \text{floor}(\max(\bar{x}_{2,j}, \bar{x}_{3,j}))$. This process is repeated for lines 12, 13, 2′3, and 12′.

Suppose all the indices of the bins that the map of line 23 cuts through are known, and denote them as $\{\mathbf{i}\} = \{\mathbf{c}_1, \mathbf{c}_2, \ldots, \mathbf{c}_k\}$. Notice that if $\triangle 123$ is regarded as a collection of lines between the map of point 1 in $\bar{\mathbf{X}}$-space and bins $\{\mathbf{c}_1, \mathbf{c}_2, \ldots, \mathbf{c}_k\}$, one can utilize the linear extrapolation method expressed by Eq. (3.51). That is, the triangle is sampled using a scan of lines. Undersampling of the plane may occur, but this problem can be mitigated by either taking more points on the map of 23 with linear extrapolation, or by repeating the sampling process for the remaining two vertex-hypotenuse combinations 3-12 and 2-13. The same argument can be made for $\triangle 12'3$. Finally, to complete the bounded plane $323'2'$, it is enough to mirror the two triangular maps that were just found about the map of line 2'2. Apply Eq. (3.49) to the bin indices at each bin that is filled. The map of vertex 3′ is computed as a consequence of this projection.

### 3.7.2 Determining the Intersection of Planes and Hypercubes

The algorithm in Section 3.7.1 determines the bins that one linear map of a bounded region in the AR fills. Figure 3.7 is a diagram of the direct map of the AR, the linear map of a segment of it, and the bin structure in 3-space. The linear map will remain to be a 2-dimensional plane in the full 6-dimensional

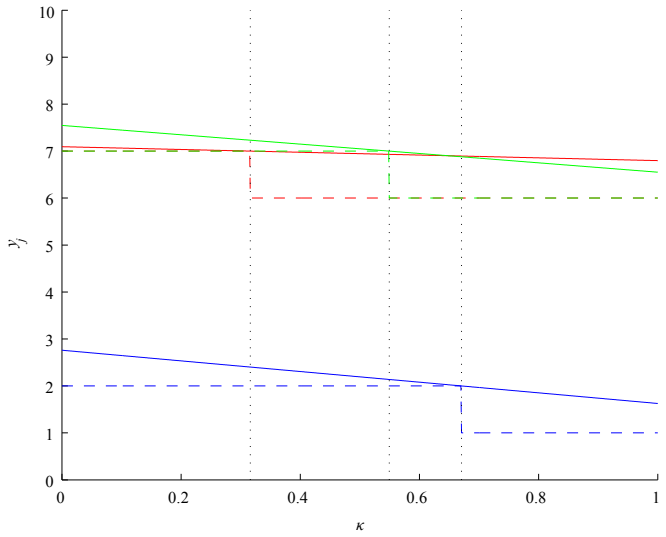


Figure 3.6: Components of $\bar{\mathbf{X}}$ in 3-space along a line segment parameterized by $\kappa$. Each bold line represents a different component of $\bar{\mathbf{X}}$ as a function of $\kappa$, and the dashed line represents the corresponding bin index for each value of $\kappa$. The black dotted lines are the values of $\kappa$ for which this line segment cuts through a bin boundary; this line segment cuts through bins $\mathbf{i} = (\text{red}, \text{green}, \text{blue})^T = (7,7,2)^T$, $(6,7,2)^T$, $(6,6,2)^T$, and $(6,6,1)^T$.

problem. The goal now is to find how much the linear map fills each bin that it cuts through; that is, to solve for the area that the linear map occupies in each bin. Assuming the AR is a uniform distribution in the range / range-rate space, the area of a segment of an AR is directly proportional to the integral over that segment. The discretized value of the AR in a particular bin is the sum of the areas of all linear map segments that reside in it.

Begin by expressing some arbitrary point $\mathbf{X}$ on the plane as follows

$$\mathbf{X} = \mathbf{X}_1 + s\mathbf{v}_1 + t\mathbf{v}_2, \tag{3.53}$$

where $s$ and $t$ are some parameters such that $0 \leq s, t \leq 1$, and

$$\mathbf{v}_1 = \mathbf{X}_2 - \mathbf{X}_1 = (v_{1,1}, v_{1,2}, \ldots, v_{1,n})^T \tag{3.54}$$

$$\mathbf{v}_2 = \mathbf{X}_3 - \mathbf{X}_1 = (v_{2,1}, v_{2,2}, \ldots, v_{2,n})^T. \tag{3.55}$$

$(s, t)$ gives a universal description a position on the linear map with respect to a skewed coordinate system $\{\mathbf{v}_1, \mathbf{v}_2\}$. For any linear map of a section of the AR, any point on the map lies within a diamond shaped region on the $s$-$t$ plane bounded by

$$\begin{cases} s + t = 0 \\ s + t = 2 \\ -s + t = 0 \\ -s + t = -2. \end{cases} \tag{3.56}$$

The bins are now strictly defined using a set of inequalities. Suppose that the hyperplanes that form the bin boundaries lie along the coordinate axes of the state space. Then, for some bin $i$ centered at $\mathbf{X}_C = (x_{C,1}, x_{C,2}, \ldots, x_{C,n})^T$ with width $\Delta\mathbf{X} = (\Delta x_1, \Delta x_2, \ldots, \Delta x_n)^T$ in each coordinate direction, the space that it

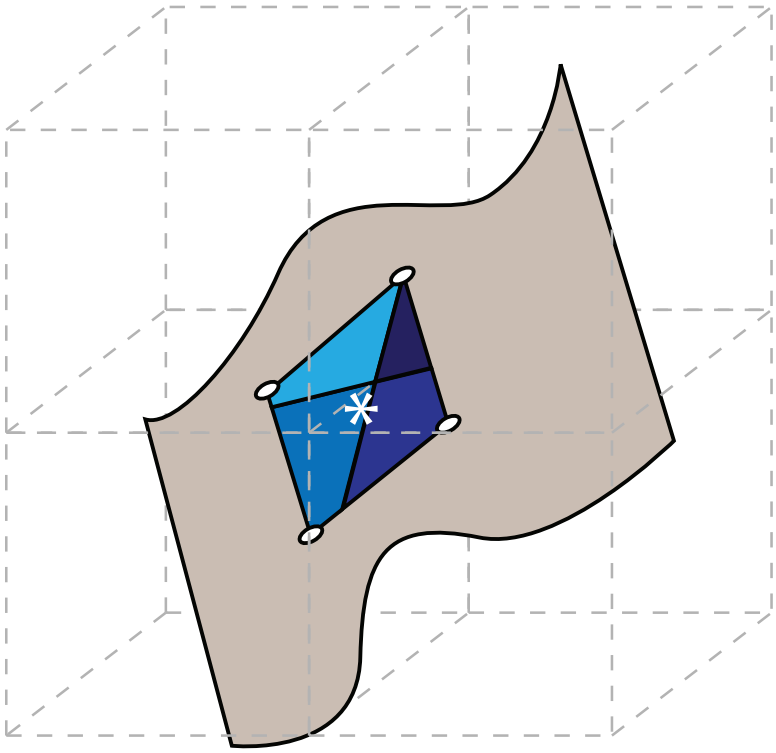

Figure 3.7: A 3-dimensional representation of the linear mapping process. The gray dashed lines represent the boundaries of the bins. The brown surface is the admissible region map, and the blue plane is a portion of the admissible region mapped to the state space about the asterisk. The plane cuts through 4 bins; regions belonging to different bins are distinguished by the shading.

fills in the state space is

$$\begin{cases} x_1 \geq x_{C,1} - \Delta x_1/2 \\ x_1 \leq x_{C,1} + \Delta x_1/2 \\ x_2 \geq x_{C,2} - \Delta x_2/2 \\ x_2 \leq x_{C,2} + \Delta x_2/2 \\ \quad \vdots \\ x_n \geq x_{C,n} - \Delta x_n/2 \\ x_n \leq x_{C,n} + \Delta x_n/2. \end{cases} \tag{3.57}$$

Since the bins are mutually exclusive, if the linear map intersects bin $i$, then the projection of the bin boundaries on to the map, or more specifically on to the $s$-$t$ plane, should form a closed region that traces out how bin $i$ cuts the map. Furthermore, the area of this region is directly proportional to the area that the map occupies in bin $i$. To project, say, the first inequality of Eq. (3.57), use the right hand side as a constraint to the first component of Eq. (3.53)

$$x_{C,1} - \Delta x_1/2 \leq x_{1,1} + sv_{1,1} + tv_{2,1} \Leftrightarrow v_{1,1}s + v_{2,1}t \geq x_{C,1} - x_{1,1} - \Delta x_1/2. \tag{3.58}$$

The remaining inequalities of Eq. (3.57) also project as half planes on the $s$-$t$ plane. Again, since the bins are mutually exclusive and the linear map is bounded, the intersection of these half planes form a closed region. Figure 3.8 shows an example of how the bin boundaries get projected onto the $s$-$t$ plane. Efficient methods of finding this intersecting region is found in Preparata and Shamos [60]. Finally, the area $A$ of the region is found with the following formula

$$A = \frac{1}{2} \left| s_1 t_2 - s_2 t_1 + s_2 t_3 - s_3 t_2 + \cdots + s_{k-1} t_k - s_k t_{k-1} + s_k t_1 - s_1 t_k \right|, \tag{3.59}$$

where $(s_j, t_j)$ is the coordinate of one of the $k$ vertices of the region, and the vertical lines represent absolute value.

Repeat the linearization and projection processes explained in Sections 3.7.1 and 3.7.2 for all objects in $\tilde{\tilde{S}}_2$, a small uniform subset of $S_2$. For each bin, compute the sum of areas of all of the linear map segments that cut through it; note that this value is proportional to the discretized value of the AR pdf in that bin. The final generalized AR is found by normalizing these sums over all bins.

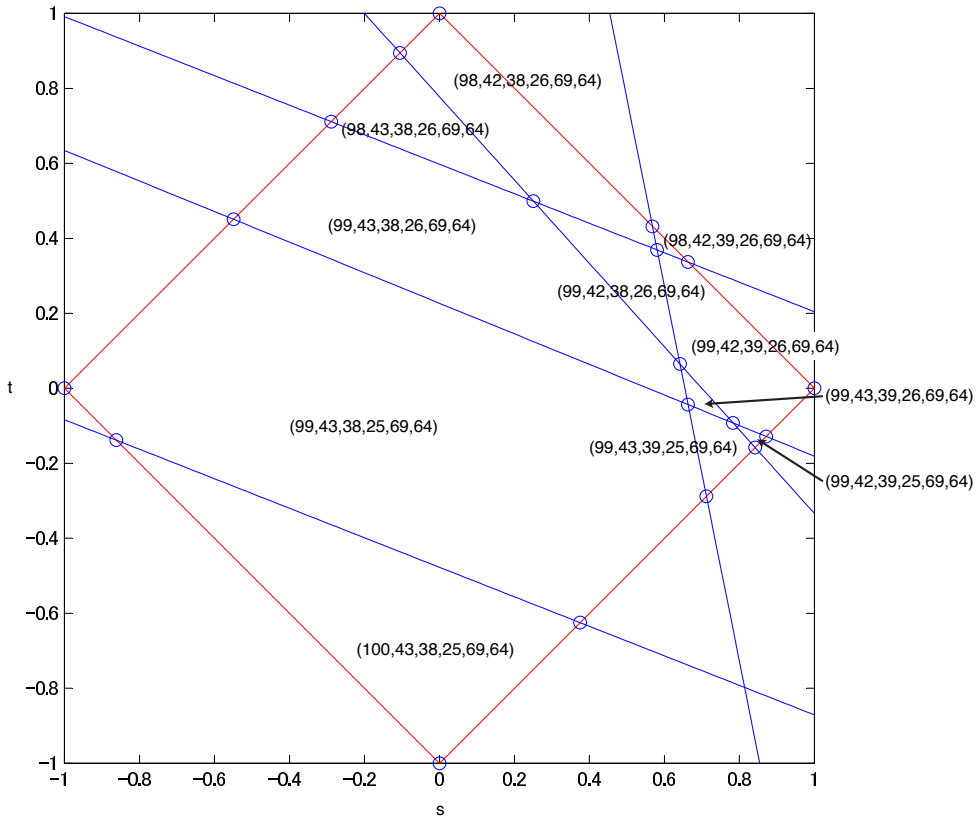


Figure 3.8: An *s*-*t* plane diagram for a linear map of the admissible region defined by $\bar{\mathbf{X}}_1$ = (99.556, 43.021, 38.964, 25.941, 69.507, 64.876)$^T$, $\bar{\mathbf{X}}_2$ = (99.19, 42.991, 39.019, 26.047, 69.492, 64.873)$^T$, and $\bar{\mathbf{X}}_3$ = (98.626, 42.994, 38.975, 26.201, 69.498, 64.877)$^T$. The red lines represent the linear map boundaries, the blue lines the bin boundaries, and the blue dots all of the intersection points. The indices of the different bins that project onto the linear map are labeled accordingly.

### 3.7.3 Benefits of the Linear Map

The speed and accuracy of the linear map are assessed based on an implementation in MATLAB. All computations are carried out on a dual-core Xeon server with double floating point precision. An AR based on an observation of an object in GEO ($\mathfrak{Y} = (\alpha, \delta, \dot{\alpha}, \dot{\delta}, \phi, \Theta)^T$ = (75.681 deg, −5.1347 deg, 14.841 arcsec/sec, 0.56513 arcsec/sec, 114.59 deg, 57.295 deg)$^T$) is mapped to the 6-dimensional Poincaré space using both the full non-linear and the linear transformations. The distribution in the range / range-rate space is assumed to be uniform. The propagation time is set to 0; the transformation is entirely static. The "truth" distribution is the map from the non-linear transformation with $\Xi = n(\tilde{S}_2) = 3000 \times 3000 = 9 \times 10^6$ sample points, which is the maximum sample size the code allowed to fit in memory. On the other hand, $\xi = n(\tilde{\tilde{S}}_2) = 500 \times 500 = 250,000$ for the linear map. The discretization of the Poincaré space is such that

$$\mathbf{X}_{\min} = (4.4621, 0, -5.0241, -5.0241, -5.0241, -5.0241) \tag{3.60}$$

$$\mathbf{X}_{\max} = (12.6206, 6.2832, 5.0241, 5.0241, 5.0241, 5.0241) \tag{3.61}$$

$$\mathbf{M} = (100, 77, 123, 123, 123, 123), \tag{3.62}$$

where $\mathbf{X}_{\min}$ and $\mathbf{X}_{\max}$ are the bounds of the space and $\mathbf{M}$ is the number of bins in each Poincaré orbit element direction. Units are in Earth radii - kg - hr. Consequently, the total number of bins is $1.7624 \times 10^{12}$. The bounds for $\mathbf{X}$ are chosen so that almost all objects in the JSpOC TLE catalog are included, and $\mathbf{M}$ is chosen so that the length of the edges of each bin are roughly equal ($\approx 0.082$.) As a rough measure, each bin spans $\sim$ 450 km in the semi-major axis direction and $\sim 4.7°$ in the mean anomaly direction. If more precise initial orbit determination is desired, we recommend refining the discretization only over regions where two pdfs overlap so as not to significantly increase computational burden. A similar idea is explored in Section 3.8.1.

Table 3.2 shows the amount of time required to compute each respective map, and their spatial and density accuracies compared to the "truth" distribution. The measure of spatial accuracy is the ratio of bins that are filled by both the "truth" distribution and the distribution of concern; e.g. the linear map fills 97.0% of the bins that the "truth" distribution fills. The measure of density accuracy is the the ratio of bins whose densities are within at least 20% relative error of the "truth" distribution; e.g. for the linear map, 92.4% of bins will have a density error relative to the "truth" distribution of less than 20%. These results indicate that

the linear map attains better accuracy than the non-linear map with the same number of sample (reference) points while still finishing computation faster than the "truth" distribution case.

Table 3.2: Computation time, spatial accuracy, and density accuracy between the non-linear (full) and linear admissible region maps. †: The computation time of the non-linear map does not scale linearly with sample size, since for larger samples a less efficient sorting algorithm must be used due to memory constraints.

| | **Full** $(3000 \times 3000)$ | **Full** $(500 \times 500)$ | **Linear** $(500 \times 500)$ |
|---|---|---|---|
| CPU time [min] | $6823^{\dagger}$ | 3 | 35 |
| Spacial Accuracy | – | 0.848 | 0.970 |
| Density Accuracy | – | 0.703 | 0.924 |

It is important to note that the high density accuracy of the linear map is possible only when the state space is non-singular. For singular variables, components of $\Phi$ can become very large, and thus Eq. (3.46) is no longer a valid approximation. Table 3.3 compares the density accuracy of the linear map using non-singular Poincaré variables and singular Keplerian orbital elements for the same GEO object AR as in the previous example. For the Keplerian orbital elements, even though the accuracy of the non-linear map is comparable to Poincaré elements, the linear map performs much worse.

Table 3.3: Density accuracy for linear maps of non-singular Poincaré orbit elements and the singular Keplerian orbital elements.

| | **Full** $(500 \times 500)$ | **Linear** $(500 \times 500)$ |
|---|---|---|
| Poincaré | 0.703 | 0.924 |
| Classical | 0.664 | 0.789 |

### 3.7.4 Planar Mesh Mapping of Admissible Region Subregions

One problem with the above linear mapping method is that vertices from different subregions may not match up, leading to reduced accuracy. See Figure 3.9 for a graphical representation. In order to alleviate this inconsistency when even higher map accuracy is desired than the linear map, we divide the subregion into two triangles: $\triangle 32'3'$ and $\triangle 323'$. All vertices are mapped non-linearly; we still assume, however, that the resulting maps in the Poincaré orbit element space are 2-dimensional planes each defined by their vertices.

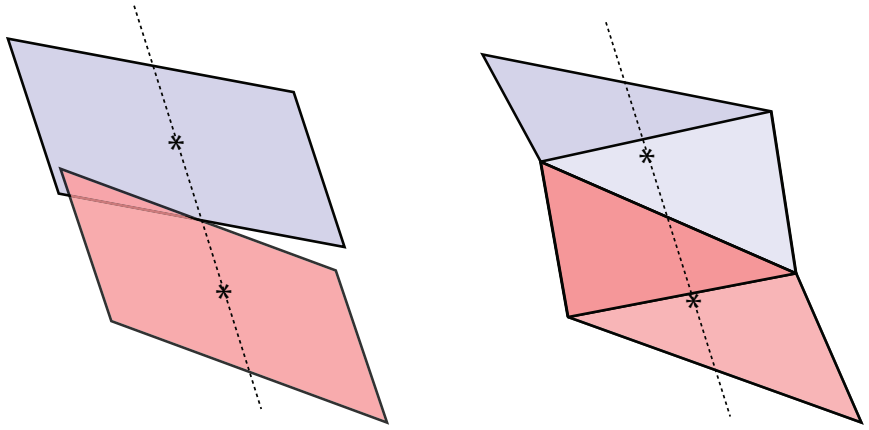

Figure 3.9: A schematic of local mapping of the admissible region using the linear (left) and planar mesh (right) techniques. The figure is an isometric view. The planar regions indicate local maps with respect to each reference point, indicated by the asterisks. Since each local map has different reference points, there will be inconsistencies (i.e. gaps) at the edges. The planar mesh map alleviates this problem because the mapping of vertices is more precise.

Thus, we are still able to use a linear extrapolation in Section 3.7.2 to deduce the Poincaré coordinates of points within each triangular map. Since it is impossible to fit a square plane to 4 vertices which are mapped non-linearly, the subregions must now be triangular. The resulting AR map is akin to a planar mesh of the actual manifold. The non-linear transformation of the vertices can be done in several ways. The most straightforward way is to numerically propagate them with the exact transformation $T$. A more efficient method, particularly for long propagation times, is the use of analytical or semi-analytical propagation. One example of the latter is the state transition tensor (STT) concept which is outlined in Section 2.2; this is the approach taken in the following section.

### 3.7.5 Benefits of the Planar Mesh Map

The difference in map accuracy of the linear and planar mesh maps is assessed based on an implementation in MATLAB. All computations are carried out on a quad-core Xeon workstation with double floating-point precision. An AR based on an error-free ground-based observation of object EM1 (c.f. Appendix B, $\mathfrak{Y} = (\alpha, \delta, \dot{\alpha}, \dot{\delta}, \phi, \Theta)^{\mathrm{T}} = (-30.970 \text{ deg}, -16.019 \text{ deg}, 8.6740 \text{ arcsec/sec}, -0.7013 \text{ arcsec/sec}, 302.71 \text{ deg}, 114.59 \text{ deg})^{\mathrm{T}}$) is mapped to the 6-dimensional Poincaré space using the exact, linear, and planar mesh with STT transformations. The distribution in the range / range-rate space is again assumed to be

uniform. Two-body dynamics is used. The AR is mapped dynamically backwards in time by 48 hours. The reference "truth" map is the map from the exact transformation with $9 \times 10^6$ sample points, which is the maximum sample size that MATLAB allowed to fit in memory. On the other hand, $3.85 \times 10^5$ reference points are used for the linear and STT maps. The pdf is inferred from the density of sample points at each bin for the exact map, and from the aforementioned projection technique for the linear and planar mesh maps. The discretization of the Poincaré space is such that

$$\mathbf{X}_{\text{min}} = (4.4621, 0, -3, -3, -4, -4), \mathbf{X}_{\text{max}} = (12.6206, 6.2832, 3, 3, 4, 4) \tag{3.63}$$

$$\mathbf{M} = (100, 77, 73, 73, 98, 98), \tag{3.64}$$

with units in Earth radii - kg - hour. Consequently, the total number of bins is $3.9408 \times 10^{11}$.

Two metrics are introduced to evaluate the performance of the maps. We refer to the admissible map of concern as $T \circ F$ and the "truth" map as $T_{\text{truth}} \circ F$, where $T$ maps the AR $F$ from range / range-rate space to the Poincaré orbit element space. The spacial spacial metric is the same as in Section 3.7.3. The density metric is redefined to examine both the mean and standard deviation of the absolute relative errors of the pdf compared to the "truth" map.

Table 3.4 summarizes the results. We find that the planar map is better than the linear map in all metrics, with the greatest benefit being the increase in precision of the probability density. Furthermore, as is seen in Figure 3.10, the planar mesh map fills in many bins in middle Earth orbit (MEO) and GEO altitudes that the linear map misses, most likely because the subregion boundaries match up without gaps as in Figure 3.9. Since these altitude ranges are where most of the RSOs exist, computational capabilities permitting, we recommend using the planar mesh map over the linear map.

## 3.8 Limiting Cases

This section investigates special observations cases where the direct Bayesian AR algorithm is expected to have difficulty in calculating an accurate initial orbit estimate: namely, when an object is observed simultaneously at two observation points or when objects in a satellite constellation are observed over long periods of time.

Table 3.4: Spatial and density accuracy metrics for the linear and planar mesh maps as well as runtimes for all three methods: Exact, Linear, and Planar Mesh. $\Delta$ is the difference in metrics between the linear and planar maps; bold letters indicate improvement.

| | **Spatial** | **Density** | | **Runtime [min]** |
|---|---|---|---|---|
| | | Mean | Std. Dev. | |
| Exact ("Truth") | – | – | – | 144 |
| Linear | 0.99883 | 0.26849 | 0.80939 | 66 |
| Planar Mesh | 0.99945 | 0.26228 | 0.69194 | 72 |
| $\Delta$ | **+0.00062** | **-0.00561** | **-0.11745** | +6 |

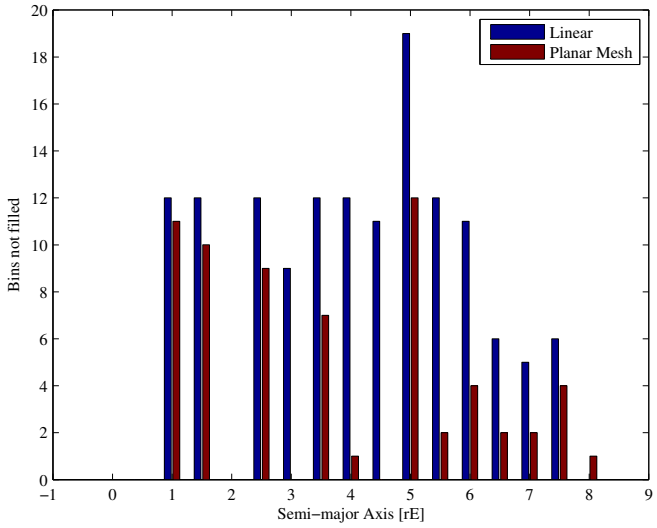


Figure 3.10: A histogram of the number of bins in the "truth" distribution which are not included in the linear (blue) and planar mesh (red) maps as a function of the semi-major axis of that bin. Number of bins are accumulated over one Earth radius.

### 3.8.1 Simultaneous Observations of an Object

The proposed algorithm may run into difficulties computing a precise state estimate when the two pdfs are nearly tangent. Although such pdfs would still most likely intersect at a single point, they may appear to occupy the same bins in the discretized state space (i.e. overlap) over a large region. One case where pdfs become nearly tangent is when an object is observed simultaneously from 2 different observations points, as seen in Figure 3.11. Here, pdf $h$ spans over 688 bins using the discretization in Section 3.7.3. This result, however, does not imply that the two pdfs intersect over a large planar region; from Eq. (3.26), 2-dimensional intersections of pdfs are extremely unlikely. Indeed, as the discretization is refined by 20%, then 50%, the overlap region begins to converge upon the coordinate of the true object state.

In a practical implementation of this method, a recursive algorithm that reduces bin size over the overlapping region should be used whenever the combined pdf spans a large area. Compared to the method proposed by Maruskin et al. that evaluates intersections of manifolds within their 2-dimensional projections, the new algorithm converges faster as the intersections are evaluated in the full 6-dimensional space [46].

### 3.8.2 Observations of Satellite Constellations

Suppose there exist two optical observations made at one observatory but separated in time by, say, 4 hours, and that they are consistent with the same orbit plane. One can either conclude that one object was observed with an orbital period that is any divisor of four, or that two different objects in a satellite constellation separated in phase by 4 hours are observed. For this particular example, most of the solutions in the former set will have semi-major axes that are too small to be included in the AR. If the temporal separation of the observations are larger, however, then single-object solutions may become viable. The long-term propagation "dilutes" information regarding the object's angular position that can be extracted from the observation separation time.

Mathematically, let two objects be on an orbit with period $\tau$ separated by mean anomaly $\Delta M$. In two-body motion, $\tau$ is related to semi-major axis as $\tau = 2\pi\sqrt{a^3/\mu}$. Suppose one of the objects is observed at time 0, and then the other at time $N\tau + (\Delta M/n)$, where $N \in \mathbb{N}$ and $n$ is the mean motion; i.e. the second object is

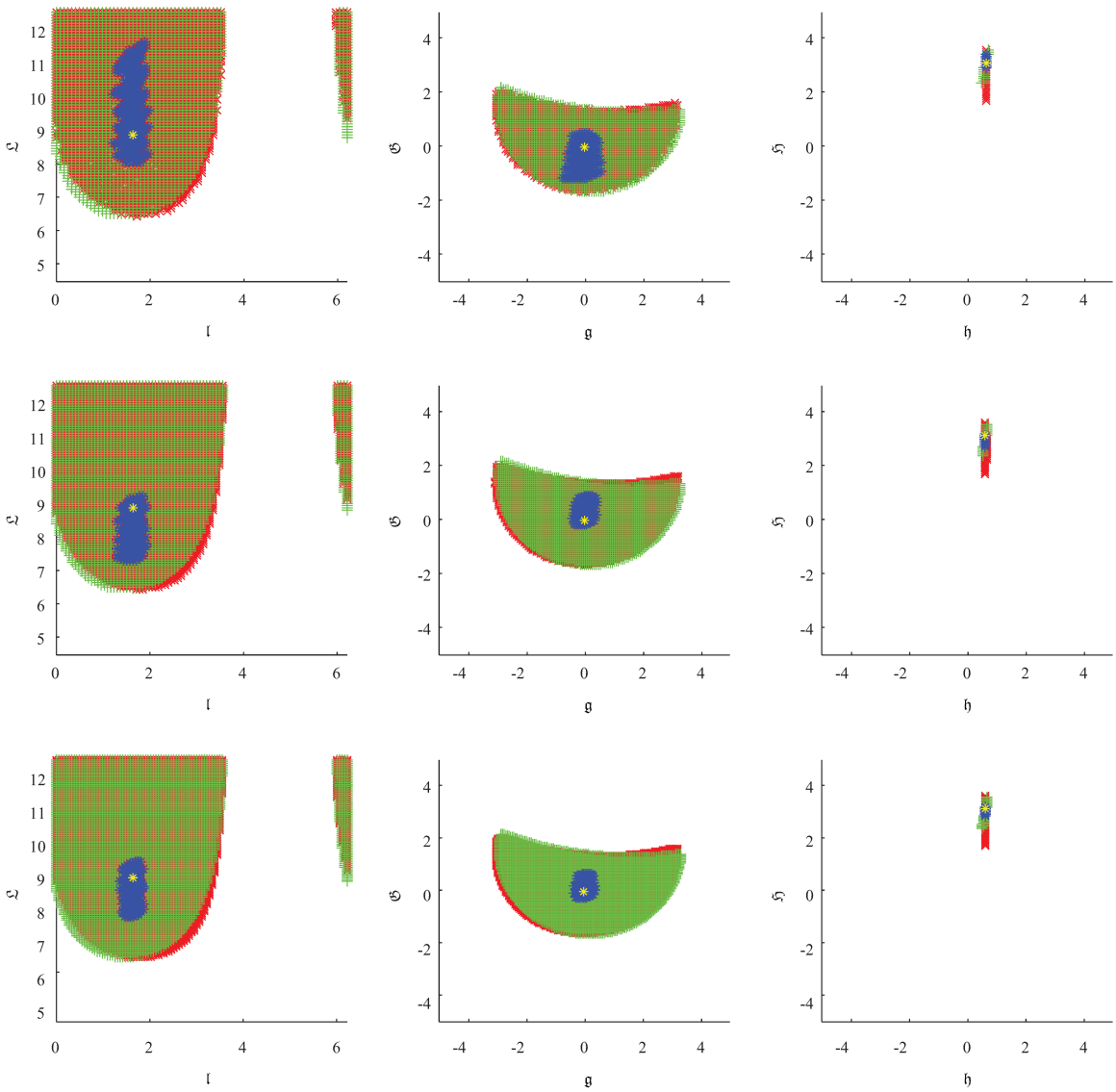

Figure 3.11: Combined pdf $h$ of two near-parallel pdfs (CM1 observed simultaneously at ($\phi$ [deg], $\Theta$ [deg]) = $(57.296, 57.295)$ and $(114.59, 85.944)$ at time $t = 26.36$ hours; c.f. Appendix B) as the discretization is refined from $M = 1.7624 \times 10^{12}$ (top) to $1.2M$ (middle) and $1.5M$ (bottom).

observed after $N$ revolutions. Now, if one were to wrongly assume that the same object was observed twice, then the true anomaly $a + \Delta a$ of this ficticious object is

$$2\pi N \sqrt{\frac{a^3}{\mu}} + \frac{\Delta M}{n} = 2\pi N \sqrt{\frac{(a+\Delta a)^3}{\mu}} \tag{3.65}$$

$$\Leftrightarrow \frac{\Delta a}{a} = \left(1 + \frac{\Delta M}{2\pi N}\right)^{2/3} - 1. \tag{3.66}$$

Therefore, $N \to \infty \;\Rightarrow\; \Delta a/a \to 0$. If the first observation generated a non-empty AR, then it is likely that the proposed algorithm will mistakenly correlate the second observation given the two observations are temporally well-separated.

Figure 3.12 is a graphical representation of the above scenario. 2 separate objects ($\Delta M = 2/3\pi$) in a constellation are simulated to be observed from one observatory with different observation separation times. When the separation is 14.85 hours, the combined pdf is null at all bins, meaning the algorithm successfully recognizes the observations as those of different objects. When the separation is increased to 60.61 hours, however, the two pdfs overlap, and thus a "false positive" result is obtained.

## 3.9 Simulated Example: Ground-Based Observations

This section discusses results from an implementation of the direct Bayesian AR method in MATLAB with simulated ground-based observations. A general orbit determination scenario is considered where a set observations are associated with the algorithm discussed above. 8 objects are extracted from the JSpOC TLE catalog to obtain a sample set; they are referred to as follows [1]

> 3 objects in GEO (GEO1∼3), 1 object in a Molniya orbit (MOL1), 2 object in an eccentric MEO orbit (EM1), 1 GPS satellite (GPS1), and 3 objects in LEO (LEO1∼3)

The orbital parameters of each object are given in Appendix B. The observed object set is chosen so that an array of useful orbits in various altitudes, eccentricities, and inclinations are included. 128 zero-error observations of right ascension, declination, and their time derivatives made from 4 ground observatories are simulated for all 8 objects over the course of 5 days. Thus $\mathfrak{X} = (\alpha, \delta, \dot{\alpha}, \dot{\delta}, t_0, \Theta, \phi)$, where $t_0$ is the observation epoch and $(\Theta, \phi)$ is the inertial angular position of the observation point. The zero-error assumption is assumed to be good because the uncertainty in the angular information is generally much less

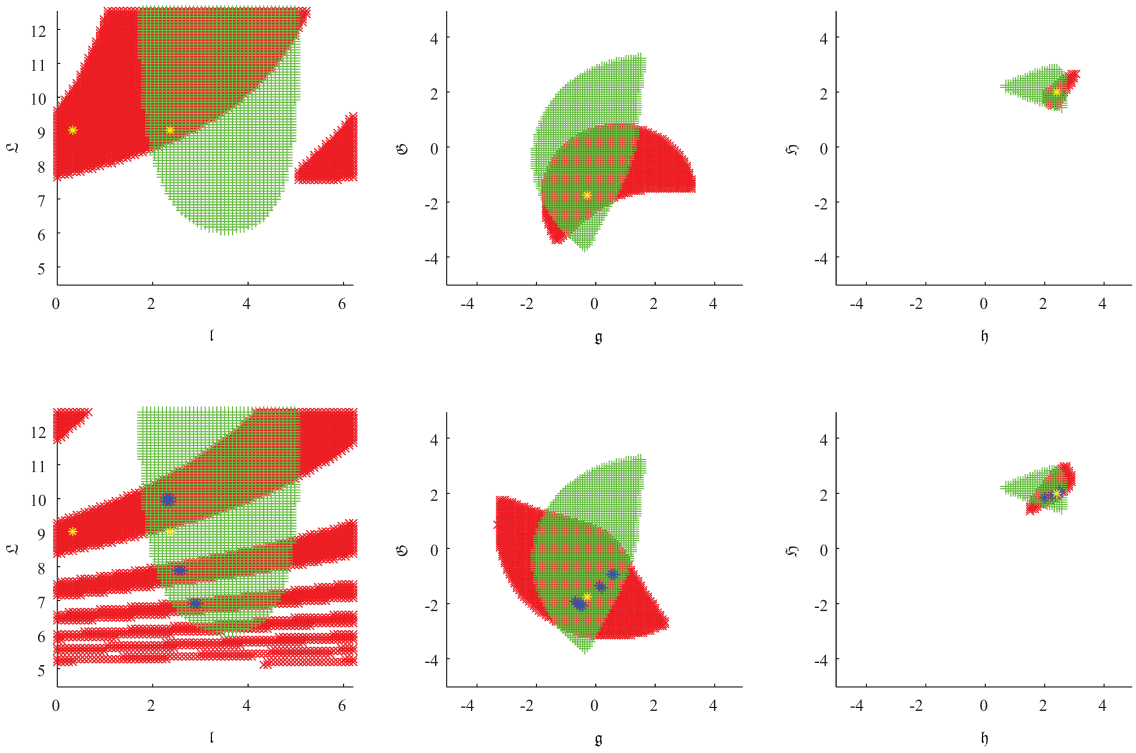

Figure 3.12: Correlation of observations of 2 different objects separated by a mean anomaly of $2/3\pi$ rad on the same orbital plane as EM2 (c.f. Appendix B). Observations are separated by 14.85 hours (top) and 60.61 hours (bottom). All observations are made at ($\phi$ [deg], $\Theta$ [deg]) = (229.18, 114.59).

than the uncertainty in the range and range-rate; refer to Chapter 4.1 for a discussion regarding the effects of observation error on the outcome of the algorithm. The 4 observations points are located at

- Socorro, New Mexico (33.8172°N 106.6599°W)
- Maui, Hawaii (20.7088°N 156.2578°W)
- Diego Garcia, British Indian Ocean Territory (7.41173°S 72.45222°E)
- Morón Air Base, Spain (37.170°N 5.609°W)

Approximately every 12 hours, the algorithm generates attributable vectors (i.e., simulated observations) for all objects that are above the local horizon at any given observation point. No *a priori* information is assumed regarding the observed objects, and thus a uniform initial pdf over range / range-rate is used. The AR mapping is approximated with the planar mesh STT method. The discretization of the Poincaré space is the same as in Section 3.7.5. For simplicity, all dynamics are assumed to be two-body to ensure fast computational turnaround; again, this simplification is not central to the theory discussed. One point of interest is that dynamical modeling error will manifest as the inflation of the AR maps over time. This phenomenon is already partially accounted for by the fact that we have converted the aforementioned maps from 2-dimensional manifolds to pdfs discretized over 6-dimensional hypercubes.

Figure 3.13 is a graphical representation of the process explained in Section 3.6.3 for 2 observations. The red and green regions each represent pdfs based on observations that have been dynamically evolved to a common epoch (i.e. pdfs $f$ and $g$). The propagation has "shredded" the red pdf in the $\mathfrak{Q}$-$\mathfrak{l}$ plane [46]. The blue region is the combined distribution (i.e. pdf $h$). The yellow asterisk is the true state of the observed object. The distributions have been projected onto 2-dimensional subspaces using their coordinate-conjugate momentum pairs; note, however, that the correlation is conducted in the full 6-dimensional Poincaré space. When correlating two observations of the same object (top), $h > 0$ for a very small region of the state space; for this particular example, $h > 0$ for 11 bins. Furthermore, the true state is included in the region in state space where $h > 0$. Therefore, the state estimate is good. On the other hand, when two observations are of different objects (bottom), $h = 0$ for the entire state space, which allows one to conclude that the two

observations are unrelated.

Our correlation process performs well for all 128 observations: all observations are correctly correlated to the 9 objects and their states are correctly estimated down to a region of at most 11 bins out of $1.7624 \times 10^{12}$. That is, there are no "false positive" results. Again, as a rough measure, each bin spans $\sim$ 450 km in the semi-major axis direction and $\sim 4.7^\circ$ in the mean anomaly direction. With the same setup as in Section 3.7.3, each correlation run took approximately 5 minutes. To further reduce the region over which $h > 0$ as well as reduce computation time, one can assume *a priori* that all observed objects are included in either the JSpOC TLE catalog or some debris distribution model instead of the uniform distribution assumption made for Figure 3.13. Then, the AR maps are "pre-conditioned" to exclude unrealistic objects. Correlation times are reduced to 1 to 2 minutes. Table 3.9 lists the number of overlap bins for each correlated object. Pseudo code for the correlation algorithm is given in Appendix C.

Table 3.5: The estimation accuracy of each observed object when using a uniform initial pdf (left) and the JSpOC TLE catalog as the initial pdf (right). All sides of each bin are approximately 0.082 in length where the units are in the Earth radii - kg - hr system.

| | **Uniform** | | **Pre-Conditioned** | |
|---|---|---|---|---|
| $\{r\}$ | Overlap bins | Contains true state | Overlap bins | Contains true state |
| GEO1 | 6 | YES | 3 | YES |
| GEO2 | 5 | YES | 1 | YES |
| GEO3 | 2 | YES | 2 | YES |
| MOL1 | 1 | YES | 1 | YES |
| EM1 | 2 | YES | 1 | YES |
| GPS1 | 2 | YES | 1 | YES |
| LEO1 | 6 | YES | 1 | YES |
| LEO2 | 8 | YES | 2 | YES |
| LEO3 | 11 | YES | 1 | YES |

Initially, the correlation algorithm was set up to correlate observations first to last; i.e. it correlates the $j$-th observation with $j+1$ th, and if this case fails $j$-th with $j+2$ th, and so on. Since the observations are generated in 15 minute intervals, it was often the case that the initial overlap region between two correlated observations spanned up to $10^3$ bins. As a consequence, subsequent correlation runs took more time than in the more optimal case where the observations are separated more and thus the overlap spans over only a

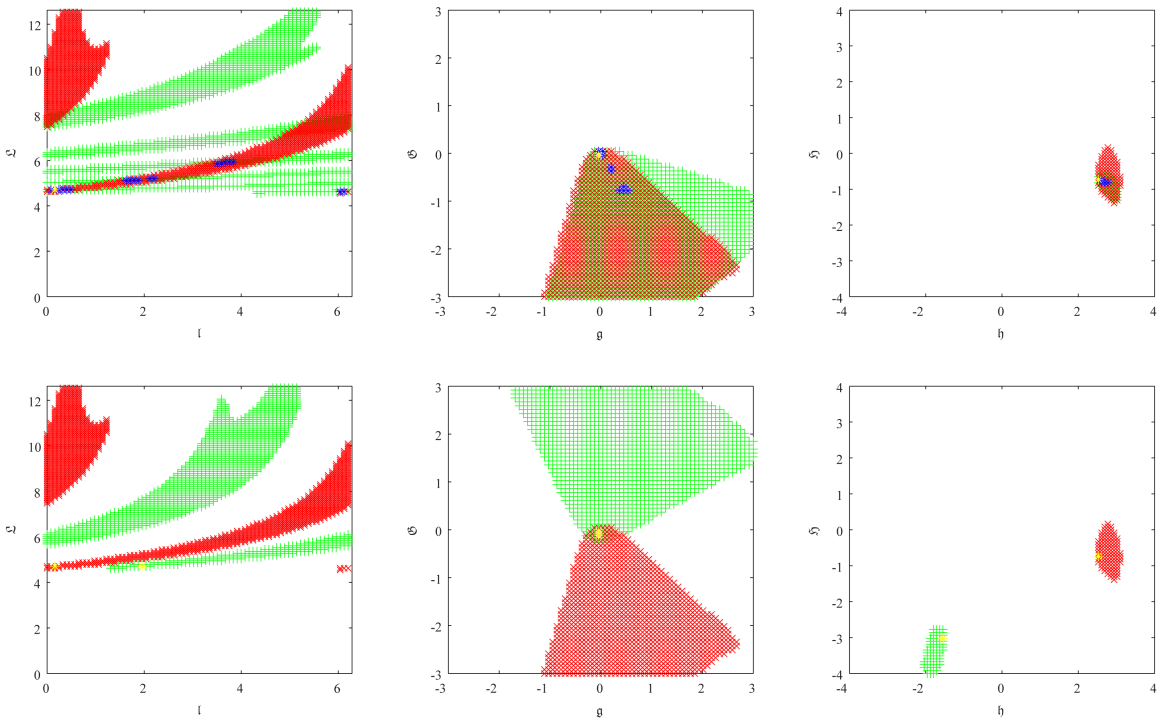

Figure 3.13: Projections of probability distributions when correlating observations of two different objects (top; LEO2-LEO3) and the same object (bottom; LEO2-LEO2). Length units in Earth radii, time units in hours, angle units in radians.

few bins. Consequently, the algorithm is modified so that it correlates objects last to first; i.e. it correlates the $j$-th observation with the $N$-th, then $j$-th with $N-1$ th, and so on, where $N$ is the total number of observations in the current batch. Then, the observations in each correlation run are separated by up to 24 hours, which indeed reduces the initial overlap size. It should be noted that, although not encountered in this current example, the two objects in GEO in the object set could act like satellites in a constellation, causing fictitious overlaps when correlating observations from two separate objects in GEO. In conclusion, there exists an advantageous separation time between observations such that the corresponding pdfs are perpendicular enough to produce a small overlap region which is not fictitious. This idea shall be discussed again in Section 5.4.

## 3.10 Simulated Example: Space-Based Observations

The goal in this section is to associate simulated observations from LEO and GEO of objects in both MEO and GEO so that the direct Bayesian AR method is corroborated to work for space-based observations. The observed objects are:

> 3 objects in GEO (GEO 1~3), 1 object in a Molniya orbit (MOL1), 2 objects in an eccentric MEO orbit (EM1, 2), 1 object in a circular MEO orbit (CM1), 1 object in a GPS orbit (GPS1)

and observing satellites are:

> 1 satellite in LEO (LEO-O), 1 satellite in GEO (GEO-O).

Their orbit elements are listed in Appendix B. The LEO observing satellite orbit is similar to that of the SBSS system. The GEO observer is intended to simulate an optical sensor as a hosted payload on a GEO commercial satellite.

### 3.10.1 False Association via the Observing Satellite's State

For any attributable vector, the VO corresponding to $(\rho, \dot{\rho}) = (0, 0)$ always maps to the state of the observing satellite. Therefore, if one is to include the origin of the range / range-rate space in the AR, then

the AR maps of any two observations will intersect at this point, leading to false associations and degenerate orbit solutions as the posterior pdf $h > 0$ over this intersection. Figure 3.14 is an example of one such degenerate case. The intersecting region indeed includes the state of the observing satellite but not any of the observed satellites.

One can remove the observer's solution by reformulating the range criterion for the ARs as follows

$$C_2' = \{(\rho, \dot{\rho}) : \rho_{\text{MIN}} \leq \rho \leq 14\} \tag{3.67}$$

where $\rho_{\text{MIN}} > 0$. $(\rho, \dot{\rho}) = (0, 0)$ is no longer included in the AR, so the AR maps themselves should not intersect. A false intersection may still be detected by the algorithm, however, depending on the discretization size. That is, if the "cutout" region corresponding to $0 \leq \rho \leq \rho_{\text{MIN}}$ is completely contained within a single discretization cell, then a false positive association is detected. Thus, it is necessary to refine the discretization over the overlap area of the AR maps. This step can be achieved by dividing the sides of the bins according to some integer refinement factor: e.g. a factor of 3 will give 729 new bins per old bin. Bear in mind that the refinement is only valid to the accuracy of the AR maps, which is in turn mainly driven by the observation accuracy. In the following examples, zero observation error is assumed: the refinement technique is applied only to show the theoretical validity of the AR method for space-based observations.

### 3.10.2 Observer at LEO

Considered here is an association of a batch of simulated space-based observations with the AR method. In this example, 101 error-free observations of the 8 objects in the object set are simulated over 48 hours from a near-circular, sun-synchronous orbit at 630 km altitude (LEO-O); refer to Section 4.2 for a discussion regarding the effects of observation error on the outcome of the algorithm. Observations are made every 10 minutes, but the same object is not observed twice for at least two hours. This setup ensures that at least 2 observations of each object are made over the simulation time span as well as that observations per object are sparse. Occultation due to the Earth is considered by modeling the Earth and its atmosphere as an opaque sphere of radius 6578 km. Since the focus of this section is on the dynamical and topological aspects of the AR method, lighting is assumed to be good regardless of observation geometry,

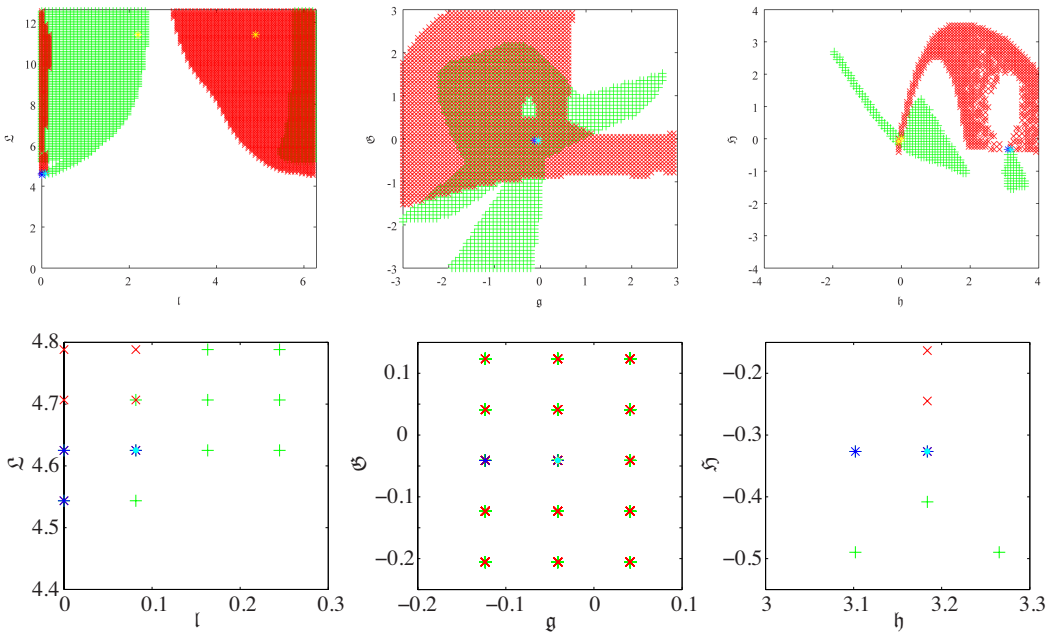

Figure 3.14: Projections of admissible region maps when associating observations from LEO-O of two different objects (GEO1-GEO2). Each subplot is a 2-dimensional subspace of the Poincaré space. Regions where the associated pdf for GEO1 is non-zero are in red, GEO2 in green. The blue region is where the posterior pdf is non-zero; i.e. where the two maps intersect. The yellow asterisks indicate the true state of the observed objects, and the cyan asterisk is the state of the observing satellite. The bottom plot is a zoom in of the top plot focusing on the blue region. Units of length are in Earth radii, time in hours, and angle in radians.

although future detailed simulations should take the phase angle with respect to the sun into account. The AR mapping is approximated with the planar mesh method with full numerical propagation of segment vertices. The Earth's zonal harmonics up to fifth order are considered and the dynamics are integrated using a variable step seventh / eighth order Runge-Kutta algorithm [28]. The Poincaré space discretization is the same as in Section 3.7.5. $\rho_{\text{MIN}}$ = 20 km and the discretization is refined by a factor of 25. The refinement factor is chosen with trial and error to ensure that the degenerate solution is excluded without excess computational burden. Table 3.6 is a summary of the results. Observations are correctly associated and the state of all objects are correctly estimated, indicating that the AR method is a viable option for both associating LEO-based observations and providing an initial orbit estimate.

Table 3.6: The estimation accuracy of objects observed (GEO1∼GPS1) for a space-based observer in a low Earth orbit LEO-O. For each object observed ("Object"), the number of observations processed ("Number of Obs.") as well as the number of discretization bins that the posterior pdf is non-zero ("Overlap Bins") are listed. "True Sol." and "Degenerate Sol." indicate whether the observed objects' states or the observing satellite's state, respectively, are included in the solution. All sides of each bin are approximately 0.082 in length where the units are in the Earth radii - kg - hr system.

| **Object** | **Number of Obs.** | **Overlap Bins** | **True Sol.** | **Degenerate Sol.** |
|---|---|---|---|---|
| GEO1 | 14 | 3 | YES | NO |
| GEO2 | 14 | 2 | YES | NO |
| GEO3 | 12 | 2 | YES | NO |
| MOL1 | 13 | 1 | YES | NO |
| EM1 | 11 | 1 | YES | NO |
| EM2 | 13 | 2 | YES | NO |
| CM1 | 12 | 2 | YES | NO |
| GPS1 | 12 | 4 | YES | NO |

### 3.10.3 Observer at GEO

When a similar problem as in the previous section is considered for an observer in GEO, the lack of relative motion makes it difficult to remove the degenerate solution. In this example, 2 error-free observations are simulated over 5 hours for each of the 3 GEO objects (GEO1-3) in the object set from a GEO orbit (GEO-O), for a total of 6 observations. Observations are made every 30 minutes, but the same object is not observed twice for at least 4 hours. Geometric considerations, the dynamics of objects, and the discretiza-

tion of the Poincaré space are the same as the LEO example. $\rho_{\text{MIN}} = 50$ km and the discretization refinement factor is set to 75. Table 2 is a summary of the results. Although no false positive associations are observed, the initial orbit estimates all contain the observing satellite's state. Due to the slow relative motion in GEO, the AR maps remain near parallel to each other, and thus a very fine refinement of the state space is required to differentiate between the two manifolds near the degenerate solution. Consequently, if more observations are to be processed, it is highly likely that they will not be correctly associated as any AR map will intersect at the degenerate solution.

Table 3.7: The estimation accuracy of each observation pair ("Obs. Pair") for the GEO-O observer. $\Delta t$ is the time between observations in hours. All sides of each bin are approximately 0.082 in length where the units are in the Earth radii - kg - hr system.

| **Obs. Pair** | $\Delta t$ | **Overlap bins** | **True Sol.** | **Degenerate Sol.** |
|---|---|---|---|---|
| GEO1-GEO1 | 4.0 | 17 | YES | YES |
| GEO1-GEO2 | 0.5 | 0 | – | – |
| GEO1-GEO3 | 1.0 | 0 | – | – |
| GEO2-GEO2 | 4.0 | 14 | YES | YES |
| GEO2-GEO3 | 0.5 | 0 | – | – |
| GEO3-GEO3 | 4.0 | 24 | YES | YES |

Similar difficulty in distinguishing between the states of the observed and observing satellites for the Gooding method is mentioned in Vallado as well as Schaeperkoetter and Mortari [65,87]. Poor observability for close proximity tracking in GEO is well documented analytically [71, 81, 89]; regardless of the coordinate frame used, observability in the linear sense is weak if not lost whenever the observer and the observed objects are stationary relative to each other. Woffinden proposes conducting maneuvers to improve observability, but this approach is not reasonable for SSA, where tens of thousands of space-based observations may be made per day [53].

As a solution, eccentricity ($e = 0.0001 \rightarrow e = 0.001$) and inclination ($i = 0.0057^\circ \rightarrow i = 0.25^\circ$) are added to the observer's orbit: this new orbit is referred to as GEO-O'. The time gap between observations is also increased to up to 16 hours to further introduce dynamical change. Table 3 shows the improved performance. Here, 35 observations over approximately 60 hours are processed. Note that similarly increasing the observation time gap for the GEO-O observer produced fictitious solutions due to an ambiguity in the

number of revolutions the observed object made between observations; refer to Section 3.8.2. In order to conduct state estimation based solely on GEO-on-GEO optical observations without *a priori* information on the observed object, an orbit like GEO-O' that ensures relative motion is beneficial from an astrodynamics standpoint.

Table 3.8: The estimation accuracy of each observed object for an improved GEO (GEO-O') observer. All sides of each bin are approximately 0.082 in length where the units are in the Earth radii - kg - hr system.

| **Object** | **Number of Obs.** | **Overlap Bins** | **True Sol.** | **Degenerate Sol.** |
|---|---|---|---|---|
| GEO1 | 5 | 6 | YES | NO |
| GEO2 | 5 | 3 | YES | NO |
| GEO3 | 5 | 5 | YES | NO |
| MOL1 | 4 | 1 | YES | NO |
| EM1 | 3 | 7 | YES | NO |
| EM2 | 4 | 2 | YES | NO |
| CM1 | 4 | 2 | YES | NO |
| GPS1 | 4 | 3 | YES | NO |

## 3.11 Conclusions

In this chapter, a new approach to the estimation of Earth-orbiting objects was proposed where observations were expressed as probability density functions that represent not only their errors but also the limited knowledge in the unobserved variables. The functions, referred to as admissible regions, are bounded by a set of physical constraints. Bayes' rule is directly applied to associate multiple observations and subsequently obtain an orbit estimate. Because the admissible region maps are 2-dimensional manifolds when perfect measurements are assumed, we conclude from topological arguments that they do not intersect generically. As a consequence, a positive correlation also simultaneously provides an initial orbit estimate. A method of linearly extrapolating sub-regions of the admissible region to the discretized Poincaré space is shown to improve computational turn-around without significant loss of map accuracy. Two limiting cases are examined: one where orbit estimation accuracy may be compromised if the time between observations is short, and another where false correlations may occur if objects in a satellite constellation are observed. The direct Bayesian admissible region method is applied to both ground- and space-based simulated obser-

vations. For the former, 128 observations are successfully associated and the initial orbit estimates are good. For the latter, the observer's state is always included in the admissible region map, causing all observations to associate with all other observations. At a theoretical level, this problem can be solved by setting a lower bound on the observation range larger than 0. Although this solution worked well for the 101 observations tested for a low Earth orbit observer, the slow dynamics inhibits its effectiveness particularly for an observation satellite in geostationary orbit. If one is to place an observer near geosynchronous objects, from the standpoint of initial orbit determination, efforts to introduce dynamical change are beneficial, such as increasing the observation time gap, or increasing the inclination and eccentricity of the observer. As future work, more perturbing forces relevant to resident space objects should be added to the simulations, such as solar radiation pressure and atmospheric drag. Simultaneously, the effects of dynamic modeling errors to the admissible region maps should be further studied.

# Chapter 4

## Addressing Errors in The Direct Bayesian Admissible Region Method

So far, all of the theory and examples discussed assumed zero observation error to argue the problem's sparseness. This simplification was deemed to be appropriate since the error in the observation data ($\sim 10^0$ arcsec in angles) is typically much smaller than the uncertainty associated with range and range-rate ($\sim 10^0$ Earth radii and Earth radii/hour in range and range-rate, respectively). Nevertheless, it is important to know quantitatively the effects of errors in observation information to the association and initial orbit determination results. Of particular interest is how much the observation error would "inflate" the admissible region (AR) maps in the state space, as the addition of observational errors would, in principle, increase the dimensionality of the AR from 2 to 6. Ignoring large errors will result in both false positives and negatives, and to this end, a detailed treatment of observational error for the direct Bayesian AR method is given in this chapter.

The outline of this chapter is as follows. For ground-based observations, the linear map of a displacement in the attributable vector space to the Poincaré orbital element space is considered in quasi-Monte Carlo fashion over a sample set of reference orbits. The direction and magnitude of the mapped displacements are an indication of the "inflation" that occurs when measurement errors are added to the AR. A number of specific orbit determination scenarios are especially prone to failed associations. For space-based observations, the attributable vector is higher in dimension due to the inclusion of position and velocity of the observer, making the above Monte Carlo analysis infeasible. Thus, a simpler analysis focusing on the magnitude of mapped displacements is employed. Finally, two ways to explicitly take into account errors are proposed: one where the linear extrapolation map is generalized to higher dimensions, and another where a

least squares batch is applied to the direct Bayesian results.

## 4.1 Effects of Measurement Errors on The Admissible Region: Ground-Based Observations

27000 objects are considered distributed uniformly in the semi-major axis ($19134.3 \leq a\,[\text{km}] \leq 51024.8$), eccentricity ($0 \leq e \leq 0.8$), and inclination ($-90^\circ \leq i \leq 90^\circ$) spaces but randomly in the other Keplerian orbital elements. The observation point is also randomly chosen for each object so that the observation takes place at least 11.5° above the horizon. This approach ensures more control over the sample set than choosing objects directly from ARs. Each state is then displaced in the 6 coordinate directions of the inertial topocentric spherical coordinate frame one by one: $\Delta\rho = 6.059$ km, $\Delta\dot{\rho} = 13.71$ km/hr, $\Delta\alpha = \Delta\delta = 1.62$ arcsec, and $\Delta\dot{\alpha} = \Delta\dot{\delta} = 3.6 \cdot 10^{-3}$ arcsec/sec [46]. These displacements correspond to the size of one admissible region sample subset when the sample size is $\sim 10^5$ and Gaussian observation errors of $\sigma = 2$ arcsec in both $\alpha$ and $\delta$ are considered up to 3-$\sigma$. The displacements are mapped statically to the Poincaré orbital element space ($\mathfrak{L}$, $\mathfrak{l}$, $\mathfrak{G}$, $\mathfrak{g}$, $\mathfrak{H}$, $\mathfrak{h}$) via a linear transformation $\Phi_S = \Phi_3 \circ \Phi_2 \circ \Phi_1$ similar to Section 3.4.2, where

$$\Phi_1 = \left.\frac{\partial(x, y, z, \dot{x}, \dot{y}, \dot{z})}{\partial(\rho, \dot{\rho}, \alpha, \delta, \dot{\alpha}, \dot{\delta})}\right|_*, \Phi_2 = \left.\frac{\partial(a, e, i, \Omega, \omega, M)}{\partial(x, y, z, \dot{x}, \dot{y}, \dot{z})}\right|_* \tag{4.1}$$

$$\Phi_3 = \left.\frac{\partial(\mathfrak{L}, \mathfrak{l}, \mathfrak{G}, \mathfrak{g}, \mathfrak{H}, \mathfrak{h})}{\partial(a, e, i, \Omega, \omega, M)}\right|_*, \tag{4.2}$$

the asterisks indicate that the partials are evaluated along a reference state, and $(x, y, z, \dot{x}, \dot{y}, \dot{z})$ are the Cartesian states. Here, the state of the observed object is used as the reference. Finally, the dynamics from the initial epoch $t^0$ to some time $\tau$ are added also linearly with a state transition matrix $\Phi_4(\tau, t^0)$ such that the complete linear map is

$$\Phi(\tau, t^0) = \Phi_4(\tau, t^0) \circ \Phi_S(t^0). \tag{4.3}$$

For simplicity, two-body dynamics is assumed so that $\Phi_4(\tau, t^0)$ is given analytically as Eq. (3.25).

Figure 4.1 shows the magnitude of the mapped displacements for all simulation cases. The different colors represent different coordinate directions in the spherical coordinates. The simulations are indexed in lexicographical order with $a$, $e$, and $i$ as bases; thus, as the index increases, $a$ monotonically increases. The

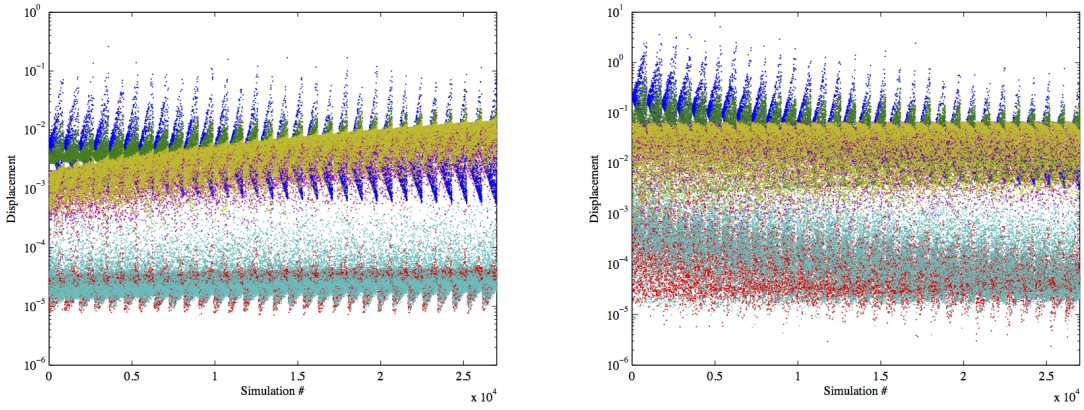


Figure 4.1: Norm of displacement in the $\rho$ (blue), $\dot{\rho}$ (green), $\alpha$ (red), $\delta$ (cyan), $\dot{\alpha}$ (purple), and $\dot{\delta}$ (gold) directions when mapped to the Poincaré orbital element space. Time propagated for 0 (left) and 120 hours (right).

errors in the angles, on the average, have an order 2 to 3 smaller effect on the map compared to the other variables. Therefore, it is possible to ignore them and reduce the dimensionality of the problem from 6 to 4 in many situations. The exceptions are when the velocity of the object is high ($\sim$ 8 km/s and higher), as indicated in Figure 4.2, and when the velocity is parallel to the direction of the error, as indicated in Figure 4.3. In either case, the angular error affects the orientation of the orbit plane in addition to the position of the object on the orbit.

In addition, the mapped displacement in the $\dot{\alpha}$ and $\dot{\delta}$ reach the same order of magnitude as those in the $\rho$ and $\dot{\rho}$ as either semi-major axis or propagation time increases. The growth makes sense: a larger semi-major axis is akin to a longer "lever arm" amplifying angle-rate errors, and longer propagation times allow for the dynamics to greatly deform the state space. The map in the $\rho$ direction, however, is nearly parallel to the map in either $\dot{\alpha}$ or $\dot{\delta}$ especially when propagation times are on the order of days: refer to Tables 4.1 and 4.2. The dynamics stretches the state space in the l-direction (equivalent to the $M$-direction in Keplerian orbital elements), causing the displacement vectors to align with each other. In fact, when the admissible region is propagated by 120 hours, the mapped displacement in both $\dot{\alpha}$ and $\dot{\delta}$ are within 30° of that in $\rho$ for over 80% of the tested cases. A scatter plot of the smaller angle between the range and either range-rate is given in Figure 4.4, and of the larger angle in Figure 4.5.

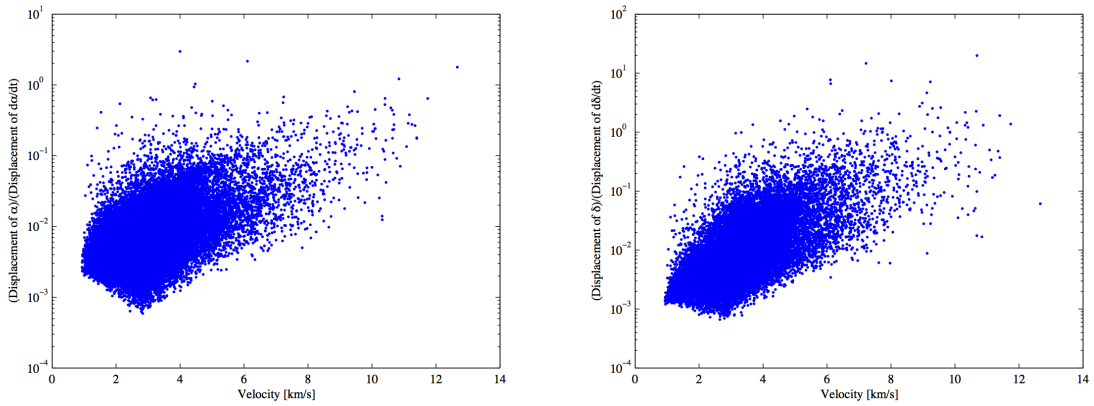


Figure 4.2: Left: ratio between the norm of the displacement in $\alpha$ and $\dot{\alpha}$ when mapped to the Poincaré orbital element space versus the velocity of the observed object. Right: similar plot but for $\delta$ and $\dot{\delta}$.

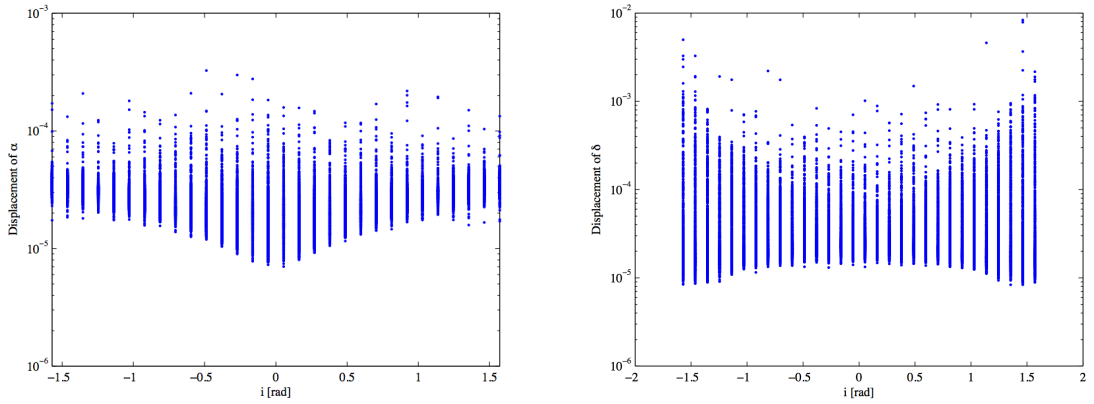


Figure 4.3: Left: ratio between the norm of the displacement in $\alpha$ when mapped to the Poincaré orbital element space versus the object's inclination. Right: similar plot but for $\delta$.

Table 4.1: Percentage of simulation sample points where the smaller angle between the map of the displacement in the range and either angle-rate meets the criterion indicated in the top row. Values for two propagation times ($\Delta t$) are shown.

| | $< 10$ deg | $< 30$ deg |
|---|---|---|
| $\Delta t = 0$ | 35.49 | 86.94 |
| $\Delta t = 120$ h | 98.62 | 100.00 |

Table 4.2: Percentage of simulation sample points where the larger angle between the map of the displacement in the range and either angle-rate meets the criterion indicated in the top row. Values for two propagation times ($\Delta t$) are shown.

| | $< 10$ deg | $< 30$ deg |
|---|---|---|
| $\Delta t = 0$ | 1.39 | 22.58 |
| $\Delta t = 120$ h | 58.30 | 82.54 |

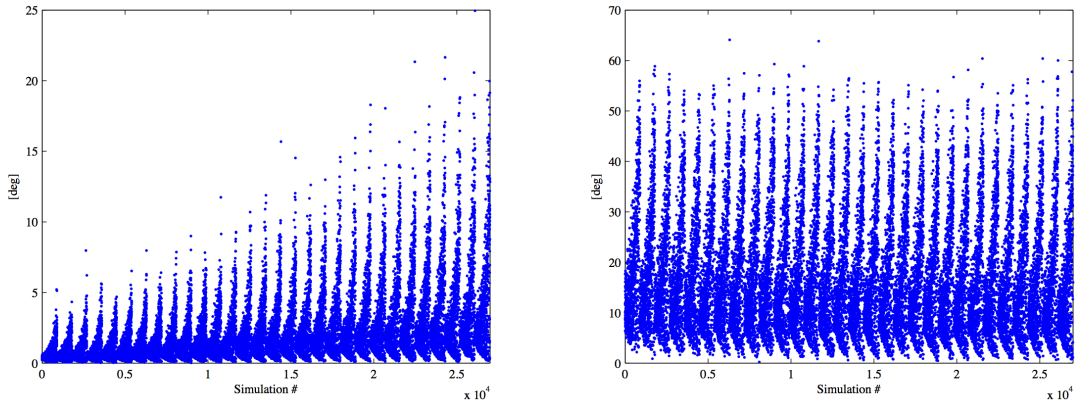


Figure 4.4: The smaller angle between the map of the displacement in the range and either angle-rate for all simulations. Left: propagation time is 0, right: propagation time is 120 hours.

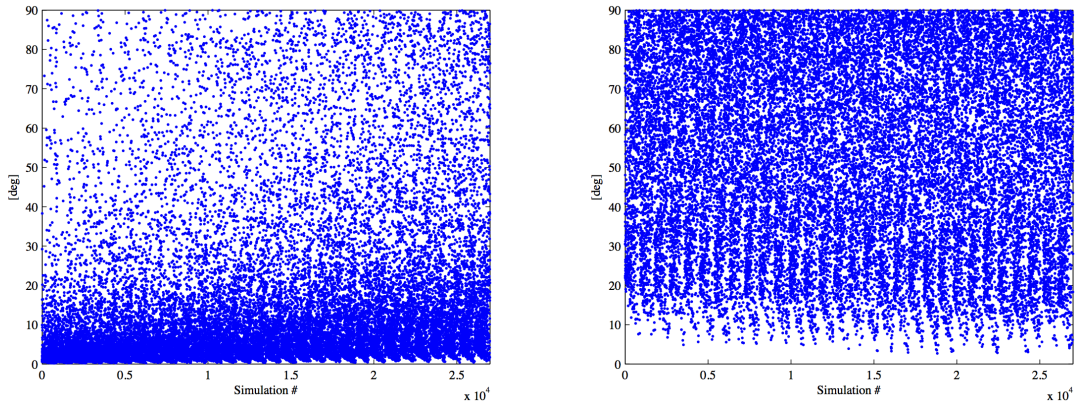


Figure 4.5: The larger angle between the map of the displacement in the range and either angle-rate for all simulations. Left: propagation time is 0, right: propagation time is 120 hours.

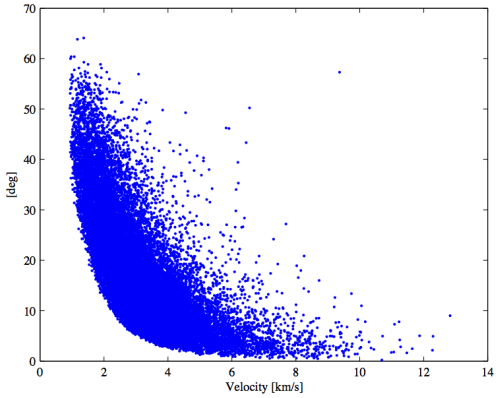


Figure 4.6: Scatter plot of the smaller angle between the map of the displacement in the range and either angle-rate versus the velocity of the observed object. The propagation time is 0.

Conversely, when propagation times are short, the angle-rate errors can displace the AR map in directions perpendicular to the $\rho$ and $\dot{\rho}$ maps, meaning that ignoring these errors may not be justified for fine discretizations of the state space. This phenomenon is most prevalent when the velocity of the observed object is slow ($\sim$ 3 km/s and lower) as can be inferred from Figure 4.6. The reason why the map of the errors in $\rho$ and the angle-rates align is because they both act to change the orbit energy and thus $\mathfrak{Q}$ (equivalent to semi-major axis); the former through the orbit radius and the latter through velocity. When the velocity is low, however, even a small error in the angle-rates can strongly influence not only the orbit energy but also the orbit plane orientation.

## 4.2 Effects of Measurement Errors on The Admissible Region: Space-Based Observations

For space-based observations, the static linear transformation from the attributable vector state space to the Poincaré orbital element space is modified to add the observer's state $(\mathbf{P}_O, \dot{\mathbf{P}}_O)$

$$\Phi_S(t_0) = \left.\frac{\partial(\mathfrak{Q}, \mathfrak{l}, \mathfrak{G}, \mathfrak{g}, \mathfrak{H}, \mathfrak{h})^T}{\partial(a, e, i, \Omega, \omega, M)^T}\right|_* \circ \left.\frac{\partial(a, e, i, \Omega, \omega, M)^T}{\partial(x, y, z, \dot{x}, \dot{y}, \dot{z})^T}\right|_* \circ \left.\frac{\partial(x, y, z, \dot{x}, \dot{y}, \dot{z})^T}{\partial(\alpha, \delta, \dot{\alpha}, \dot{\delta}, \mathbf{P}_O, \dot{\mathbf{P}}_O)^T}\right|_* . \tag{4.4}$$

As with the ground-based case, the complete linear transform adds a dynamic transform from time $t_0$ to $\tau$. Two-body dynamics with secular $J_2$ perturbations is considered for this example: refer to Section 2.3.2 for details.

First, to generate reference orbits, 126 error-free observations are simulated from LEO-O to the objects in the 8 object sample set in Section 3.10 over the span of 120 hours: refer to Appendix B for initial states of all objects. The observations are timed according to the rules in Section 3.10.2. Then, deviations in the attributable vector are sampled on the 3-$\sigma$ error hyperellipsoid whose bounds are the same as the deviations assumed in the previous section: $\sigma_\alpha = \sigma_\delta = 0.54$ arcsec, and $\sigma_{\dot{\alpha}} = \sigma_{\dot{\delta}} = 1.2 \cdot 10^{-3}$ arcsec/sec. In order to reduce the dimensionality of this analysis, perfect knowledge of the observing satellite's velocity is assumed, given that it can usually be determined to the millimeter/second-level [83]. The maximum absolute Poincaré state deviation, computed with (4.4), is recorded for each observation. Figure 4.7 shows the time evolution of these maxima, and Table 4.3 is a tabulated summary. Only the error in $\mathfrak{l}$ grows significantly in time, which is expected as $\mathfrak{l}$ is directly proportional to the mean anomaly. After 120 hours, the state errors are on the same order of magnitude as the discretization for $\mathfrak{l}$, whereas for all other coordinate directions, they remain less than 1/10th of the nominal bin size employed in the examples in Sections 3.9 and 3.10.

Table 4.3: The mean and maximum state errors in each Poincaré orbital element direction, as well as the ratio of their values with respect to the nominal discretization size of 0.081586, for the LEO-O observer.

| | **Mean** | (Ratio) | **Max** | (Ratio) |
|---|---|---|---|---|
| $\mathfrak{L}$ | 0.00363 | 0.04446 | 0.00731 | 0.08955 |
| $\mathfrak{l}$ | 0.02236 | 0.27401 | 0.06075 | 0.74461 |
| $\mathfrak{G}$ | 0.00169 | 0.02075 | 0.00429 | 0.05261 |
| $\mathfrak{g}$ | 0.00164 | 0.02013 | 0.00416 | 0.05102 |
| $\mathfrak{H}$ | 0.00106 | 0.01299 | 0.00251 | 0.03082 |
| $\mathfrak{h}$ | 0.00117 | 0.01439 | 0.00354 | 0.04335 |

Figure 4.8 and Table 4.4 are results of similar analyses run for the GEO-O observation satellite. Here, the error in $\mathfrak{l}$ grows beyond the nominal discretization size at about 80 hours. This is due to a combination of the larger uncertainty in the observing satellite's state and the higher sensitivity to measurement errors compared to the low Earth orbit (LEO) case especially when observation distances are large. On the other hand, the errors in all of the other coordinate directions are the approximately the same as the previous example.

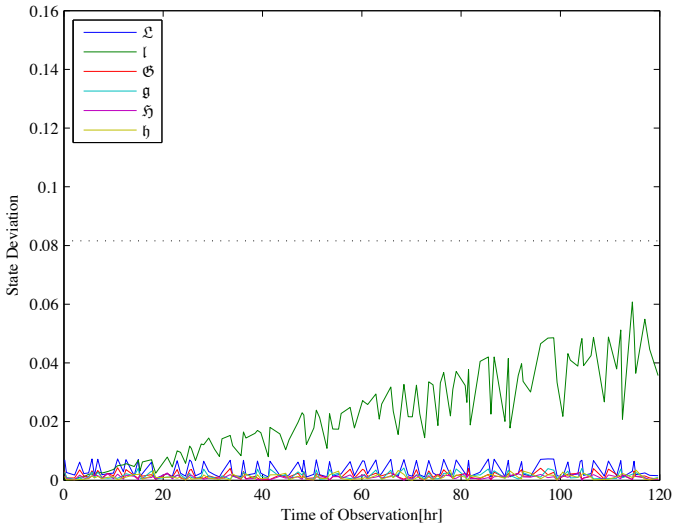


Figure 4.7: Errors in the Poincaré orbital elements due to uncertainty in the attributable vector as a function of time for the LEO-O observer. The black dotted line indicates the nominal discretization size.

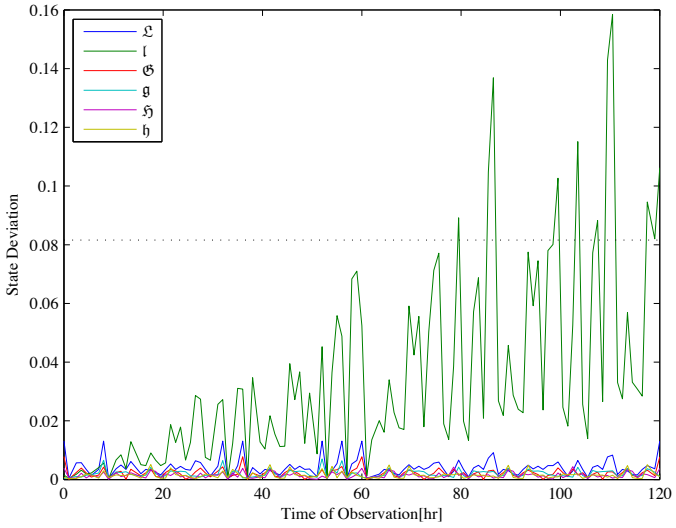


Figure 4.8: Errors in the Poincaré orbital elements due to uncertainty in the attributable vector as a function of time for the GEO-O observer. The black dotted line indicates the nominal discretization size.

Table 4.4: The mean and maximum state errors in each Poincaré orbital element direction, as well as the ratio of their values with respect to the nominal discretization size of 0.081586, for the GEO-O observer.

| | **Mean** | (Ratio) | **Max** | (Ratio) |
|---|---|---|---|---|
| $\mathfrak{L}$ | 0.00417 | 0.05106 | 0.0131 | 0.16059 |
| $\mathfrak{l}$ | 0.03455 | 0.42342 | 0.15845 | 1.94212 |
| $\mathfrak{G}$ | 0.00221 | 0.02714 | 0.00779 | 0.09553 |
| $\mathfrak{g}$ | 0.00205 | 0.02519 | 0.00705 | 0.08636 |
| $\mathfrak{H}$ | 0.00148 | 0.01818 | 0.00437 | 0.05357 |
| $\mathfrak{h}$ | 0.00154 | 0.01884 | 0.0051 | 0.06251 |

## 4.3 Extension of The Planar Mesh Map to Higher Dimensions

Discussed here are methods to account for the effects of observational error as discussed above in tracklet association and initial orbit determination (IOD). For the 2-dimensional AR, subsets of the AR are regarded as planar such that, for a uniform distribution in the range / range-rate direction, the generalized AR (i.e., a probability density function or pdf) is efficiently computed by means of linear extrapolation: refer to Section 3.7.4. Each planar subregion is constructed as the union of line segments between a vertex and its opposing edge. The probability in each discretization bin is then computed by determining how the plane is divided up into the bins it resides in. The AR is expanded to extra dimensions in a similar spirit: a $n$-dimensional AR map is regarded as a union of $(n-1)$-dimensional maps. This process may be repeated recursively until the whole map is sampled by a scan of 1-dimensional line segments. Such an approach could be both feasible and desirable for ground-based observations because, from the analysis Section 4.1, the observational error effectively only adds one extra dimension to the AR map, and thus one extra recursion level, in many realistic observation scenarios.

First, the $\rho$-$\dot{\rho}$ space is sampled and the $2^n$ vertices of a $n$-dimensional subspace about each sample point solved for via the linear transformation (4.3). Since the observational error is well approximated as Gaussian, the limits of the subspace in the directly observed variables may be defined by a $k$-$\sigma$ ($k \in \mathbb{N}$) bound so that the AR remains compact. Consequently, the subspace is a orthotope in topocentric spherical coordinates, which is mapped to a convex polytope in the Poincaré orbital element space. Note that only $\rho$ and $\dot{\rho}$ are sampled over as sampling over the full $n$-dimensional space would become more and more

computationally expensive for larger and larger $n$. Rather, it is useful to first assess which discretization bins the AR spreads across, compute the posterior pdf $h[\mathbf{X}(\tau)]$ with (3.31) assuming a uniform distribution over these bins, and finally evaluate the actual posterior pdf only over the bins where $h > 0$; i.e., a much smaller subset of the ARs.

Let the bins be indexed as a vector $\mathbf{i} = (i_1, \ldots, i_n)$ in each direction of the state space and define $\bar{\mathbf{X}}$ for convenience as in Section 3.7.1. From the sample points, two points are chosen that lie on an edge and the bins it passes through calculated with (3.52). To find the bin indices of the 2-face containing this edge, the indices of the following line segments are computed:

(1) The opposing edge

(2) The 2 line segments connecting the two edges

(3) Line segments parallel to the original edge which pass through points corresponding to all $\kappa_j$ of (2).

Although this approach is robust, it does not guarantee that all bins in which the 2-face resides are accounted for. Undersampling may be mitigated by increasing the line segments considered in 3. The 3-face is similarly found by calculating the bins occupied by the opposing 2-face, the line segments connecting them, and 2-faces parallel to the original. The routine is repeated until all $(n-1)$-faces of the $n$-dimensional subspace are accounted for.

With the direct Bayesian AR approach, the association of observations is inferred from the topology of the ARs which is sufficiently characterized without the numerical values of the pdf. Therefore, the association step is complete if (3.31) is applied to an approximation of the AR with uniform density and compactness defined by the $k$-$\sigma$ observational error bound. Nevertheless, for orbit estimation purposes, the *a posteriori* pdf may be computed and integrated over each bin in its domain. From (2.9), all that is required to determine the value of the AR pdf is an analytical expression of the initial AR. The uncertainty in the attributable vector $\mathfrak{y}$ may be expressed as

$$p(\mathfrak{y}^0) = \frac{1}{\sqrt{(2\pi)^{2n}|[P^0]|}} \exp\left\{\frac{1}{2}(\mathfrak{y}^0 - \boldsymbol{\mu}^0)^T [P^0]^{-1} (\mathfrak{y}^0 - \boldsymbol{\mu}^0)\right\}, \tag{4.5}$$

where $\boldsymbol{\mu}^0$ is the initial mean and $[P^0]$ the initial covariance. Note that $n = 4$ for ground-based and $n = 10$ for space-based observations, but as in Section 4.1, the errors in $\alpha$ and $\delta$ may be ignored for the former, in which case $n = 2$. For the latter, ignoring velocity errors reduces the dimensionality to $n = 7$ as in Section 4.2. Given values for $\rho$ and $\dot{\rho}$, (4.5) fully describes the AR in the subspace corresponding to variables in $\mathfrak{Y}^0$. If a uniform distribution is assumed for $\rho$ and $\dot{\rho}$, it is akin to regarding them as a random draw, allowing us to write the AR pdf as

$$p(\mathbf{X}^0) = \frac{1}{\mathcal{A}\sqrt{(2\pi)^{2n}|[\tilde{P}^0]|}} \exp\left\{\frac{1}{2}(\mathbf{X}^0 - \tilde{\boldsymbol{\mu}}^0)^T[\tilde{P}^0]^{-1}(\mathbf{X}^0 - \tilde{\boldsymbol{\mu}}^0)\right\}, \tag{4.6}$$

where the tilde indicates the parameters of (4.5) mapped to the Poincaré orbital element space, $\mathcal{A}$ is the area of the domain of the AR on the surface corresponding to $\rho$ and $\dot{\rho}$ directions, and $\mathbf{X}^0$ is restricted to the subspace corresponding to variables in $\mathfrak{Y}^0$. At all other points, the AR is 0. Integration over the discretization bins may now be achieved with a cubature, for instance [44]. Alternatively, an analytic expression of the initial pdf may be obtained through a Gaussian mixture model [11].

The theory discussed so far is implemented in MATLAB. Here, two noisy ground-based optical observations of a sub-geosynchronous orbit object are simulated. ARs for both observations are computed with and without the effects of errors and the posterior pdf is solved for each. The Keplerian and Poincaré orbital elements of the observed object at the time of the first observations are

$$(a, e, i, \Omega, \omega, M) = (40000 \text{ km}, 0, 5 \text{ deg}, 17.19 \text{ deg}, 17.19 \text{ deg}, 17.19 \text{ deg}) \tag{4.7}$$

$$(\mathfrak{L}, \mathfrak{l}, \mathfrak{G}, \mathfrak{g}, \mathfrak{H}, \mathfrak{h}) = (11.17, 0.9, 0, 0, -0.08618, 0.2786), \tag{4.8}$$

where the units for the Poincaré elements are in Earth radii - kg - hr. Two-body dynamics is again assumed for simplicity but is not central to our technique.

The two observations are separated by 8 hours. For both, the attributable vector is displaced by 1.35 arcsec in the angles and $9.0 \cdot 10^{-3}$ arcsec/sec in the angle-rates. According to the analysis in Section 4.1, in this scenario, the effects due to errors in right ascension and declination may be ignored but not those due to their rates. The errors in the angle-rates are assumed to be distributed normally with zero-mean with $3.6 \cdot 10^{-3}$ arcsec/sec 1-$\sigma$. The AR domain is constrained by the criteria in Section 3.3 for $\rho$ and $\dot{\rho}$ and the 3-$\sigma$ bounds for $\dot{\alpha}$ and $\dot{\delta}$.

The Poincaré space is discretized such that the bounds of the state space are

$$\mathbf{X}_{\min} = (4.4621, 0, -3, -3, -4, -4) \tag{4.9}$$

$$\mathbf{X}_{\max} = (17.2815, 6.2832, 3, 3, 4, 4). \tag{4.10}$$

The bin size is reduced adaptively over regions where the posterior pdf is non-zero until they reach $3.3624 \cdot 10^{-4}$ ($\mathfrak{L}$), $1.9392 \cdot 10^{-3}$ ($\mathfrak{l}$), $1.8519 \cdot 10^{-3}$ ($\mathfrak{G}$, $\mathfrak{g}$), and $2.4691 \cdot 10^{-3}$ ($\mathfrak{H}$, $\mathfrak{h}$) for a total of $1.3613 \times 10^{22}$ bins over the entire space. This resolution corresponds to approximately 10 km in the semi-major axis direction and 1 degree in the mean anomaly direction. The number of AR sample points in the $\rho$-$\dot{\rho}$ space is similarly increased adaptively until the resolution reaches approximately 750 m in $\rho$ and 1.7 km/h in $\dot{\rho}$.

Table 4.5 is a summary of the results. For each case, the number of bins spanned by the AR of the first (AR 1) and second (AR 2) observations, the Boolean outcome of the association, the number of bins spanned by the posterior pdf (Posterior), and whether the posterior pdf includes the true state of the observed object (Incl. Truth) are listed. When the observational errors are ignored entirely, the two ARs appear to not intersect, resulting in a false negative outcome. Conversely, when the errors are included, the ARs span over a $\sim 20$ % larger region in the state space and they indeed intersect over a region containing the true state of the observed object. In Figure 4.9, the ARs and the posterior pdf is projected on to 2-dimensional spaces defined by the coordinate-momenta pairs. Note that the actual application of Bayes' rule (3.31) is done in the full 6-dimensional space. The domain of the posterior pdf has converged tightly about the true state.

Table 4.5: Results of the association and initial orbit determination based on admissible regions ignoring (w/o Error) and including (w/ Error) effects of observational error.

| | **w/o Error** | **w/ Error** | $\Delta$ [%] |
|---|---|---|---|
| Bins (AR 1) | 144271 | 184010 | +27.54 |
| Bins (AR 2) | 164896 | 201783 | +22.37 |
| Association | FALSE | **TRUE** | – |
| Bins (Posterior) | – | 234 | – |
| Incl. Truth | – | **TRUE** | – |

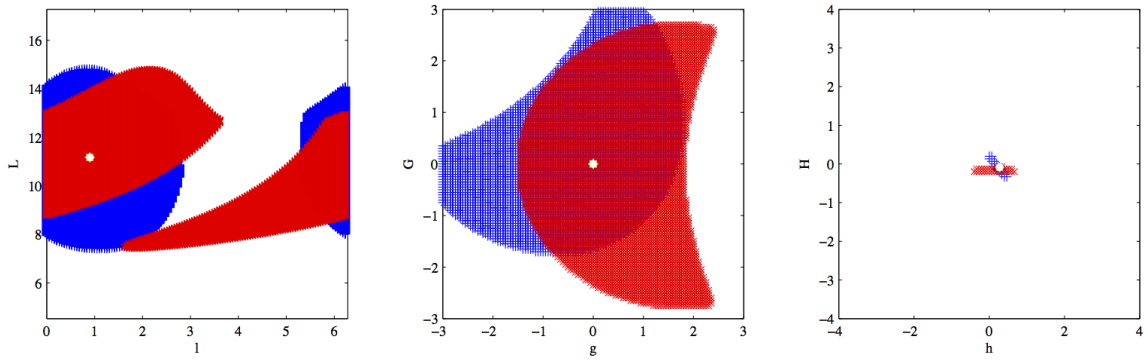


Figure 4.9: Admissible region including effects of observational errors in the Poincaré orbital element space for the first (blue) and second (red) observations. True state (white) lies on top of the posterior pdf (green).

## 4.4 "Direct Bayesian + Least Squares" Hybrid Approach

Although the extension of the two-dimensional linear map extrapolation discussed in the previous section provides the tools to incorporate measurement error completely within the framework of ARs, it proved to be too computationally expensive when processing more than $10^2$ tracklets or when the errors span more dimensions than the angle measurements alone. In this light, a hybrid approach is proposed that takes the observation association and initial orbit determination results of the direct Bayesian method and feeds it into a least squares estimator. Although the steps in this new process are similar to those in a traditional IOD [2], the justification of the association and the estimation are separated, thus improving robustness.

In order to better exclude multi-rev solutions, a minimum limit $p_{\min}$ is set to the $p$-value associated with the model utility test of the observed minus computed $(O - C)$ residuals. Suppose that for $n$ pairs of samples $y_1, \ldots, y_n$ each associated respectively to independent variable $x_1, \ldots, x_n$, the samples are modeled with a simple linear regression model as

$$\hat{y}_i = \hat{\beta}_0 + \hat{\beta}_1 x_i, \tag{4.11}$$

for all integers $1 \leq i \leq n$, where the hat symbolizes that it is a model estimate. Then, for the hypothesis test regarding slope parameter $\beta_1$

$$\begin{cases} H_0 : \beta_1 = 0 \\ H_1 : \beta_1 \neq 0, \end{cases} \tag{4.12}$$

where $H_0$ is the null and $H_1$ the alternative hypothesis, the probability of falsely rejecting $H_0$ is set to be $p_{\min}$. Through this step, a maximum bound is effectively set for $\beta_1$ itself, meaning the residuals must be unrelated to time in a linear sense for an observation pair to be associated to a state estimate. The best estimate for the slope parameter $\hat{\beta}_1$ is

$$\hat{\beta}_1 = \frac{n\sum x_i y_i - (\sum x_i)(\sum y_i)}{n\sum x_i^2 - (\sum x_i)^2}, \tag{4.13}$$

where the summation is from $i = 1$ to $n$ [14]. $\beta_1 = \pm 1$ iff all sample pairs lie on a straight line; thus, although it is not always the case that $\beta_1 = 0$ if the residuals are unrelated to time, since the tracklets arcs are so short, it may be assumed that the residual bias is linear enough for us to use slope parameter $\beta_1$ in this context. The test statistic is Student's $t$-distribution

$$t = \hat{\beta}_1 \sqrt{\frac{n(n-2)}{n\sum y_i^2 - (\sum y_i)^2 + \hat{\beta}_1(\sum x_i)(\sum y_i) - n\hat{\beta}_1 \sum x_i y_i}}. \tag{4.14}$$

As an example of how the linear regression slope parameter can help identify multi-rev solutions, Table 4.6 shows the association result of two observations geometrically correlated as in Section 5.3 to object 98006B in the Joins Space Operations Center (JSpOC) two-line element (TLE) catalog. For the multi-rev solution over the first tracklet, even though the root mean square (RMS) of the residuals in right ascension (RA) are smaller than the expected measurement error of 2 arcsec 1-$\sigma$, the $\beta_1$ value suggests a strong linear relationship between the residuals over time. In addition, the small $p$-value indicates that it is highly unlikely to falsely infer $\beta_1 \neq 0$ due to random chance.

Table 4.6: For two orbit estimates computed based on the hybrid approach, the semi-major axis ($a$), eccentricity ($e$) and inclination ($i$) are listed along with the RMS of the residuals for the first tracklet in RA ($\text{RMS}_{\text{RA}}$) and the linear regression slope parameter ($\beta_{1,\text{RA}}$) with its corresponding $p$-value.

| | $a$ [km] | $e$ | $i$ [deg] | $\text{RMS}_{\text{RA}}$[arcsec] | $\beta_{1,\text{RA}}$ | $p$ |
|---|---|---|---|---|---|---|
| **Solution 1** | 20285 | 0.57013 | 2.2261 | 0.24841 | 0.97512 | 0.00469 |
| **Solution 2** | 42166 | 0.00466 | 0.2886 | 0.05599 | -0.13651 | 0.82673 |

A brief outline of the hybrid algorithm is now presented. A detailed implementation as well as a flowchart is discussed in Section 5.3. First, the direct Bayesian AR algorithm is run as in Section 3.6.3: based on attributable vectors, ARs are computed in the Poincaré orbital element space $\mathbf{X}(t) = (\mathfrak{L}, \mathfrak{l}, \mathfrak{G}, \mathfrak{g}, \mathfrak{H},$

♭). The AR are propagated to a common epoch $\tau$ and associated with Bayes' rule in reverse chronological order. If the posterior pdf $h[\mathbf{X}(\tau)]$ is non-zero, then the centroid of each bin where $h > 0$ is passed to a bank of least squares batch filters. No *a priori* information is necessary; if desired, however, the *a priori* covariance may be set to approximate $h$. For the set of filters that converge, if

(1) the RMS of the $O - C$ residuals over all tracklets processed is less than some maximum $\text{RMS}_{\text{max}}$ AND

(2) the $p$-value of the model utility test for both the right ascension and declination for each individual tracklet is greater than some minimum $p_{\text{min}}$,

then the tracklets are confirmed to be associated and the state estimate with the smallest $O-C$ residual RMS is added to the object catalogue.

## 4.5 Conclusions

In this chapter, a quantitative argument on the effects of measurement errors on the admissible region, and consequently direct Bayesian tracklet association, was given. The errors arising from uncertainty in the attributable vector, along with any dynamical modeling errors, practically limit the state space discretization size. Refining the discretization beyond the level of state error is not recommended as it may lead to false positive / negative association results. For ground-based observations, tracklets of objects moving faster than 8 km/s or slower than 3 km/s are prone to large admissible region mapping errors in the Poincaré orbital element space. For space-based observations, measurements made from an observer in the geosynchronous belt experienced larger errors than those from a low Earth orbit. For both observers, the state space error increased as the propagation time of admissible regions increased. The errors may be accounted for by recursively reducing the dimension of some predesignated error bound until a linear extrapolation in 1 dimension may be applied. For problems with many tracklets or observed variables, however, a hybrid approach that feeds results of the direct Bayesian method to a least squares batch filter is recommended. The simple linear regression slope parameter is proposed as a metric to reduce false positive tracklet associations due to multi-rev solutions. Future work is to improve the discretization in the state space based on rate of

error growth: for example, the least number of bins can be assigned in the $l$-direction, followed by $\mathfrak{L}$, then all other directions.

# Chapter 5

## Applications to Short-Arc Data at The Astronomical Institute at The University of Bern

Thus far, the theoretical framework to accomplish direct Bayesian short-arc association has been laid out. The admissible region (AR) was generalized to be a bounded probability density function (pdf) in some state space whose propagation is described by the Fokker-Planck equations. Several simplifications were introduced to reduce computation time, such as linear extrapolation of AR subsets and special solutions to uncertainty propagation for Hamiltonian and deterministic systems. Association of simulated data as well as simulations on the effects of measurement error showed promise that the direct Bayesian method is indeed applicable to the too-short arc problem.

To this end, in this chapter, the direct Bayesian admissible region concept is applied to actual optical short arcs of Earth-orbiting objects. In particular, the hybrid approach introduced in Section 4.4 is tested on 212 tracklets of geosynchronous (GEO) belt objects taken at the Zimmerwald Observatory of the Astronomical Institute at the University of Bern (AIUB) [68]. Observation capabilities at AIUB, particularly of the ZimSMART telescope, are discussed. The association results are compared against the current orbit determination workflow at AIUB, which consists of conventional geometric tracklet correlation and least squares techniques. The hybrid approach produces 20 association pairs; over half agrees with the AIUB results and two are highly likely to be newly detected. The remaining pairs suggest new association possibilities as well as cast light on the fundamental limits of conducting tracklet association based solely on dynamical and geometrical information.

Figure 5.1: Current setup of ZimSMART [26].

## 5.1 Optical Observation Capabilities And Processing

The Zimmerwald observatory, located about 10km south of Berne, Switzerland, consists of several optical telescopes [18, 25, 26]. One of them, the Zimmerwald SMall Aperture Robotic Telescope (ZimSMART), is best suited for surveying the sky searching for space debris; a photograph is given in Figure 5.1 and its specs are listed in Table 5.1. ZimSMART is used to develop an orbital elements catalogue. Two different orbital regions are surveyed: GEO and medium Earth orbit (MEO). The aim of the surveys of the geostationary ring is maximum coverage of the region around the celestial equator which can be observed from Zimmerwald.

Images taken with ZimSMART are analyzed as follows. First, the right ascension and declination (RA/DEC) of each Resident Space Object (RSO) in the image files are automatically extracted. For each star, which appear streak-like, the center of mass is calculated. RSOs, on the other hand, appear point-like; their centers of mass are calculated as well. As every image has an exposure time, the epoch of the coordinates is chosen to be the mid-exposure time. The RA/DEC of the RSOs are calculated relative to celestial bodies whose physical coordinates are known and cataloged. If the same object is detected on at least 3 images, a *tracklet* will be produced; i.e., a text file containing the observing epoch, position in right

Table 5.1: Instrument specs for the ZimSMART telescope.

| **Spec** | **Value** |
|---|---|
| Lat., Long., Alt. [deg, deg, m] | 46.8772 N, 7.4652 E, 951.2 |
| Cartesian [m] | 4331306.2000, 567553.9900, 4633121.6600 |
| System | WGS-84 |
| Telescope mount | ASA DDM85 |
| Telescope tube | Takahashi $\varepsilon$-180 |
| Aperture diameter | 180 mm |
| Focal length | 500 mm |
| Detector type | CCD |
| Detector size | $4096 \times 4096$ pixel |
| Field of view | $2° \times 2°$ |
| Typical readout time | 7 s |
| Wavelengths | White light |
| Typical exposure time | 10 s |
| Sensitivity | Magnitude 13.5 for 10s exposure time (1m objects in GEO) |

ascension and declination, and apparent magnitude of the object for each image.

After extracting tracklets, one has to identify the observed objects. This process is performed in three steps. First, each tracklet is correlated with the Joint Space Operations Center (JSpOC) two-line element (TLE) catalogue and an internal AIUB catalogue via positions and velocities. The complete procedures are described in detail in [18]. For each observation epoch, ephemerides are computed for each object in the catalogue. A nearest neighbour decision is applied where the deviations of the observations are compared to the ephemerides via the following parameters: arc length error, intrack error, crosstrack error, deviation of the apparent velocity, and angle between the direction of motion. The decision normally is non-ambiguous as, for each tracklet, the nearest neighbor is chosen. Nevertheless, there exist cases where the decision is ambiguous: e.g. when the same object is stored in the catalogue under several names and with elements of different reference epochs.

In the second step, the leftover tracklets are tested pairwise to check if some of them belong to the same object; if so, they are stored as combined tracklets. Tracklets, for which no other fitting tracklet could be found, remain single. This procedure reduces the amount of computations in the following step. Tracklets are combined if the result of a boundary value problem initial orbit determination procedure as outlined in [2] produces residuals below 1.5 arcsec.

Next, the orbital elements of objects in the AIUB internal catalogue are compared with those estimated from the tracklets. This method is especially effective for newly detected objects with observations from only one night. More details are described in [25]. An initial orbit determination (IOD) is conducted pairwise and the resulting orbital elements are compared again to the internal catalogue. The user defines two observations within a tracklet pair and a circular orbit is determined. In this case, the argument of perigee kept at 0°. The user can then decide whether a least-squares orbit improvement is applied. If chosen, an orbit is determined with all six Keplerian elements estimated. If the tracklets span a single night, a simple dynamical model is applied, which includes up to second degree spherical harmonics of the Earth's gravity field and third-body effects of the Sun and solar system planets. With observations from a second night on, a more precise dynamical model is utilized: by default, the Earth's gravitational field up to degree and order 12 is included, but this value can be changed by the user. The scaling factor of the direct radiation

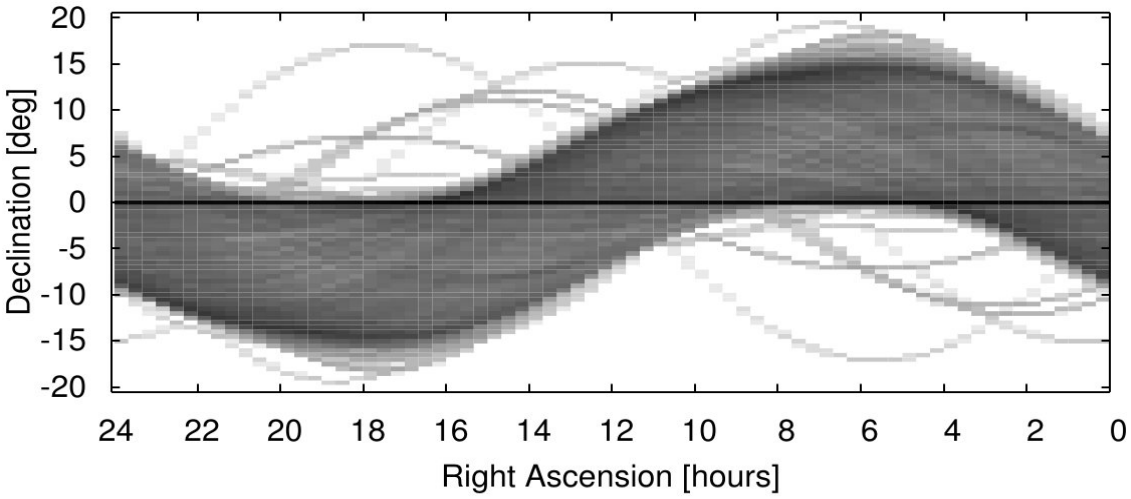


Figure 5.2: Distribution of resident space objects in the geostationary belt with respect to right ascension and declination [25].

pressure can also be estimated. The *a priori* state is set to be the circular orbit IOD results.

As the final step, the identifications via positions and velocities as well as those via orbital elements have to be confirmed by a statistical orbit determination (OD). The new tracklet is associated with an internal catalog object only if the OD is successful; i.e., if the root mean square (RMS) of the residuals of a least squares batch filter is below 1.5 arcsec. Due to the tracklets being *too short arc* and lacking dynamical information, especially when the tracklet pairs span a single night, not every Keplerian element is included in the RMS, but rather only the semi-major axis, inclination, and right ascension of the ascending node.

## 5.2 Observation Strategy

Surveys of the geostationary ring are executed by scanning declination "stripes" with fixed right ascension. These observations are taken without a priori information of any catalogue objects. For the survey from which data processed in this chapter are extracted, 24 stripes are taken separated by 1 hour in right ascension. These stripes are at 0 hr, 1hr, . . . , 23 hr. Each stripe contained five fields separated in declination by the field of view of 2°, and similarly, 5 images are taken for each field. The declination of the lowest field depended on the known RSO population density, as plotted in Figure 5.2. The advantage of this method is that the observations can be acquired in a fully automated fashion with no human interaction;

Table 5.2: Parameters for the data set used in this example. # of objects detected is based on AIUB correlation results.

| Parameter | Value |
|---|---|
| Epoch of Initial Field | Aug 18, 2012 22:59:08.64 UTC |
| Epoch of Final Field | Aug 20, 2012 02:01:32.69 UTC |
| Stripe Right Ascension | 23 hr |
| Total # of Fields | 55 |
| Total # of Tracklets | 212 |
| Total # of Objects Detected | 48 |
| # of Objects Detected Twice w/ 24h Gap | 19 |

the telescope software can choose the visible fields automatically. Again, a tracklet contains a minimum of 3 images and a maximum of 5, corresponding to the number of images taken per field. Depending on the exposure time and the number of images, a tracklet thus spans anywhere between $1 \sim 2$ minutes.

## 5.3 Results

In this section, the outcome of observation association via the direct Bayesian only approach and hybrid approach are compared. Then, the orbits of objects detected by the hybrid approach are examined in further detail. We process a set of tracklets taken with the ZimSMART telescope over one RA stripe; detailed measurement parameters are given in Table 5.2. The admissible regions are defined with the criteria set

$$C = \bigcap_{i=1}^{4} C_i, \tag{5.1}$$

and

$$C_1 = \{(\rho, \dot{\rho}) : E \leq 0\} \qquad C_2 = \{(\rho, \dot{\rho}) : 1.03 \leq \rho \leq 8.53, -5 \leq \dot{\rho} \leq 5\} \tag{5.2}$$

$$C_3 = \{(\rho, \dot{\rho}) : 1.03 \leq r_p\} \qquad C_4 = \{(\rho, \dot{\rho}) : r_a \leq 15\}, \tag{5.3}$$

where $E$ is the specific geocentric energy of the particle, and $r_a$ and $r_p$ are the apoapsis and periapsis radii of the orbit, respectively. Units of are in the Earth radii - kg - hour system. These criteria ensure that the AR encompasses most trackable object relevant to SSA while simultaneously filtering out highly eccentric orbits. They are then divided into 375,000 subsets (750 units of discretization in the range-direction $\times$ 500

units in the range-rate) and each subset linearly extrapolated as explained in Section 3.7.4. The Poincaré space is discretized such that the bounds of the state space are

$$\mathbf{X}_{\min} = (4.5285, 0, -3, -3, -4, -4) \tag{5.4}$$

$$\mathbf{X}_{\max} = (14.110, 6.2832, 3, 3, 4, 4), \tag{5.5}$$

where the units are again in Earth radii - kg - hr. The bin size is set such that the sides are $1.1052 \cdot 10^{-2}$ (♇), $1.7453 \cdot 10^{-2}$ (♅), $1.6667 \cdot 10^{-2}$ (♆, ♃), and $2.2222 \cdot 10^{-2}$ (♄, ♄) for a total of $5.2424 \times 10^{15}$ bins over the entire space. This resolution corresponds to approximately 100 km in the semi-major axis direction and 1 degree in the mean anomaly direction. For the direct Bayesian only case, the discretization is refined dynamically over the support of the posterior pdf to $6.1449 \cdot 10^{-4}$ (♇), $1.7453 \cdot 10^{-2}$ (♅), $3.3333 \cdot 10^{-3}$ (♆, ♃), and $4.4444 \cdot 10^{-3}$ (♄, ♄) for a total of $5.8928 \times 10^{19}$ bins over the entire space; algorithmic details are the same as in Section 3.10.1. The observation error for the least squares batch filter is set to 2 arcsec 1-$\sigma$. The observation-state relationship and corresponding linear partials matrix assumes a spherical Earth

$$x = \rho \cos\alpha \cos\delta \tag{5.6}$$

$$y = \rho \sin\alpha \cos\delta \tag{5.7}$$

$$z = \rho \sin\delta, \tag{5.8}$$

where $x$, $y$, $z$ are in an Earth centered inertial (J2000) coordinate frame. In this example, the solution rejection criteria with respect to the observed minus computed ($O - C$) residuals are $\text{RMS}_{\max} = 0.7$ arcsec for the root mean square and $p_{\min} = 0.1$ for the $p$-value of the model utility test; these values are chosen to best describe the observational capabilities of ZimSMART. Figure 5.3 is a flowchart of the hybrid approach implemented for this chapter.

Table 5.3 is a table of all 20 associated observation pairs detected. The solutions are categorized into three types:

**Type I** The solution is most likely a true solution; associates tracklets that are also similarly correlated with the AIUB code.

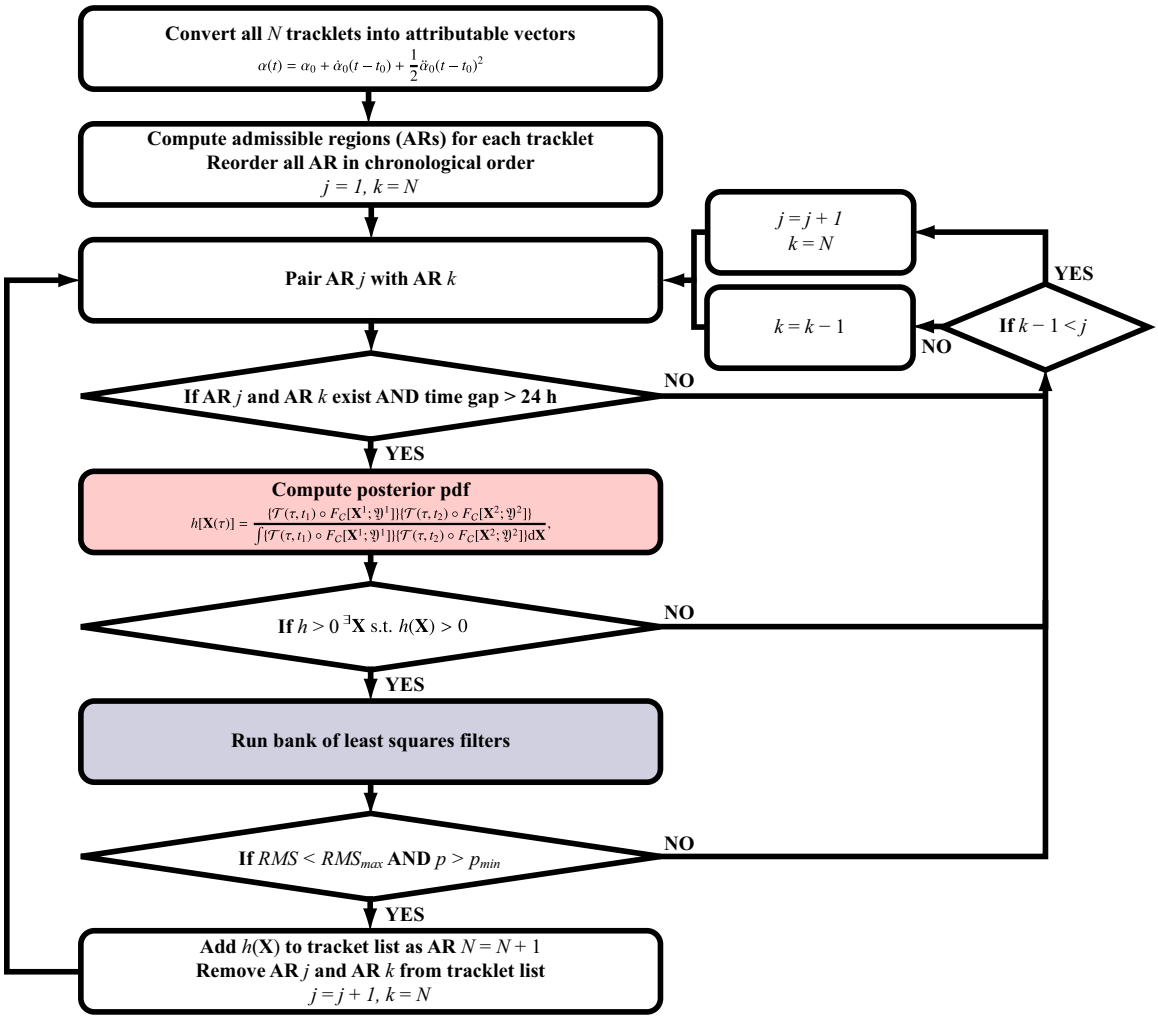


Figure 5.3: A flowchart of the "direct Bayesian + least squares" hybrid approach.

**Type II** The solution is most likely a false positive (multi-rev) solution; associates tracklets that are correlated to two separate objects with the AIUB code AND the solution does not exist at or near (± 200 km) GEO altitude.

**Type III** The solution is most likely a new true solution; at least one of the associated tracklets are not correlated with the AIUB code AND the solution exists at or near (± 200 km) GEO altitude.

Table 5.4 compares the distribution of solution types for the direct Bayesian only and hybrid methods. As expected, for the direct Bayesian only case, over 60% of the solutions found are multi-rev solutions. This ratio improves to 35% for the hybrid case; furthermore, 2 additional "true" solutions are detected. If an object is indeed observed twice or more, the fact that more multi-rev solutions are rejected means that their observations are not "used up" before being properly associated. The Keplerian orbital elements of all solutions obtained with the hybrid method are listed in Appendix D. Based on these results, in a real-world scenario where hundreds of tracklets that contain measurement errors are to be associated, we recommend modifying the direct Bayesian admissible region approach so that it explicitly accounts for such errors as well as reduces multi-rev solutions.

### 5.3.1 Type II Solutions

We now examine in detail the 45% of hybrid method solutions that do not agree with existing techniques. Table 5.5 lists the semi-major axis, eccentricity, and inclination of the Type II solutions. We find that none of the objects are at GEO altitude; in fact, all objects except for Object 6 are in altitudes where it is unlikely for any object to exist. As can be inferred from the strict gating required for an association to be detected ($RMS_{max}$ = 0.7 arcsec), however, these are not non-physical solutions but rather multi-rev solutions that arise from the ambiguity of the number of revolutions made by the observed object during the observation gap. Indeed, if we are to look at the ratio of the time gap between observations to the orbital period of the solution, they are all nearly integers between 1 and 3.

Figures 5.4 and 5.5 are graphical representations of one Type II solution, Object 9, as well as the two catalogued objects to which the AIUB code correlated the corresponding tracklet pair. As expected,

Table 5.3: Summary of association results ordered by solution type. Tracklets correlated to objects in the JSpOC TLE catalog with the AIUB code are indicated by their 6 letter international designator. Tracklets associated with AIUB's least squares method are indicated by a 7 letter internal designator starting with "Z." Tracklets newly associated are indicated by a bracketed number assigned by tracklet epoch. $\delta t$ is the observation time gap.

| Solution Type | Object ID | Observation #1 | Observation #2 | $\delta t$ [days] |
|---|---|---|---|---|
| **Type I** | 2 | '94022A' | '94022A' | 1.01325 |
| | 3 | '93078B' | '93078B' | 1.00508 |
| | 5 | '00081A' | '00081A' | 1.00508 |
| | 11 | '91075A' | '91075A' | 1.00387 |
| | 12 | '02015B' | '02015B' | 1.00172 |
| | 13 | '98006B' | '98006B' | 1.00172 |
| | 14 | '10025A' | '10025A' | 1.00172 |
| | 15 | '08034B' | '08034B' | 1.00172 |
| | 16 | '98057A' | '98057A' | 1.00172 |
| | 17 | '85015B' | '85015B' | 1.01285 |
| | 19 | 'Z11003C' | 'Z11003C' | 1.00932 |
| **Type II** | 4 | '10032B' | '98050A' | 1.00635 |
| | 6 | '98050A' | '09008B' | 1.08071 |
| | 7 | '00054A' | '10025A' | 1.00635 |
| | 9 | '08065B' | '10021A' | 1.01453 |
| | 10 | '11041A' | '98057A' | 1.00603 |
| | 18 | '04008A' | '98024A' | 1.03621 |
| | 20 | '01042A' | 'Z12230G' | 1.00963 |
| **Type III** | 1 | [3] | 'Z12230C' | 1.00635 |
| | 8 | [13] | [120] | 1.00635 |

Table 5.4: Orbit solutions found by type and association method. $\Delta$ is the difference between methods.

| | Type I | Type II | Type III | Total |
|---|---|---|---|---|
| **Direct Bayesian only** | 10 | 18 | 1 | 29 |
| **Hybrid** | 11 | 7 | 2 | 20 |
| **$\Delta$** | +1 | -11 | +1 | -9 |

Table 5.5: For Type II solutions, listed here are the semi-major axis $a$, eccentricity $e$, inclination $i$, and ratio between the observation time gap $\delta t$ and the orbit period $T$.

| Object ID | $a$ [km] | $e$ | $i$ [deg] | $\delta t/T$ |
|---|---|---|---|---|
| 4 | 20370.27 | 0.574014 | 2.36898 | 3.001 |
| 6 | 44103.76 | 0.033165 | 0.15711 | 1.013 |
| 7 | 20367.00 | 0.601097 | 4.21171 | 3.002 |
| 9 | 20489.57 | 0.566496 | 2.53346 | 2.999 |
| 10 | 26695.54 | 0.385897 | 1.64413 | 2.000 |
| 18 | 27240.55 | 0.344950 | 0.95749 | 2.001 |

Object 9 and the catalogued objects align along the observation direction at each tracklet epoch. We find that the slight inclination common to Type II solutions is necessary so that the solution appears at the same declination as an object in the GEO ring.

### 5.3.2 Type III Solutions

Table 5.6 lists the orbital elements of the Type III solutions found and Figure 5.6 is a plot of their groundtracks. Unlike the Type II solutions, both objects are very near circular at geosynchronous altitude, making it likely that they are uncatalogued objects. Here, the long time gap between observations allowed the admissible regions to dynamically evolve so that previously uncorrelated tracks could be linked together.

Table 5.6: For Type III solutions, listed here are all 6 orbital elements: semi-major axis $a$, eccentricity $e$, inclination $i$, right ascension of the ascending node $\Omega$, argument of periapsis $\omega$, and mean anomaly $M$.

| Object ID | $a$ [km] | $e$ | $i$ [deg] | $\Omega$ [deg] | $\omega$ [deg] | $M$ [deg] |
|---|---|---|---|---|---|---|
| 1 | 42167.94 | 0.005040 | 8.74794 | 38.5298 | 38.449 | 264.763 |
| 8 | 42166.74 | 0.000314 | 0.09691 | 56.8309 | 143.201 | 140.752 |

## 5.4 Potential Improvements of The Observation Strategy

The proposed idea of applying a least squares batch filter to the direct Bayesian probabilistic output is effective but nonetheless can still be improved. Table 5.7 sorts the 19 objects expected to be detected

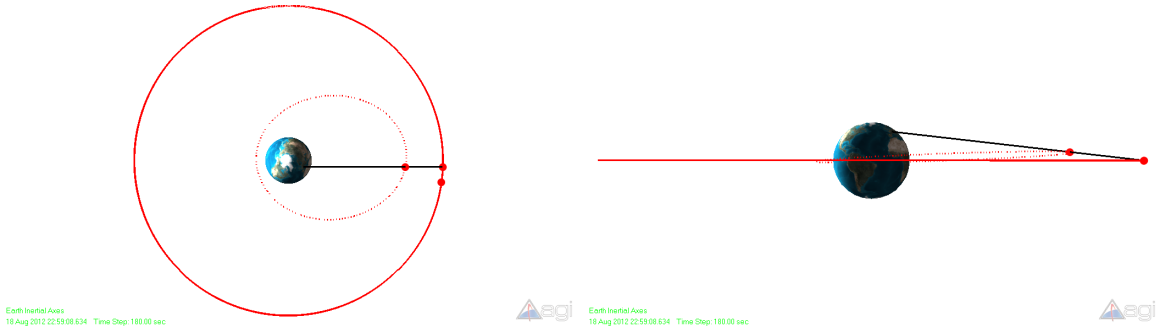

Figure 5.4: The orbit (dotted red line) and position of Object 9 at the first observation epoch along with orbits and positions of catalogued objects 08065B and 10021A (solid red lines) as well as the observation direction (black). Left: view along the $-z$-direction in the J2000 coordinate frame, right: view along the $+y$-direction in the J2000 coordinate frame. Figures generated with AGI's STK.

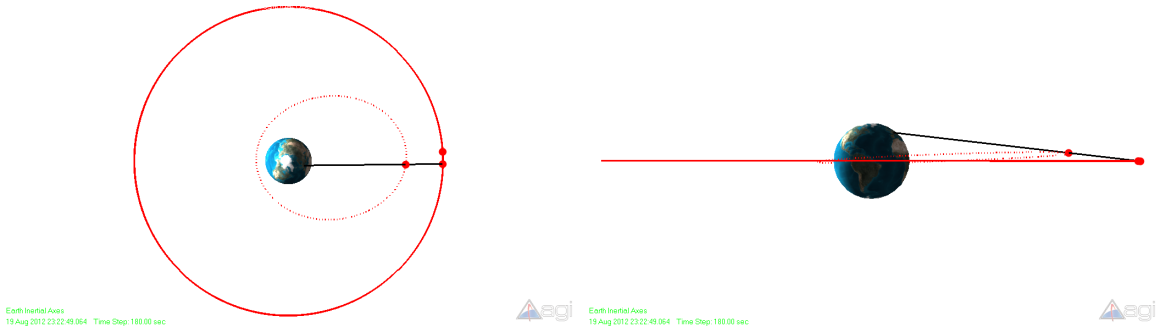

Figure 5.5: Similar to Figure 5.4 but for the second observation epoch. Figures generated with AGI's STK.

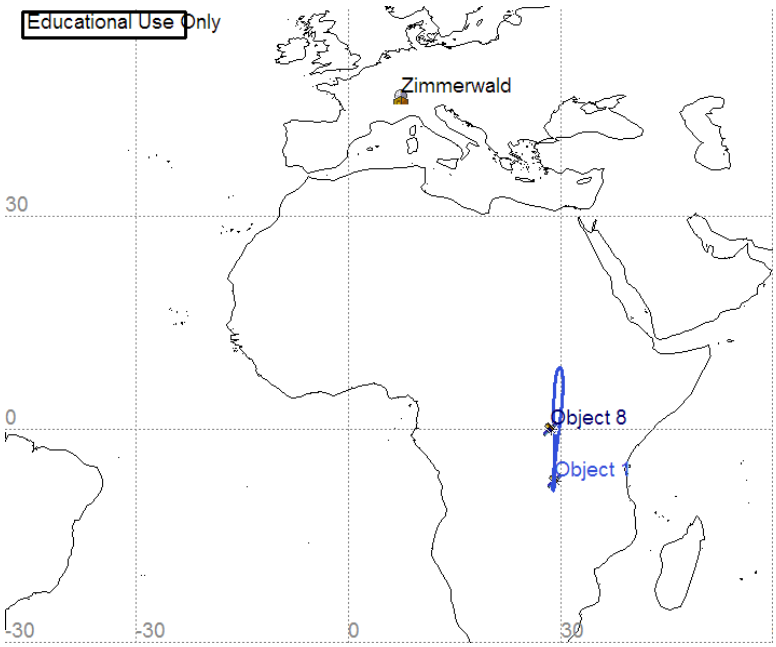


Figure 5.6: Ground tracks of Type III solutions for a full orbit from the observation epoch: Objects 1 (light blue) and 8 (dark blue). The position of each object at the epoch of the first observation is indicated by a satellite logo. The position of the Zimmerwald observatory is also plotted with a dome logo. Figure generated with AGI's STK.

Table 5.7: Objects where multiple tracklets with at least a 24 hour time gap are correlated based on the AIUB algorithm. Tracklets of objects under "Agreement" are associated similarly with the hybrid approach, "multi-rev" associated with another object, and "missed" not associated at all. Number of objects in each category in parenthesis.

| | | |
|---|---|---|
| 00081A | | |
| 02015B | | |
| 08034B | | |
| 10025A | | |
| 85015B | | |
| 91075A | | |
| 93078B | | 82082A |
| 94022A | | 84028A |
| 98006B | 00054A | 93015A |
| 98057A | 11041A | 95067A |
| Z11003C | 98050A | 98056A |
| **Agreement (11)** | **Multi-Rev (3)** | **Missed (5)** |

based on the AIUB correlation results by whether it matches the results from the hybrid method or not. Type II solutions are not completely rejected; consequently, about 15% of the expected objects are missed due to one or more of their observations being associated to a multi-rev solution. Ruling out apparent multi-rev solutions as false associations given just the two tracklets and dynamical system flow may be difficult, especially when the measurement residuals are so well behaved. Note that multi-rev solutions are not a problem in the AIUB code as the observations are seldom associated beyond a single night. This approach is not ideal either: as discussed in Section 3.1, a lack of dynamical information can also lead to poor association solutions. Indeed, new objects within the GEO belt are indeed detected with the hybrid approach where the associated observations are separated by at least 24 hours.

The easiest way to reject multi-rev solutions is to conduct follow-on observations based on the estimated state. If the multi-rev solution is indeed truth, then its short orbital period relative to GEO objects should allow it to be observed multiple times per night. Alternatively, one can make better use of the information already available in the observations. Geometric correlation to objects in the JSpOC TLE catalog as implemented in the current AIUB code is, in effect, one example where *a priori* information is fused into the association process. Preconditioning the ARs with pdfs derived from debris catalogs or density models may

similarly be effective, as in Section 3.9. Information which would allow one to distinguish between tracklets also exists outside of the realm of dynamics, such as photometry and spectroscopy from the charge-coupled device (CCD) image files [69, 70, 72]. Finally, because the evaluation of Bayes' rule when associating ARs is an embarrassingly parallel problem, all-on-all association may be possible within a reasonable time if many computation cores are available.

Additionally, about 25% of the 19 expected objects are completely missed by the hybrid approach. The solution corresponding to object 82082A is rejected due to a particularly large $O - C$ residual value (-2.445 arcsec) in the declination direction for one angle measurement. If this particular measurement were to be excluded, the RMS of the declination residuals improves from 1.0113 arcsec to 0.59865 arcsec. For all of the other solutions, the $p$-value limit for the model utility test of the residuals is triggered, most probably by mistake. Figure 5.7 is one such example: the residuals in the declination direction for the first tracklet is "linear enough" such that $p = 0.0432 < p_{\min} = 0.1$. As such, there exist observation scenarios where reliably evaluating the "no linear relationship" null-hypothesis can be difficult due to the small number of individual angle measurements included in a tracklet. Increasing measurements per tracklet not only will shed better light on any biases present in the residuals but also has the added benefit of improving the angle-rate estimate in the attributable vector.

Because the theory discussed above addresses the too-short arc (TSA) problem in a much more probabilistically straightforward way than other IOD techniques, it allows one to reevaluate future observational strategies so that they minimize false positive / negative association solutions. Any changes to the current strategy, such as the time gap between tracklets, directly affects the *a posteriori* pdf in the state space without the need to assume an observation geometry, dynamical system, or type of errors accounted for. Furthermore, it is not necessary to parametrically account for multi-rev solutions, which explained all false positive solutions encountered in this example; rather, they naturally appear in the *a posteriori* pdf as long as they are dynamically viable.

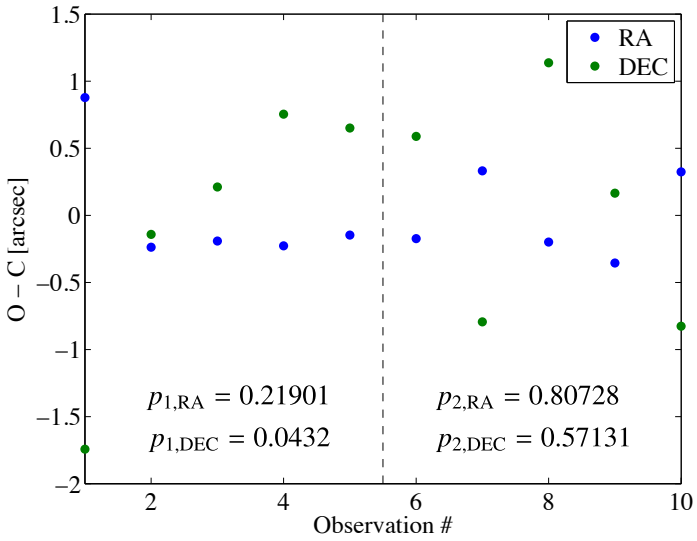


Figure 5.7: History of RA/DEC $O - C$ residuals using the hybrid method for two tracklets correlated to object 84028A with current AIUB code. Plot points to the left of the dotted line are for the first tracklet and to the right the second. $p$-values for the model utility test are indicated per tracklet and angle.

## 5.5 Conclusions

In this chapter, the direct Bayesian admissible region approach to short-arc association and initial orbit determination was applied to optical observations taken at the Astronomical Institute of the University of Bern. Traditional methods rely on the quality of the orbit determination to conduct observation association, which is often unreliable. The direct Bayesian approach improves robustness by leveraging the sparseness of probability distributions that describe range and range-rate ambiguity given a single optical track. Furthermore, a hybrid approach that appends a least squares batch filter is found to efficiently incorporate measurement error and reduce false positives due to multi-rev solutions. Processing a set of 212 tracklets taken at the Zimmerwald Observatory of the Astronomical Institute of the University of Bern results in 20 objects detected; 2 of which are newly detected by the proposed method. Although the hybrid approach cuts the number of false positive solutions by more than half compared to direct Bayesian only, about 35% of the solutions are still deemed to be false positive solutions, and thus ideas to further reject multi-rev solutions are proposed. Future work is to implement these ideas, such as increasing the number of angle measurements per tracklet, as well as further testing of the hybrid approach with more data sets.

# Chapter 6

## Conclusions and Future Work

As more and more sensing capabilities are introduced to the task of space surveillance, we expect that both correlated and uncorrelated tracks of resident space objects will drastically increase. Existing optical observation association techniques rely on simplified dynamics, *ad hoc* criteria for association, and linear propagation of Gaussian uncertainty. To maintain an accurate catalog of resident space objects now and into the future, however, a more consistent description the uncertainty associated with said objects is desired. Two characteristics of the space situational awareness problem are applicable to this goal: that the type of observation significantly influences the geometry of the observational uncertainty, and that the dynamical system is amenable to analytic or semi-analytic solution techniques. In this dissertation, each of these characteristics are examined and ultimately applied to the problem of optical track association, often referred to as the too-short arc problem.

In Chapter 2, an analytical method of non-linear uncertainty propagation including non-conservative effects was discussed. A special solution to the Fokker-Planck equations for deterministic systems and the state transition tensor concept are combined so that, given an analytical expression of both the initial probability distribution and the dynamics, the probability distribution may be expressed analytically for all time. Propagation of uncertainty is then only a matter of changing the time parameter. In particular, two-body dynamics, two-body dynamics plus secular effects of the oblateness of the Earth, and King-Hele's theory on orbital motion influenced by atmospheric drag are applied to the above framework. Examples demonstrate the potential efficiency and accuracy of analytical uncertainty propagation even when compared to numerical results employing a realistic model of dynamical system parameters.

In Chapter 3, an observation association technique which involve probability density functions representing not only measurement errors but also the limited knowledge in the unobserved variables was proposed. The functions, referred to as admissible regions, are bounded by a set of physical constraints. Bayes' rule is directly applied to associate multiple observations and subsequently obtain an orbit estimate. Because the admissible region maps are 2-dimensional manifolds when perfect measurements are assumed, we conclude from topological arguments that they do not intersect generically. A method of linearly extrapolating sub-regions of the admissible region to the discretized Poincaré space is shown to improve computational turn-around without significant loss of map accuracy. Two limiting cases are examined: one where orbit estimation accuracy is compromised if the time between observations is short, and another where false correlations may occur if objects in a satellite constellation are observed. The direct Bayesian admissible region method is applied to both ground- and space-based simulated observations; performance is good in both cases. Based on these results, we find that, for geostationary-on-geostationary observations, efforts to introduce dynamical change are beneficial from the standpoint of initial orbit determination.

In Chapter 4, a quantitative argument on the effects of measurement errors on the admissible region, and consequently direct Bayesian tracklet association, was given. The errors arising from uncertainty in the measurements and measurement parameters, along with any dynamical modeling errors, practically limit the state space discretization size. The errors may be accounted for by recursively reducing the dimension of some predesignated error bound until a linear extrapolation in 1 dimension may be applied. For problems with many tracklets or observed variables, however, a hybrid approach that feeds results of the direct Bayesian method to a least squares batch filter is recommended. The simple linear regression slope parameter is proposed as a metric to reduce false positive tracklet associations due to multi-rev solutions.

In Chapter 5, the direct Bayesian admissible region approach to short-arc association and initial orbit determination was applied to optical observations taken at the Astronomical Institute of the University of Bern. The hybrid approach is found to increase robustness in tracklet association, efficiently incorporate measurement error, and reduce false positives due to multi-rev solutions compared to direct Bayesian alone. Processing a set of 212 tracklets results in 20 objects detected; 2 of which are newly detected by the proposed method. Although the hybrid approach cuts by more than half the number of false positive solutions

compared to direct Bayesian only, some solutions are still deemed to be false positive solutions, and thus ideas to further reject multi-rev solutions are proposed.

Future work is to further incorporate additional perturbations relevant to Earth-orbiting objects to the uncertainty propagation, such as the full effect due to the oblateness of the Earth. Nonetheless, since it is impossible to account for all forces acting on a resident space object, the effects of dynamic modeling errors to the admissible region maps should also be studied. Another way to improve association accuracy is by better implementing the direct Bayesian admissible region technique. For example, the discretization in the state space can be defined based on error growth: the least number of bins should be assigned in the $\dot{l}$-direction, followed by $\Omega$, then all other directions. Similarly, increasing the number of angle measurements per tracklet will shed better light on any biases present in the residuals; it also has the added benefit of improving the angle-rate estimate in the attributable vector. As these ideas are studied, their effect should be ascertained not only through simulations but also by conducting further tests with real world data sets whenever possible.

## Bibliography


[1] Satellite situation report. Report, HQ AFSPC/XOCS. Retrieved from `http://www.space-track.org/` on August 10, 2009.

[2] G. Beutler. Methods of Celestial Mechanics Volume I: Physical, Mathematics, and Numerical Principles. Astronomy and Astrophysics Library. Springer-Verlag, Berlin, Germany, 2005.

[3] D. Brouwer and G. M. Clemence. Methods of Celestial Mechanics. Academic Press, New York, NY, 1961.

[4] J. S. Carter. How Surfaces Intersect in Space: An introduction to topology. World Scientific, Singapore, second edition, 1995. pp. 277.

[5] Committee for the Assessment of NASA's Orbital Debris Programs. Limiting future collision risk to spacecraft: An assessment of NASA's meteoroid and orbital debris programs. Technical report, National Research Council, 2011.

[6] J. L. Crassidis and J. L. Junkins. Optimal Estimation of Dynamic Systems. Chapman & Hall/CRC, Boca Raton, FL, 2004. pp. 681-707.

[7] S. Curtis. The magnetospheric multiscale mission ... resolving fundamental processes in space plasmas. Technical report, NASA Goddard Space Flight Center, 1999. NASA/TM-2000-209883.

[8] D. A. Danielson, B. Neta, and L. W. Early. Semianalytic satellite theory (SST): Mathematical algorithms. Technical report, Naval Postgraduate School, 1994.

[9] F. Delhaise. Analytical treatment of air drag and earth oblateness effects upon an artificial satellite. Celestial Mechanics and Dynamical Astronomy, 52:85 – 103, 1991.

[10] K. J. DeMars. Nonlinear Orbit Uncertainty Prediction and Rectification for Space Situational Awareness. PhD thesis, Faculty of the Graduate School of The University of Texas at Austin, 2010.

[11] K. J. DeMars and M. K. Jah. Initial orbit determination via gaussian mixture approximation of the admissible region. 2012. Presented at the AAS/AIAA Spaceflight Mechanics Meeting, Charleston, SC, AAS 12-260.

[12] K. J. DeMars, M. K. Jah, and P. W. Schumacher. The use of short-arc angle and angle rate data for deep-space initial orbit determination and track association. 2009. Presented at the Eighth US/Russian Space Surveillance Workshop, Wailea-Maui, HI.

[13] A. P. Dempster, N. M. Laird, and D. B. Rubin. Maximum likelihood from incomplete data via the EM algorithm. Journal of the Royal Statistical Society. Series B (Methodological), 39(1):1–38, 1977.

[14] J. L. Devore. Probability and Statistics for Engineering and the Sciences. Wadsworth Publishing Company, Belmont, CA, USA, 4th edition, 1995.

[15] D. Farnocchia, G. Tommei, A. Milani, and A. Rossi. Innovative methods of correlation and orbit determination for space debris. Celestial Mechianics and Dynamical Astronomy, 107(1-2):169–185, 2010.

[16] T. Flohrer, H. Krag, H. Klinrad, and T. Schildknecht. Feasibility of performing space surveillance tasks with a proposed space-based optical architecture. Advances in Space Research, 47:1029–1042, 2011.

[17] C. Früh, T. Schildknecht, R. Musci, and M. Ploner. Catalogue correlation of space debris objects. In 5th European Conference on Space Debris, 2009.

[18] C. Früh, T. Schildknecht, R. Musci, and M. Ploner. Catalogue correlation of space debris objects. 2009. Presented at the Fifth European Conference on Space Debris, Darmstadt, Germany.

[19] K. Fujimoto, J. M. Maruskin, and D. J. Scheeres. Circular and zero-inclination solutions for optical observations of earth-orbiting objects. Celestial Mechanics and Dynamical Astronomy, 106(2):157–182, 2010.

[20] K. Fujimoto and D. J. Scheeres. Correlation of optical observations of earth-orbiting objects and initial orbit determination. Journal of Guidance, Control, and Dynamics, 35(1):208–221, 2012.

[21] S. M. Gadaleta, J. T. Horwood, and A. B. Poore. Short arc gating in multiple hypothesis tracking for space surveillance. 2012. Proc. SPIE 8385, 83850Y.

[22] D. Giza, P. Singla, and M. Jah. An approach for nonlinear uncertainty propagation: Application to orbital mechanics. 2009. Presented at the 2009 AIAA Guidance, Navigation, and Control Conference, Chicago, IL. AIAA 2009-6082.

[23] F. Gustafsson, F. Gunnarsson, N. Bergman, U. Forssell, J. Jansson, R. Karlsson, and P. Nordlund. Particle filters for positioning, navigation, and tracking. IEEE Transactions on Signal Processing, 50(2):425 – 437, 2002.

[24] J. Hackett. Sapphire-like payload for space situational awareness. 2012. Presented at the Advanced Maui Optical and Space Surveillance Technologies Conference, Wailea-Maui, HI.

[25] J. Herzog, C. Früh, and T. Schildknecht. Build-up and maintenance of a catalogue of GEO objects with ZimSMART and ZimSMART 2. 2010. Presented at the 61st International Astronautical Congress, Prague, Czech Republic. IAC-10.A6.5.2.

[26] J. Herzog, T. Schildknecht, and M. Ploner. Space debris observations with ZimSMART. 2011. Presented at the European Space Surveillance Conference, Madrid, Spain.

[27] K. Hill, K. T. Alfriend, and C. Sabol. Covariance-based uncorrelated track association. 2008. Presented at the 2008 AIAA/AAS Astrodynamics Specialist Conference, Honolulu, HI. AIAA 2008-7211.

[28] K. Hill and B. A. Jones. Turboprop version 4.0. Technical report, Colorado Center for Astrodynamics Research, 2009.

[29] M. Holzinger. Optimal Control Applications in Space Situational Awareness. PhD thesis, Graduate School of the University of Colorado, 2011.

[30] C. Hongzheng, S. Xiucong, H. Chao, and T. Geshi. Optimization of hybrid orbit constellation design for space-based surveillance system. 2012. Presented at the AAS/AIAA Spaceflight Mechanics Meeting, Charleston, SC. AAS 12-146.

[31] F. R. Hoots. Theory of the motion of an artificial earth satellite. Celestial Mechanics, 23:307 – 363, 1981.

[32] F. R. Hoots and R. G. France. An analytic satellite theory using gravity and a dynamic atmosphere. Celestial Mechanics, 40:1 – 18, 1987.

[33] J. Horwood, N. D. Aragon, and A. B. Poore. Edgeworth filters for space surveillance tracking. 2010. Presented at the 2010 Advanced Maui Optical and Space Surveillance Technologies Conference, Wailea-Maui, HI.

[34] J. Horwood, N. D. Aragon, and A. B. Poore. Estimation of drag and its uncertainty in initial orbit determination using gauss-hermite quadrature. 2010. Presented at the AAS Born Symposium, Boulder, CO.

[35] J. Horwood, N. D. Aragon, and A. B. Poore. Gaussian sum filters for space surveillance: Theory and simulations. Journal of Guidance, Control, and Dynamics, 34(6):1839 – 1851, 2011.

[36] B. Jia, M. Xin, and Y. Cheng. Salient point quadrature nonlinear filtering. In Proceedings of the 2011 American Control Conference, 2011.

[37] B. J. Jones, A. Doostan, and G. H. Born. Nonlinear propagation of orbit uncertainty using non-intrusive polynomial chaos. Journal of Guidance, Control, and Dynamics, 2012. (Accepted).

[38] J. Junkins, M. Akella, and K. T. Alfriend. Non-gaussian error propagation in orbit mechanics. Journal of the Astronautical Sciences, 44(4):541–563, 1996.

[39] J. Junkins and P. Singla. How nonlinear is it? A tutorial on nonlinearity of orbit and attitude dynamics. Journal of the Astronautical Sciences, 52(1,2):7–60, 2004.

[40] D. King-Hele. Theory of Satellite Orbits in an Atmosphere. Butterworths, London, Great Britain, 1964. pp. 40-77.

[41] J. Li, L. Lin, W. An, and Y. Zhou. A constrained iterative searching algorithm for space object passive tracking using single space-based optical sensor. 2008. Presented at the IEEE International Conference on Information and Automation, Zhangjiajie, China.

[42] J. D. Lowe, D. A. Vallado, and B. Hall. Technical analysis of commercially hosted optical payloads for enhanced SSA. 2010. Presented at the Advanced Maui Optical and Space Surveillance Technologies Conference, Wailea-Maui, HI.

[43] R. H. Lyddane. Small eccentricities or inclinations in the brouwer theory of the artificial satellite. The Astronomical Journal, 68(8), 1963.

[44] J. N. Lyness and B. J. J. McHugh. Integration over multidimensional hypercubes I. a progressive procedure. The Computer Journal, 6(3):264–270, 1963.

[45] M. Majji, J. L. Junkins, and J. D. Turner. A high order method for estimation of dynamic systems. Journal of the Astronautical Sciences, 56(3):401–440, 2008.

[46] J. M. Maruskin, D. J. Scheeres, and K. T. Alfriend. Correlation of optical observations of objects in earth orbit. Journal of Guidance, Control and Dynamics, 32(1):194–209, 2009.

[47] P. S. Maybeck. Stochastic Models, Estimation and Control, volume 2. Academic Press, New York, NY, 1982. pp. 159-271.

[48] P. McCullaugh. Tensor Methods in Statistics. Chapman and Hall, London, 1987. pp. 24-56.

[49] J. W. McMahon and D. J. Scheeres. New solar radiation pressure force model for navigation. Journal of Guidance, Control, and Dynamics, 33(5):1418 – 1428, 2010.

[50] A. Milani, G. Gronchi, M. Vitturi, and Z. Knežević. Orbit determination with very short arcs. i admissible regions. Celestial Mechanics and Dynamical Astronomy, 90:57–85, 2004.

[51] A. Milani and Z. Knežević. From astrometry to celestial mechanics: orbit determination with very short arcs. Celestial Mechanics and Dynamical Astronomy, 92:118, 2005.

[52] O. Montenbruck and E. Gill. Satellite Orbits: Models Methods Applications. Springer-Verlag, New York, 2000. pp. 233.

[53] M. M. Morton and T. Roberts. Joint space operations center (JSpOC) mission system (JMS). 2011. Presented at the Advanced Maui Optical and Space Surveillance Technologies Conference, Wailea-Maui, HI.

[54] NASA Orbital Debris Program Office. Orbital debris quarterly news. 17(1), 2013.

[55] M. Oswald, S. Stabroth, C. Wiedemann, P. Wegener, H. Klinkrad, and P. Vörsmann. ESA's MASTER 2005 debris environment model. Advances in the Astronautical Sciences, 123(1):811–824, 2006.

[56] R. S. Park and D. J. Scheeres. Nonlinear mapping of gaussian statistics: Theory and applications to spacecraft trajectory design. Journal of Guidance, Control and Dynamics, 29(6):1367–1375, 2006.

[57] R. S. Park and D. J. Scheeres. Nonlinear semi-analytic methods for trajectory estimation. 30(6):1668–1676, 2007.

[58] A. D. Parks. A drag-augmented brouwer-lyddane artificial satellite theory and its application to long-term station alert predictions. Technical report, Naval Surface Weapons Center, 1983. NSWC TR 83-107.

[59] J. M. Picone, A. E. Hedin, D. P. Drob, and A. C. Aikin. NRLMSISE-00 empirical model of the atmosphere: Statistical comparisons and scientific issues. Journal of Geophysical Research, 107(A12):1468, 2002.

[60] F. P. Preparata and M. I. Shamos. Computational Geometry: An introduction. Springer-Verlag, New York, NY, 1985. pp. 287.

[61] S. J. Press. Subjective and Objective Bayesian Statistics: Principles, Models, and Applications. John Wiley & Sons, Inc., Hoboken, NJ, second edition, 2003.

[62] D. R. Reid. An algorithm for tracking multiple targets. IEEE Transactions on Automatic Control, AC-24(6):843–854, 1979.

[63] A. Rosengren and D. Scheeres. Long-term dynamics of HAMR objects in HEO. 2012. Presented at the AIAA/AAS Astrodynamics Specialist Conference, Minneapolis, Minnesota, AIAA 2012-4745.

[64] A. Rossi. The earth orbiting space debris. Serb. Astron. J., (170):1–12, 2005.

[65] A. Schaeperkoetter and D. Mortari. A comprehensive comparison between angles-only initial orbit determination techniques. 2011. Presented at the AAS/AIAA Spaceflight Mechanics Meeting, New Orleans, LA. AAS 11-116.

[66] D. J. Scheeres, D. Han, and Y. Hou. Influence of unstable manifolds on orbit uncertainty. Journal of Guidance, Control, and Dynamics, 24:573–585, 2001.

[67] D. J. Scheeres, F.-Y. Hsiao, R. Park, B. Villac, and J. M. Maruskin. Fundamental limits on spacecraft orbit uncertainty and distribution propagation. Journal of Astronautical Sciences, 54(3-4):505–523, 2006.

[68] T. Schildknecht, W. Flury, C. Früh, J. Herzog, A. Hinze, and A. Vananti. Using optical observations to survey, track, and characterize small-size objects at high altitudes. 2011. Presented at the 28th International Symposium on Space Technology and Science, Okinawa, Japan, 2011-r-07.

[69] T. Schildknecht, C. Früh, J. Herzog, A. Hinze, and A. Vananti. AIUB efforts to survey, track, and characterize small-size objects at high altitudes. 2010. Presented at the Advanced Maui Optical and Space Surveillance Technologies Conference, Wailea-Maui, HI.

[70] T. Schildknecht, A. Vananti, H. Krag, and C. Erd. Reflectance spectra of space debris in GEO. 2009. Presented at the Advanced Maui Optical and Space Surveillance Technologies Conference, Wailea-Maui, HI.

[71] J. Schmidt and T. A. Lovell. Estimating geometric aspects of relative satellite motion using angles-only measurements. 2008. Presented at the AIAA/AAS Astrodynamics Specialist Conference, Honolulu, HI. AIAA-2008-6604.

[72] R. L. Scott and B. Wallace. Small-aperture optical photometry of Canadian geostationary satellites. Can. Aeronaut. Space J., 55(2):41–53, 2009.

[73] S. Šegan. Analytical computation of atmospheric effects. Celestial Mechanics, 41:381 – 388, 1988.

[74] J. Sharma, G. H. Stokes, C. von Braun, G. Zollinger, and A. J. Wiseman. Toward operational space-based space surveillance. Lincoln Laboratory Journal, 13(2):309–334, 2002.

[75] J. R. Shell. Commercially-hosted payloads for debris monitoring and mission assurance in GEO. 2011. Presented at the Advanced Maui Optical and Space Surveillance Technologies Conference, Wailea-Maui, HI.

[76] M. Šimandl, J. Královec, and T. Söderström. Advanced point-mass method for nonlinear state estimation. Automatica, 42:1133 – 1145, 2006.

[77] G. H. Stokes, C. von Braun, R. Srid haran, D. Harrison, and J. Sharma. The space-based visible program. Lincoln Laboratory Journal, 11(2):205–238, 1998.

[78] M. Tagawa, T. Hanada, Y. Kitazawa, and A. Kawabe. Orbital debris observation using space-based ladar system. 2011. Presented at the 28th International Symposium on Space Technology and Science, Okinawa, Japan.

[79] B. D. Tapley, B. E. Schutz, and G. H. Born. Statistical Orbit Determination. Elsevier Academic Press, Burlington, MA, 2004. pp. 159-284.

[80] The Boeing Company. Space based space surveillance (SBSS) system. Memorandum, 2011.

[81] J. Tombasco. Orbit Estimation of Geosynchronous Objects Via Ground-Based and Space-Based Optical Tracking. PhD thesis, Graduate School of the University of Colorado, 2011.

[82] G. Tommei, A. Milani, and A. Rossi. Orbit determination of space debris: admissible regions. Celestial Mechanics and Dynamical Astronomy, 97:289–304, 2007.

[83] D. Vallado. Fundamentals of Astrodyamics and Applications. Microcosm Press, Hawthorne, CA, third edition, 2007.

[84] D. Vallado. Fundamentals of Astrodyamics and Applications. Microcosm Press, Hawthorne, CA, third edition, 2007. pp. 119.

[85] D. Vallado. Simulating space surveillance networks. 2011. Presented at the 2011 AAS/AIAA Astrodynamics Specialist Conference, Girdwood, AK. AAS 11-580.

[86] D. Vallado, J. Lowe, and J. Anderson. Benefits of hosted payload architectures for improved GEO SSA. 2011. Presented at the Advanced Maui Optical and Space Surveillance Technologies Conference, Wailea-Maui, HI.

[87] D. A. Vallado. Evaluating gooding angles-only orbit determination of space based space surveillance measurements. 2010. Presented at the AAS Born Symposium, Boulder, CO.

[88] C. Wiedemann, S. Flegel, J. Gelhaus, M. Möckel, H. Klinkrad, H. Krag, and P. Vörsmann. The space debris environment model MASTER-2009. 2011. Presented at the 28th International Symposium on Space Technology and Science, Okinawa, Japan.

[89] D. C. Woffinden and D. K. Geller. Observability criteria for angles-only navigation. IEEE Transactions on Aerospace and Electronic Systems, 45(3):1194 – 1208, 2008.

## Appendix A

## Derivation of State Transition Matrices For Two-Body Motion With Averaged $J_2$ Effects in The Poincaré Orbital Elements

Let $\Phi_P = (\partial\,^P\mathbf{X}(t)/\partial\,^P\mathbf{X}^0)$, $\Phi_D = (\partial\,^D\mathbf{X}(t)/\partial\,^D\mathbf{X}^0)$, $J_{PD} = \{\partial\,^P\mathbf{X}(t)/\partial\,^D\mathbf{X}(t)\}$, $J_{DP,0} = (\partial\,^D\mathbf{X}^0/\partial\,^P\mathbf{X}^0)$. Then,

$$\Phi_P = J_{PD} \circ \Phi_D \circ J_{DP,0}. \tag{A.1}$$

$\Phi_D$ has no singularities

$$\Phi_D(1,1) = \Phi_D(2,2) = \Phi_D(3,3) = \Phi_D(4,4) = \Phi_D(5,5) = \Phi_D(6,6) = 1 \tag{A.2}$$

$$\Phi_D(2,1) = \left[-\frac{3\mu^2}{L^4} + J_2\left(\frac{3\mu^4 {r_E}^2}{L^8}\right)\left(\frac{L}{G}\right)^3\left(1 - 3\frac{H^2}{G^2}\right)\right]t \tag{A.3}$$

$$\Phi_D(2,3) = \Phi_D(4,1) = J_2\left(\frac{9\mu^4 {r_E}^2}{4L^8}\right)\left(\frac{L}{G}\right)^4\left(1 - 5\frac{H^2}{G^2}\right)t \tag{A.4}$$

$$\Phi_D(2,5) = J_2\left(\frac{9\mu^4 {r_E}^2}{2L^8}\right)\left(\frac{L}{G}\right)^4\left(\frac{H}{G}\right)t \tag{A.5}$$

$$\Phi_D(4,3) = J_2\left(\frac{3\mu^4 {r_E}^2}{2L^8}\right)\left(\frac{L}{G}\right)^5\left(2 - 15\frac{H^2}{G^2}\right)t \tag{A.6}$$

$$\Phi_D(4,5) = \Phi_D(6,3) = J_2\left(\frac{15\mu^4 {r_E}^2}{2L^8}\right)\left(\frac{L}{G}\right)^5\left(\frac{H}{G}\right)t \tag{A.7}$$

$$\Phi_D(6,1) = J_2\left(\frac{9\mu^4 {r_E}^2}{2L^8}\right)\left(\frac{L}{G}\right)^4\left(\frac{H}{G}\right)t \tag{A.8}$$

$$\Phi_D(6,5) = -J_2\left(\frac{3\mu^4 {r_E}^2}{2L^8}\right)\left(\frac{L}{G}\right)^4 t. \tag{A.9}$$

Unless otherwise stated, only non-zero elements of a matrix are listed in this section. $J_{PD}$ and $J_{DP,0}$, on the other hand, can contain "0/0" singularities

$$J_{PD}(1,1) = J_{PD}(2,2) = J_{PD}(2,4) = J_{PD}(2,6) = 1 \quad J_{DP,0}(1,1) = J_{DP,0}(2,2) = J_{DP,0}(3,1) = J_{DP,0}(5,1) = 1 \tag{A.10}$$

$$J_{PD}(4,4) = J_{PD}(4,6) = \mathfrak{G} \qquad J_{DP,0}(3,3) = J_{DP,0}(5,3) = -\mathfrak{G}^0 \tag{A.11}$$

$$J_{PD}(3,4) = -J_{PD}(3,6) = -\mathfrak{g} \qquad J_{DP,0}(3,4) = J_{DP,0}(5,4) = -\mathfrak{g}^0 \tag{A.12}$$

$$J_{PD}(6,6) = \mathfrak{H} \qquad J_{DP,0}(5,5) = -\mathfrak{H}^0 \tag{A.13}$$

$$J_{PD}(5,6) = -\mathfrak{h} \qquad J_{DP,0}(5,6) = -\mathfrak{h}^0 \tag{A.14}$$

$$J_{PD}(3,1) = -J_{PD}(3,3) = \frac{\mathfrak{G}}{\mathfrak{G}^2 + \mathfrak{g}^2} \qquad J_{DP,0}(2,4) = J_{DP,0}(4,4) = -\frac{\mathfrak{G}^0}{(\mathfrak{G}^0)^2 + (\mathfrak{g}^0)^2} \tag{A.15}$$

$$J_{PD}(4,1) = -J_{PD}(4,3) = \frac{\mathfrak{g}}{\mathfrak{G}^2 + \mathfrak{g}^2} \qquad J_{DP,0}(2,3) = -J_{DP,0}(4,3) = \frac{\mathfrak{g}^0}{(\mathfrak{G}^0)^2 + (\mathfrak{g}^0)^2} \tag{A.16}$$

$$J_{PD}(5,3) = -J_{PD}(5,5) = \frac{\mathfrak{H}}{\mathfrak{H}^2 + \mathfrak{h}^2} \qquad J_{DP,0}(4,6) = -J_{DP,0}(6,6) = -\frac{\mathfrak{H}^0}{(\mathfrak{H}^0)^2 + (\mathfrak{h}^0)^2} \tag{A.17}$$

$$J_{PD}(6,3) = -J_{PD}(6,5) = \frac{\mathfrak{h}}{\mathfrak{H}^2 + \mathfrak{h}^2} \qquad J_{DP,0}(5,4) = -J_{DP,0}(6,5) = \frac{\mathfrak{h}^0}{(\mathfrak{H}^0)^2 + (\mathfrak{h}^0)^2}. \tag{A.18}$$

But these singularities cancel out when $\Phi_P$ is computed

$$\Phi_P(1,1) = 1 \tag{A.19}$$

$$\Phi_P(2,1) = \Phi_D(2,1) + \Phi_D(2,3) + \Phi_D(2,5) + \Phi_D(4,1) + \Phi_D(4,3) + \ldots \Phi_D(4,5) + \Phi_D(6,1) + \Phi_D(6,3) + \Phi_D(6,5) \tag{A.20}$$

$$\Phi_P(2,3) = -\mathfrak{G}^0 \{\Phi_D(2,3) + \Phi_D(4,3) + \Phi_D(6,3) + \Phi_D(2,5) + \Phi_D(4,5) + \Phi_D(6,5)\} \tag{A.21}$$

$$\Phi_P(2,4) = -\mathfrak{g}^0 \{\Phi_D(2,3) + \Phi_D(4,3) + \Phi_D(6,3) + \Phi_D(2,5) + \Phi_D(4,5) + \Phi_D(6,5)\} \tag{A.22}$$

$$\Phi_P(2,5) = -\mathfrak{H}^0 \{\Phi_D(2,5) + \Phi_D(4,5) + \Phi_D(6,5)\} \tag{A.23}$$

$$\Phi_P(2,6) = -\mathfrak{h}^0 \{\Phi_D(2,5) + \Phi_D(4,5) + \Phi_D(6,5)\} \tag{A.24}$$

$$\Phi_P(3,1) = -\mathfrak{g}\{\Phi_D(4,1) + \Phi_D(4,3) + \Phi_D(4,5) + \Phi_D(6,1) + \Phi_D(6,3) + \Phi_D(6,5)\} \tag{A.25}$$

$$\Phi_P(3,3) = \frac{\mathfrak{G}\mathfrak{G}^0}{\mathfrak{G}^2+\mathfrak{g}^2} + \frac{\mathfrak{g}\mathfrak{g}^0}{(\mathfrak{G}^0)^2+(\mathfrak{g}^0)^2}\mathfrak{G}^0\mathfrak{g}\{\Phi_D(4,3) + \Phi_D(4,5) + \Phi_D(6,3) + \Phi_D(6,5)\} \tag{A.26}$$

$$= \cos\left\{(g-g^0)+(h-h^0)\right\} + \mathfrak{G}^0\mathfrak{g}\{\Phi_D(4,3) + \Phi_D(4,5) + \Phi_D(6,3) + \Phi_D(6,5)\} \tag{A.27}$$

$$\Phi_P(3,4) = \frac{\mathfrak{G}\mathfrak{g}^0}{\mathfrak{G}^2+\mathfrak{g}^2} - \frac{\mathfrak{g}\mathfrak{G}^0}{(\mathfrak{G}^0)^2+(\mathfrak{g}^0)^2} + \mathfrak{g}^0\mathfrak{g}\{\Phi_D(4,3) + \Phi_D(4,5) + \Phi_D(6,3) + \Phi_D(6,5)\} \tag{A.28}$$

$$= \sin\left\{(g-g^0)+(h-h^0)\right\} + \mathfrak{g}^0\mathfrak{g}\{\Phi_D(4,3) + \Phi_D(4,5) + \Phi_D(6,3) + \Phi_D(6,5)\} \tag{A.29}$$

$$\Phi_P(3,5) = \mathfrak{g}\mathfrak{H}^0\{\Phi_D(4,5) + \Phi_D(6,5)\} \tag{A.30}$$

$$\Phi_P(3,6) = \mathfrak{g}\mathfrak{h}^0\{\Phi_D(4,5) + \Phi_D(6,5)\} \tag{A.31}$$

$$\Phi_P(4,1) = \mathfrak{G}\{\Phi_D(4,1) + \Phi_D(4,3) + \Phi_D(4,5) + \Phi_D(6,1) + \Phi_D(6,3) + \Phi_D(6,5)\} \tag{A.32}$$

$$\Phi_P(4,3) = \frac{\mathfrak{g}\mathfrak{G}^0}{\mathfrak{g}^2+\mathfrak{G}^2} - \frac{\mathfrak{G}\mathfrak{g}^0}{(\mathfrak{G}^0)^2+(\mathfrak{g}^0)^2} - \mathfrak{G}^0\mathfrak{G}\{\Phi_D(4,3) + \Phi_D(4,5) + \Phi_D(6,3) + \Phi_D(6,5)\} \tag{A.33}$$

$$= \sin\left\{(g-g^0)+(h-h^0)\right\} - \mathfrak{G}^0\mathfrak{G}\{\Phi_D(4,3) + \Phi_D(4,5) + \Phi_D(6,3) + \Phi_D(6,5)\} \tag{A.34}$$

$$\Phi_P(4,4) = \frac{\mathfrak{g}\mathfrak{g}^0}{\mathfrak{G}^2+\mathfrak{g}^2} + \frac{\mathfrak{G}\mathfrak{G}^0}{(\mathfrak{G}^0)^2+(\mathfrak{g}^0)^2} - \mathfrak{g}^0\mathfrak{G}\{\Phi_D(4,3) + \Phi_D(4,5) + \Phi_D(6,3) + \Phi_D(6,5)\} \tag{A.35}$$

$$= \cos\left\{(g-g^0)+(h-h^0)\right\} - \mathfrak{g}^0\mathfrak{G}\{\Phi_D(4,3) + \Phi_D(4,5) + \Phi_D(6,3) + \Phi_D(6,5)\} \tag{A.36}$$

$$\Phi_P(4,5) = -\mathfrak{G}\mathfrak{H}^0\{\Phi_D(4,5) + \Phi_D(6,5)\} \tag{A.37}$$

$$\Phi_P(4,6) = -\mathfrak{G}\mathfrak{h}^0\{\Phi_D(4,5) + \Phi_D(6,5)\} \tag{A.38}$$

$$\Phi_P(5,1) = -\mathfrak{h}\{\Phi_D(6,1) + \Phi_D(6,3) + \Phi_D(6,5)\} \tag{A.39}$$

$$\Phi_P(5,3) = \mathfrak{h}\mathfrak{G}^0\{\Phi_D(6,3) + \Phi_D(6,5)\} \tag{A.40}$$

$$\Phi_P(5,4) = \mathfrak{h}\mathfrak{g}^0\{\Phi_D(6,3) + \Phi_D(6,5)\} \tag{A.41}$$

$$\Phi_P(5,5) = \frac{\mathfrak{H}\mathfrak{H}^0}{\mathfrak{H}^2+\mathfrak{h}^2} + \frac{\mathfrak{h}\mathfrak{h}^0}{(\mathfrak{H}^0)^2+(\mathfrak{h}^0)^2} + \mathfrak{h}\mathfrak{H}^0\Phi_D(6,5) \tag{A.42}$$

$$= \cos\left(h-h^0\right) + \mathfrak{h}\mathfrak{H}^0\Phi_D(6,5) \tag{A.43}$$

$$\Phi_P(5,6) = \frac{\mathfrak{H}\mathfrak{h}^0}{\mathfrak{H}^2+\mathfrak{h}^2} - \frac{\mathfrak{h}\mathfrak{H}^0}{(\mathfrak{H}^0)^2+(\mathfrak{h}^0)^2} + \mathfrak{h}\mathfrak{h}^0\Phi_D(6,5) \tag{A.44}$$

$$= -\sin\left(h-h^0\right) + \mathfrak{h}\mathfrak{h}^0\Phi_D(6,5) \tag{A.45}$$

$$\Phi_P(6,1) = \mathfrak{H}\{\Phi_D(6,1) + \Phi_D(6,3) + \Phi_D(6,5)\} \tag{A.46}$$

$$\Phi_P(6,3) = -\mathfrak{H}\mathfrak{G}^0\{\Phi_D(6,3) + \Phi_D(6,5)\} \tag{A.47}$$

$$\Phi_P(6,4) = -\mathfrak{H}\mathfrak{g}^0\{\Phi_D(6,3) + \Phi_D(6,5)\} \tag{A.48}$$

$$\Phi_P(6,5) = \frac{\mathfrak{h}\mathfrak{H}^0}{\mathfrak{H}^2+\mathfrak{h}^2} - \frac{\mathfrak{H}\mathfrak{h}^0}{(\mathfrak{H}^0)^2+(\mathfrak{h}^0)^2} - \mathfrak{H}\mathfrak{H}^0\Phi_D(6,5) \tag{A.49}$$

$$= \sin\left(h-h^0\right) - \mathfrak{H}\mathfrak{H}^0\Phi_D(6,5) \tag{A.50}$$

$$\Phi_P(6,6) = \frac{\mathfrak{h}\mathfrak{h}^0}{\mathfrak{H}^2+\mathfrak{h}^2} + \frac{\mathfrak{H}\mathfrak{H}^0}{(\mathfrak{H}^0)^2+(\mathfrak{h}^0)^2} - \mathfrak{H}\mathfrak{h}^0\Phi_D(5,6) \tag{A.51}$$

$$= \cos\left(h-h^0\right) - \mathfrak{H}\mathfrak{h}^0\Phi_D(5,6). \tag{A.52}$$

Note that the Delaunay angles only appear as a difference between the initial and current values, meaning that, since the rate of change of the angles are well-defined and constant for any orbit, the differences are also well-defined.

## Appendix B

## Initial Orbital Elements For Observed and Observing Objects in The Direct Bayesian Examples

Table B.1: The classical orbital elements at the epoch time for all 8 observed objects and 2 observer satellites in the Examples section where $r_E$ is Earth radius.

| **Name** | $a$ [$r_E$] | $e$ | $i$ [rad] | $\Omega$ [rad] | $\omega$ [rad] | $M$ [rad] |
|---|---|---|---|---|---|---|
| GEO1 | 6.6102 | 0.0003 | 0.0002 | 3.1274 | 2.3294 | 5.7226 |
| GEO2 | 6.6109 | 0.0003 | 0.0009 | 5.9501 | 2.9681 | 5.8729 |
| GEO3 | 6.6109 | 0.0001 | 0.0001 | 3.0902 | 4.2464 | 6.1176 |
| MOL1 | 4.1971 | 0.7154 | 1.1204 | 0.8126 | 5.1137 | 0.1671 |
| EM1 | 3.6573 | 0.7123 | 0.3106 | 1.0976 | 1.6080 | 5.9942 |
| EM2 | 4.1472 | 0.5529 | 1.2347 | 5.5811 | 2.4137 | 4.8996 |
| CM1 | 3.9994 | 0.0006 | 1.1284 | 4.9148 | 4.2128 | 2.9461 |
| GPS1 | 4.1645 | 0.0048 | 0.9599 | 2.7242 | 3.6934 | 2.5851 |
| LEO1 | 1.1219 | 0.0002 | 1.5080 | 2.2899 | 1.3765 | 4.9092 |
| LEO2 | 1.1211 | 0.0147 | 1.3223 | 0.2616 | 5.3095 | 0.9519 |
| LEO3 | 1.1512 | 0.0266 | 1.7134 | 2.0417 | 5.7676 | 0.4918 |
| LEO-O | 1.0988 | 0.0001 | 1.7088 | 1.0000 | 0.1000 | 0.1000 |
| GEO-O | 6.6109 | 0.0001 | 0.0001 | 1.0000 | 0.1000 | 0.1000 |
| GEO-O' | 6.6109 | 0.0010 | 0.0044 | 1.0000 | 0.1000 | 0.1000 |

Table B.2: The Poincaré orbital elements at the epoch time for all 8 observed objects and 2 observer satellites in the Examples section listed as ($a$ [$r_E$], $e$, $i$ [rad], $\Omega$ [rad], $\omega$ [rad], $M$ [rad]), ($\mathfrak{L}$ [$r_E^2$/hour], $\mathfrak{l}$ [rad], $\mathfrak{G}$ [$r_E$/hour$^{1/2}$], $\mathfrak{g}$ [$r_E$/hour$^{1/2}$], $\mathfrak{H}$ [$r_E$/hour$^{1/2}$], $\mathfrak{h}$ [$r_E$/hour$^{1/2}$]), where $r_E$ is Earth radius.

| **Name** | $\mathfrak{L}$ | $\mathfrak{l}$ | $\mathfrak{G}$ | $\mathfrak{g}$ | $\mathfrak{H}$ | $\mathfrak{h}$ |
|---|---|---|---|---|---|---|
| GEO1 | 11.4721 | 4.8962 | 0.0006 | 0.0006 | 0.0000 | -0.0006 |
| GEO2 | 11.4727 | 2.2247 | -0.0005 | -0.0009 | 0.0010 | 0.0029 |
| GEO3 | 11.4727 | 0.8879 | -0.0003 | 0.0001 | 0.0000 | -0.0002 |
| MOL1 | 9.1414 | 6.0934 | 0.8200 | 2.1991 | -1.9501 | 1.8469 |
| EM1 | 8.5333 | 2.4166 | -0.9526 | -2.0447 | -0.6739 | 0.3451 |
| EM2 | 9.0868 | 0.3281 | -1.7237 | -0.2444 | 2.0573 | 2.4323 |
| CM1 | 8.9234 | 5.7905 | -0.0005 | -0.0017 | 3.1297 | 0.6421 |
| GPS1 | 9.1057 | 2.7195 | -0.0019 | 0.0143 | -1.1296 | -2.5474 |
| LEO1 | 4.7263 | 2.2925 | 0.0003 | -0.0005 | -2.2395 | -1.9606 |
| LEO2 | 4.7245 | 0.2398 | 0.0209 | 0.0242 | -0.6902 | 2.5783 |
| LEO3 | 4.7876 | 2.0179 | -0.0582 | 0.0026 | -2.9466 | -1.5001 |
| LEO-O | 4.6772 | 1.2000 | -0.0002 | 0.0001 | -2.7450 | 1.7625 |
| GEO-O | 11.4727 | 1.2000 | -0.0003 | 0.0002 | -0.0003 | 0.0002 |
| GEO-O' | 11.4727 | 1.2000 | -0.0030 | 0.0015 | -0.0124 | 0.0080 |

## Appendix C

## Pseudo-Code For The Direct Bayesian Admissible Region Method

Load first observation (i.e. its attributable vector)

Remove the first observation from the observation list

Correlate first observation with second observation

$i = 3$

WHILE observations are not correlated

    Load $i$-th observation
    Correlate first observation with $i$-th observation
    $i = i + 1$

END

IF none of the observation correlate with the first observation

    Initialization failed, end routine

ELSE

    Store the overlap between the first and $i - 1$ th observation as Object 1
    Remove $i - 1$ th observation from the observation list
    $j = 2$
    WHILE observations exist in list

        Load $j$-th observation
        Remove $j$-th observation from the observation list
        Load Object 1
        Correlate $j$-th observation with Object 1
        $l = 2$
        WHILE object and observations are not correlated AND $l <$ (number of objects accounted for)

```
            Load l-th object
            Correlate j-th observation with Object l
            l = l + 1
        END
        IF j-th observation and Object l − 1 correlate
            Store the overlap between the j-th observation and Object l − 1 as
            the new Object l − 1
        ELSE
            Load j + 1 th observation
            Correlate j-th observation with j + 1 th observation
            k = 2
            WHILE observations are not correlated
                Load j + k th observation
                Correlate j-th observation with j + k th observation
                k = k + 1
            END
            IF none of the observation correlate with the j-th observation
                Store j-th observation as an observation that failed to
                correlate
            ELSE
                Store the overlap between the j-th observation and the
                j + k − 1 th observation as Object N, where
                N = (number of objects accounted for) + 1
                Remove j + k − 1 th observation from the observation list
            END
        END
        j = j + 1
    END

END
```

## Appendix D

## Keplerian Orbital Elements of All Objects Detected in The ZimSMART Observations With The Hybrid Method

Table D.1: Keplerian orbital elements of all objects detected with the hybrid approach: semi-major axis ($a$), eccentricity ($e$), inclination ($i$), right ascension of the ascending node ($\Omega$), argument of periapsis ($\omega$), and mean anomaly ($M$). Solutions sorted by the epoch of the first tracklet. "Tr 1" and "Tr 2" indicate the objects that the associated tracklets were correlated to by the AIUB code. Objects in the NORAD TLE catalog are denoted by their 6 letter international designator, those in AIUB's internal catalog by a 7 letter designator starting with "Z," and uncorrelated tracks by a bracketed number assigned by tracklet epoch. "Type" is the solution type: I, II, or III.

| Obj # | $a$ [km] | $e$ | $i$ [deg] | $\Omega$ [deg] | $\omega$ [deg] | $M$ [deg] | Tr 1 | Tr 2 | Type |
|---|---|---|---|---|---|---|---|---|---|
| 1 | 42167.9389 | 0.00504009 | 0.15268036 | 0.67247208 | 0.67106167 | 4.62098602 | [ 3] | Z12230C | III |
| 2 | 42553.9802 | 0.00220195 | 0.14845483 | 1.02426359 | -2.9210019 | 1.58577527 | 94022A | 94022A | I |
| 3 | 42474.7078 | 0.00104508 | 0.05504329 | 1.20373515 | 0.46646274 | 4.33420972 | 93078B | 93078B | I |
| 4 | 20370.2703 | 0.57401358 | 0.04134642 | -1.4298436 | -2.0797513 | 3.30584577 | 10032B | 98050A | II |
| 5 | 42167.8135 | 0.00485164 | 0.00833985 | 1.41736384 | -0.1245722 | 4.65738998 | 00081A | 00081A | I |
| 6 | 44103.7561 | 0.03316462 | 0.00274204 | 1.53057116 | -1.8511525 | 6.26491311 | 98050A | 09008B | I |
| 7 | 20367.0045 | 0.60109671 | 0.07350824 | -2.8500348 | -0.3679198 | 2.27664978 | 00054A | 10025A | II |
| 8 | 42166.739 | 0.00031368 | 0.00169132 | 0.99188551 | 2.49933109 | 2.45658423 | [ 13] | [ 120] | III |
| 9 | 20489.5672 | 0.56649625 | 0.04421714 | -2.3842792 | -0.9701911 | 2.77169499 | 08065B | 10021A | II |
| 10 | 26695.5358 | 0.38589704 | 0.02869554 | -1.0047144 | -2.714267 | 3.61614499 | 11041A | 98057A | II |
| 11 | 42358.4502 | 0.00639731 | 0.12502374 | 1.02260295 | -2.8554889 | 1.46486536 | 91075A | 91075A | I |
| 12 | 42166.1451 | 0.00504257 | 0.00645396 | 1.49216639 | 2.92711687 | 1.43573959 | 02015B | 02015B | I |
| 13 | 42165.7048 | 0.00465978 | 0.00503632 | -0.1067257 | -1.8389239 | 1.53631869 | 98006B | 98006B | I |
| 14 | 42166.3074 | 0.00442969 | 0.00214473 | 2.01311262 | 2.3699257 | 1.51251347 | 10025A | 10025A | I |
| 15 | 42165.9793 | 0.00151075 | 0.00235757 | 1.3716077 | 3.06449675 | 1.4651209 | 08034B | 08034B | I |
| 16 | 42166.089 | 0.00093822 | 0.00177328 | 1.16793164 | 0.5203132 | 4.20931434 | 98057A | 98057A | I |
| 17 | 42369.2386 | 0.00313633 | 0.23807355 | 0.57337329 | 0.69360244 | 4.30588617 | 85015B | 85015B | I |
| 18 | 27240.5471 | 0.34495023 | 0.01671134 | -1.7512588 | -1.6627614 | 2.29904061 | 04008A | 98024A | II |
| 19 | 42359.0222 | 0.01589573 | 0.18605515 | 0.58086998 | -2.3777622 | 0.8033633 | Z11003C | Z11003C | I |
| 20 | 26755.2517 | 0.38458146 | 0.03241271 | -0.879943 | -2.7948581 | 2.30041338 | 01042A | Z12230G | II |